Nyilatkozom, hogy az értekezés önálló munkám és más művekből szó szerint idézett vagy tartalmilag átvett részeket megfelelő módon idézem.

Budapest, 2024. 06. 13.

……

Nyilatkozom, hogy az értékezés és a tézisfüzetek leadott nyomtatott és elektronikus példányai mindenben azonosak.

Budapest, 2024. 06. 13.

……

Nyilatkozom, hogy hozzájárulok az értekezés és a tézisfüzet nyilvánosságra hozatalához.

Budapest, 2024. 06. 13.

……

Hozzájárulok, hogy fokozatszerzési eljárásom anyagát – beleértve az abban foglalt személyes adataimat – a vonatkozó jogszabályok és a Budapesti Műszaki és Gazdaságtudományi Egyetem belső szabályzatai szerint arra jogosult személyek és testületek megismerhessék, illetve az adataimat kezeljék.

Budapest, 2024. 06. 13.

……

Graduate School of Physics
Budapest University of Technology and Economics

Phase-Field Crystal Modeling of Nucleation and Growth Processes

Ph.D. dissertation

Frigyes Podmaniczky

Wigner Research Centre for Physics

Budapest, Hungary
2024

Contents

Symbols and Abbreviations

a	lattice constant
A_{noise}	noise amplitude
ATG	Asaro-Tiller-Grinfeld
b	length of Burger's vector
BCC	body centered cubic
BD	Brownian dynamics
β	$(k_{\text{B}}T)^{-1}$
c_0	$c(k=0)$, related to compressibility $\kappa^{-1} = (1-c_0)\,\rho_l k_{\text{B}}T$
$c^{(1)}(\boldsymbol{r})$	one-particle direct correlation function
$c^{(2)}(\boldsymbol{r}_1, \boldsymbol{r}_2)$	two-particle direct correlation function
$c\,(k)$	Fourier transform of the direct pair correlation function
CNT	classical nucleation theory
DDFT	dynamical DFT
$\delta(\boldsymbol{r})$	Dirac-delta
$\Delta\omega$	thermodynamic driving force, grand potential density difference
$\delta F[y(x)]/\delta y$	variational/functional derivative
DFT	density functional theory
D	diffusion constant
DPFC	diffusive PFC
E	Young's modulus
EL	Euler-Lagrange
ELE	Euler-Lagrange equation
EOM	equation of motion
ϵ	PFC model parameter
η	fractional density change
F	Helmholtz free energy
FCC	face centered cubic
F_{ex}	excess free energy
f	lattice misfit, $f = (\sigma_s - \sigma_f)\,/\sigma_f$
F_{id}	free energy of ideal gas

FNH	fluctuating nonlinear hydrodynamics
γ	interface free energy
GFN	growth front nucleation
G	shear modulus
h	epitaxial layer thickness
h_c	critical layer thickness
HPFC	hydrodynamic PFC
HS	hard sphere
INCA-HPFC	incompressibly advected HPFC model
JMAK	Johnson-Mehl-Avrami-Kolmogorov
κ	compressibility, $\kappa^{-1} = (1 - c_0)\,\rho_l k_\mathrm{B} T$
$k_\mathrm{B}T$	average thermal energy
k, q	wavenumber
KTHNY	Kosterlitz-Thouless-Halperin-Nelson-Young
Λ	thermal de Broglie wavelength
λ	modulation wavelength
LJ	Lennard-Jones
log	natural logarithm
$\log 10$	base-10 logarithm
MB	Matthews-Blakeslee
MC	Monte Carlo
MD	molecular dynamics
MRCO	medium range crystalline order
μ	chemical potential
μ_B	bulk viscosity
μ_S	shear viscosity
ν	Poisson's ratio
Ω	grand potential
ω	ATG growth factor
OP	order parameter
$\boldsymbol{p}$	momentum density
PBC	periodic boundary condition
PB	People-Bean
PDE	partial differential equation
PFC	phase-field crystal
PF	phase-field
PFT	phase-field theory
P	pressure
ψ	order parameter

PY	Percus-Yevick
q_0	selected wavenumber
q_l	bond orientational order parameter
$\overline{q}_l$	first neigbor averaged q_l
Ra	Rayleigh number
RDF	radial distribution function
$\rho^*(\boldsymbol{r})$	density distribution at an extremum of a functional
$\rho(\boldsymbol{r})$	number density
ρ_0	reference liquid density
ρ_l	average liquid density
RLV	reciprocal lattice vector
RY	Ramakrishnan-Yussouff
SG	square gradient
SH	Swift-Hohenberg
σ	stress
σ_f	lattice constant of unstrained layer
σ_s	lattice constant of substrate
$S(q)$	structure factor
Θ	crystalline orientation in 2D
T_m	melting temperature
$\boldsymbol{v}$	velocity field
VDM	van der Merwe
V	volume
$V(\boldsymbol{x})$	external potential
W_{het}	work of formation, heterogeneous nucleus
W_{hom}	work of formation, homogeneous nucleus
ξ	number of solid bonds
$X_{\max}$	final solid fraction
$X(t)$	solid fraction in time
ζ	noise term accounting for fluctuations

Acknowledgements

I would like to express my sincere gratitude to my thesis advisor, the late Dr. László Gránásy, for his invaluable guidance, encouragement and support throughout the completion of this work.

I am also grateful to my colleagues, for their constructive feedback, helpful suggestions and fruitful collaboration. They have made this journey more enjoyable and rewarding.

A huge appreciation goes to my loving mother, who has always encouraged me to pursue my interests.

Last but not least, I am blessed with the company of my wife who has put up with my many flaws over the years and tried to understand me the best as she could and who has also been my best friend.

The following quote faithfully pictures the spirit of this dissertation:

"A model is a lie that helps you see the truth"

Chapter 1

Introduction

1.1 Motivation

Behind the rising standards of living in modern societies, there lies a corresponding increase in our understanding of the science of materials processing and also an increase in diversity of engineered materials, which have little to no counterparts occurring naturally. The properties of such materials, ranging from their mechanical strength to their electrical properties are intimately connected to their underlying microstructure.

For example, the crystal structure and impurity content of a semiconductor material determine its band structure and its electrical performance. Similarly, in construction applications, weight-to-strength ratios are critical and high-strength steels are required to withstand the enormous loads and stresses placed upon them. In these situations, engineers turn to lighter alloys that are strengthened by precipitating second-phase particles within their original grain structure. These steels typically contain a favorable combination of grain boundaries and a mix of refined crystal grains, allowing them to maintain their strength, while also remaining ductile. The development of perlitic steels (alternating layers of ferrite and cementite) played a crucial role, for example, in the lengthening of bridge spans, allowing for the construction of longer and more complex structures.

From a technological point of view, solidification is a key link in the materials processing chain. This first order phase transformation starts with homogeneous or heterogeneous nucleation. Although, this happens on the nanoscale, it usually influences the grain-size distribution and the related physical properties on larger scales. Accordingly, crystallization of molten materials is truly a multiscale process both in time and space.

The microstructure of materials develop through a variety of processes, including solidification, solid-state precipitation and thermo-mechanical processing. These processes are governed by the fundamental physics of free boundary dynamics and non-equilibrium phase transformation kinetics. For example, in solidification and re-crystallization, nucleation of crystal grains is followed by a competitive growth of these grains under the drive to reduce the overall free energy of the system. This process is limited by the diffusion of heat and mass, which itself depends on thermodynamic parameters.

The driving forces can be identified in a range of phenomena, for example they can result from the minimization of bulk free energy, anisotropic surface energy or elastic energy. Elastic effects in strain-induced transformations during heat treatment have profound consequences on the morphology and distribution of second-phase precipitates and grain boundaries.

The modeling of the microstructure and the prediction of material properties, has greatly benefited from recent advances in theoretical and numerical tools. A variety of theoretical models have been developed to capture different aspects of solidification. Particle based methods include ab initio computations, Monte Carlo (MC) simulations and Molecular Dynamics (MD). Continuum based methods include the density functional theory of classical particles, coarse-grained phase-field models and large scale sharp interface models.

Modern parallel computing now allows billions of atoms to be simulated for nanoseconds, while various continuum and sharp interface methods have made it possible to quantitatively model free surface kinetics responsible for microstructure formation up to 100's of micrometers.

Despite these advances, each methodology comes with its own advantages and limitations. Accordingly, often a combination of models is required to address specific problems. As a result, there is a constant need for new and innovative techniques, to better understand the relationships between microstructure and material properties.

It is clear, that the technological advancements of societies have often been linked to their ability to engineer new materials and exploit their properties. From the earliest days of human history to the present days, our understanding of materials science has allowed us to create new and exciting technologies that have changed the world.

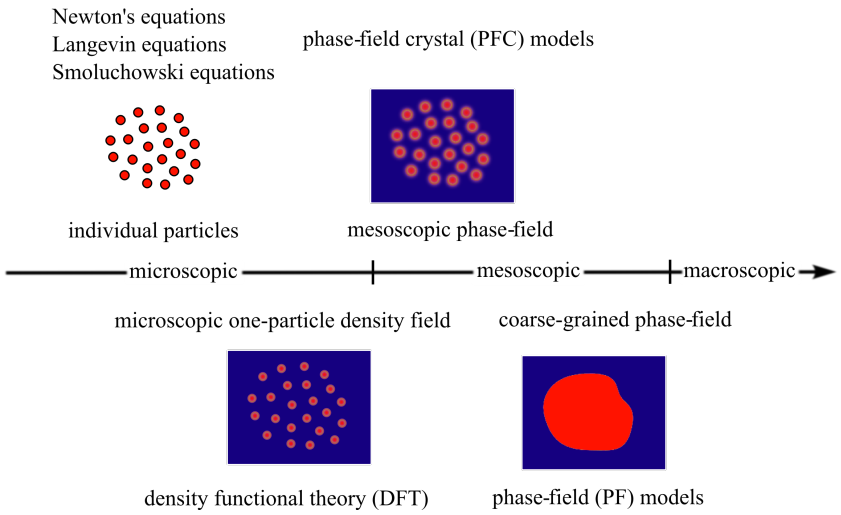

Figure 1.1: Location of the PFC model according to the level of description in the materials science modeling hierarchy.

1.2 Goals

In this dissertation, I am going to address crystal nucleation and growth phenomena on the molecular scale. To accomplish this, I rely on the phase-field crystal (PFC) [1] model (see Fig. 1.1, which can be viewed as a simple dynamical density functional theory (DDFT), which has been proposed in its simplest form by K. R. Elder et al. in 2002. Its form is motivated on the basis of an approximation procedure to classical density functional theory (DFT). Owing to its relative simplicity, especially, when numerical simulations are considered, it rapidly became fairly popular and has been employed to model a broad range of physical phenomena, as it can address the simulation of fairly sizeable crystals (containing up to several millions of atoms) on a diffusive time scale.

Although, in most cases, the PFC model can only be viewed as a qualitative description of these phenomena, it contains naturally such features as crystalline and amorphous structures, elasticity and crystalline anisotropies, among others. In a few cases, attempts have been made (see Ref. [2]) to make advanced PFC models even quantitative.

Herein, I am going to use the single-mode PFC model from Elder et al. to address early stages of crystallization, including homogeneous and heterogeneous crystal nucleation and strained heteroepitaxial growth. In its original form, it relies on overdamped particle dynamics, a combination, which is expected to be reasonable for colloidal suspensions. The simplicity of the PFC model makes it suitable for investigating the effect of different relaxation dynamics (hydrodynamic

vs. diffusive) on crystallization. Along this line, I am going to present dynamic extensions, that rely on hydrodynamic density transport, which is expected to approximate the behaviour of simple liquids, such as liquid metals. Relying on these techniques, I investigate structural aspects of two-/multi-step nucleation and the effect of the mode of density relaxation on such structures. I also attempt to answer the question, whether the amorphous precursor based two-step nucleation reported for diffusive dynamics (colloidal suspensions) can occur in the case of simple liquids or metals, which may have practical significance. The present work opens the way for developing improved models of nucleation. This work forms part of the "Élvonal" Excellence Program of the National Agency for Research, Development and Innovation, Hungary (NKFIH) under Contract No. KKP-126749.

1.3 Phase transformations

This thesis revolves around the topic of solidification. It is a subject of materials science, which itself is the predictive study of the properties and behaviour of homogeneous and heterogeneous phases of matter and the interplay between the different phases of materials, in and out of equilibrium. The kinetics of phase transformations form a significant part of this field, since in practice, materials even in the long-time limit, rarely reach their theoretically possible, most stable state. Rather, they tend to remain *stuck* in locally stable states, which include defects and other inhomogeneities, that will determine their physical properties and so their technological applicability.

The initial state of matter during solidification is usually structureless, e.g. a molten liquid state. This initial thermodynamic state can be represented on the phase diagram as a point, which can be made metastable, by changing certain external thermodynamic variables, such as the temperature or pressure. Under the relaxation time, the system reaches the values of the changed external parameters. Metastability of a system means, that besides the current one, there exists another state compatible with external conditions with a lower free energy. Metastable phases act as equilibrium phases, they are stable against small perturbations, but there exist certain large perturbations, which provide an *irreversible* path to the preferred, more stable phase with lower free energy.

First order phase transformations start with nucleation, which is the formation of a cluster of the more stable phase inside the metastable phase. These heterophase clusters represent non-equilibrium states, which connect the metastable phase with the stable one. Their work of formation exhibits an energetic barrier as the size

of the cluster is increased. The nucleus is the state, located at the top of the barrier. While the nucleus is associated with the maximum of the work of formation wrt. cluster size, it still represents the lowest energy barrier in the space of all possible fluctuations. In the free energy landscape, the nucleus is associated with a mathematical saddle point. The process of nucleation is a thermally activated process, because thermal fluctuations lead to the passing of this minimum energy barrier.

Single phase systems can also be prepared in a thermodynamically unstable state, which separates into more stable phases. In such unstable systems, any perturbation can initiate the transformation process unconditionally, this process is called a spinodal decomposition. A closer analysis reveals, that in models, which account for thermal fluctuations, metastable systems close to the spinodal transform via a so-called kinetic spinodal. It manifests, when the barrier of transformation becomes comparable to $k_{\mathrm{B}}T$, the average thermal activation energy. In the phase diagram, the spinodal lines meet the binodal lines (marking phase coexistence of the stable phases) in a critical point.

In the case, when two coexisting phases are present and separated by a planar interface, an infinitesimal decrease in the internal energy of the system will drive a proportional increase in the solid fraction. This change in internal energy is the latent heat, that is released during the transformation and which is a hallmark of first order phase transformations. If the same amount of energy is absorbed by the system, the solid fraction will return to its previous value.

This is an example of a reversible phase transformation, which is a quasi-static process at a well defined temperature, pressure and chemical potential. However, in practice, due to large driving forces, the phase transformation is often an irreversible, non-equilibrium growth process, which takes the system closer to a globally stable state. The resulting microstructure and the accumulation of defects are determined by the path and velocity of transformation, that is realized during non-equilibrium processing.

1.4 Levels of description

The empirical study of internal energy, work and heat transfer in real systems paved the way to the foundation of thermodynamics. This was completed with the discovery of entropy, an important, but concealed quantity, elaborated on in App. A.1. The introduction of this additional state variable generalized the mechanical definition of internal energy to thermal phenomena. The mathematical

framework of equilibrium thermodynamics serves as the basis for order parameter theories of aggregate matter. The concept of irreversibility is closely linked to the modeling of out of equilibrium systems. Time-dependent continuum theories must provide a mechanism for dissipation or entropy production, which takes the system closer to equilibrium. This mechanism is phenomenological in nature, it has not been rigorously derived from microscopic theories with time reversal symmetry.

In materials science and especially in the study of the condensed phases of matter, the basic interaction between atoms or molecules is of quantum mechanical origin. Many contemporary phenomena cannot be understood on the sole basis of classical mechanics. In most liquids, the thermal de Broglie wavelength $\Lambda = (2\pi\beta\hbar^2/m)^{1/2}$ is much smaller than the nearest-neighbor separation $a \approx \rho^{-1/3}$ so a classical approximation can be adequate for the calculation of static properties at not too low temperatures and not too high pressures. Much progress is possible, relying on classical mechanics alone. The traces of quantum mechanics is found in the exact form of the effective interaction potential between the constituent particles. We are concerned with the description of matter composed of classical particles, with a prescribed interaction between them. The temporal evolution of such systems is determined by Hamiltonian dynamics, the direct numerical solution of which is referred to as molecular dynamics (MD), this model serves as a means for the validation of more coarse-grained, effective theories.

The classical approximation leads to the significant simplification, that the thermodynamic effects that come from thermal motion can be separated from the effects of interaction between the particles. This separation of the potential (V) and kinetic (K) energy contributions also leads to a means of characterizing the liquid state. In the gaseous phase the ratio $K/V \gg 1$ and in the low-temperature solid $K/V \ll 1$, while in the dense liquid phase $K/V \approx 1$. If the system is characterized by a length scale σ which corresponds to the range and energy scale ϵ to the strength of the intermolecular forces, then the reduced density $\rho^* = N\sigma^3/V$ and the reduced temperature $T^* = \mathrm{k_B}T/\epsilon$ are also of the order of unity. Thus in liquids, collisions have a greater importance, than in dilute gases but they lack the long-range positional order present in crystalline solids. The structure of liquids is dominated by short-range positional order and by the so-called *excluded volume* effect which is the result of close packing hard particles, that represents well all elements beyond a certain density.

The study of phase transformations can happen on different levels of description, putting emphasis on different aspects of the processes involved. While in this regard, MD forms the most fundamental, particle-based description, it is also the

computationally most expensive one. In reality and in MD simulations not too far from equilibrium, a separation of timescales is observed. On the shortest timescale, thermal motion of the particles can be discerned. This amounts to vibrations of particle positions, around the average positions, determined by a slowly decaying neighborhood of particles. On longer timescales, particles are able to exchange positions with one another, neighborhoods dissolve and new ones form. A change in the nature of aggregation can also be observed. On a still longer timescale, not only mechanical, but statistical processes rooted purely in entropy are able to equilibrate, e.g. compositional changes become salient. Finally, on the longest timescale, parcels of liquid matter flow, obeying forces due to pressure gradients and plastic deformations change the solid structure.

It is desirable, to carefully choose models, that operate on the relevant length and timescales determined by the phenomenon under study. Comparing the two extreme cases, one would rarely set out to study the velocity field and drag coefficient of an airfoil with the use of an MD simulation, since it operates on orders of magnitude smaller length and timescales, compared to the effective theory of hydrodynamics. Much of the computational resources would be wasted on resolving atomic vibrations, that do not bear significance to the fluid dynamics problem.

However, if the aim is to study the nature of the boundary condition, that the airfoil's surface imposes on the fluid, which is necessary to describe the flow problem accurately or to calculate the transport coefficient, namely viscosity, that enters the fluid dynamics problem, or to derive an equation of state between the fluid pressure and density, the use of MD can be suitable or even invaluable. It is up to the theoretician or computational experimentalist, to judge the appropriateness of the level of description for the given problem.

In the end, though, some kind of averaging has to be applied in MD simulations to provide a connection with experiments, which usually measure average properties of systems. These average properties can sometimes be obtained in a simpler way, than using MD for the solution of the trajectories of all the particles, by using for example, Monte Carlo (MC) simulations. These are probabilistic methods, that set out to calculate equilibrium statistical averages of operators, by sampling the configuration space of the system, according to a temperature dependent Boltzmann weight.

A higher level of description is achieved, when the particle based picture is dropped, in favor of a continuum based approach, the procedure of statistical averaging is partially or completely replaced by the use of a free energy functional, founded in thermodynamics.

Most effective models are based around the notion of conservation laws, the idea that certain quantities in the system can change only by related currents, that transport said quantities. The trivial examples for this can be the conservation of particle number and the conservation of momentum, the prime example of which is the Navier-Stokes equation of hydrodynamics. On the largest of length and timescales, the conservation laws are adequate for the description of the dynamics, which basically form continuity equations for the densitites of these conserved quantities. The propagation of change in these quantities are called the slow or generalized hydrodynamic modes of the system, in contrast to those changes, which are not associated with conserved quantities and thus do not obey a transport equation.

The thermodynamic basis of the order parameter theories - like the Landau theory of phase transitions - is the principle of free energy minimization. Given a system at an equilibrium state, it can be taken out of equilibrium by changing the external conditions, such as temperature. It takes the system a finite amount of time, the relaxation time to reach the new equilibrium state, set by the changed external conditions. During this time, the system cannot be described anymore solely by the thermodynamic variables, that define equilibrium. A set of physically motivated coarse-grained variables are introduced, called the order parameters, so that the state of the system can be specified as precisely as desired during this relaxation period. Expressions for the free energy in terms of these order parameters are suggested by various arguments. Dissipative processes take the system along its non-equilibrium evolution to an equilibrium distribution of the order parameter. This generalized free energy shows a minimum at the new equilibrium state, where it becomes equal to its corresponding thermodynamic potential.

Chapter 2

The freezing transition

It is an experimental fact, that most simple substances at high enough densities or low enough temperatures freeze into crystalline solids. Special precautions have to be made to avoid this transition, either molecular rearrangements need to be arrested (see glass transition [3]) or slowed down by polydispersity. Computer simulations - since they provide a well controlled playground for freezing experiments - continue to greatly contribute to our understanding of the physics of the freezing transition.

Probably the most noteworthy example of a simulated system is the hard sphere (HS) system, in which particles interacting via a hard repulsive core, surpsrisingly, crystallize into an FCC structure. Signs of this solid to liquid transition was demonstrated in an early MD simulation by Alder and Wainwright in 1957 [4]. In time, the HS system became an important reference system and the basis of perturbation theories. It was confirmed also, that freezing takes place in classical monatomic systems with repulsive two-body potentials of the form $V(r) \propto (r/a)^{-n}$ with n ranging from $n = \infty$ in the case of the HS system to $n = 1$ in the case of the one-component plasma [5].

The common feature of classical liquids near freezing is the observed structural similarity, manifested in the structure factor $S(q)$ pictured in Fig. 2.1, which measures the strength of two-point correlations wrt. particle separation. These curves near their first maxima, located at $q = q_m$ the most likely inverse separation, display high similarity and according to Verlet [6] take on a nearly universal value of $S(q_m) \approx 2.85$ at freezing. The complementary melting criterion in the solid state is the Lindemann rule [7], which states, that melting takes place, when the mean square displacement scaled by the square of the lattice constant reaches a universal value of $\langle u^2 \rangle / a^2 \approx 0.01$. Freezing parameters, like the freezing temperature or the

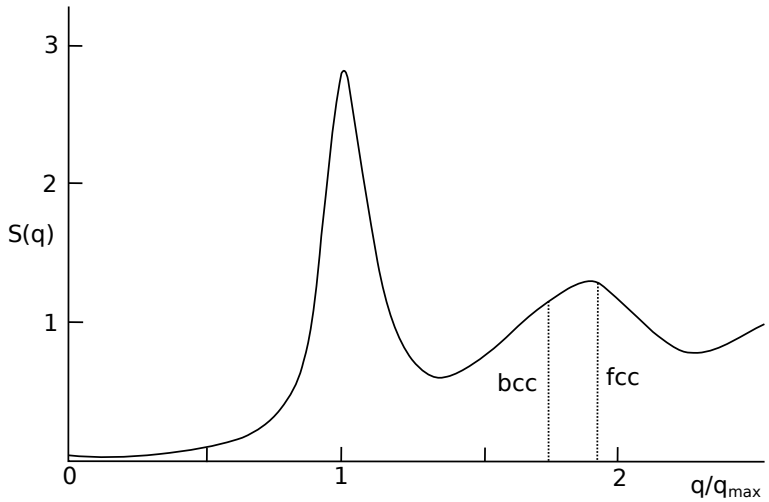

Figure 2.1: Typical liquid structure factor $S(q)$ near freezing. The position of the second reciprocal lattice vector (RLV) set for BCC and FCC structures are also shown, location of the first peak is scaled to one.

volume change on freezing can vary from system to system significantly.

2.1 Early theories

The previously mentioned work of Lindemann was the first significant contribution to the study of melting, based on the absolute instability of the solid phase. Given the average square displacement $\langle u^2 \rangle$ the melting temperature T_m can be obtained as a shear instability in a self-consistent phonon theory. However, for a first order transition, this instability need not coincide with the relative thermodynamic stability of the solid and liquid phases.

Another approach is the direct calculation of the free energy of a model liquid and a model solid. At the melting temperature, these free energies become equal, though an accurate calculation is needed, which was demonstrated in [8] for the case of sodium. Unfortunately, this approach does not generalize well, the underlying physics of the transition remains poorly understood.

Lennard-Jones and Devonshire came forward with a cell-like model [9] for the liquid, which managed to reproduce the freezing transition, however the connection to a real liquid was not clear at all.

Considering melting as an instability to the proliferation of defects in a perfect crystal, a topological phase transition was identified as the mechanism behind melting in 2D systems, called the KTHNY-theory [10].

An early theory of the transition is by Kirkwood and Monroe [11], who relate

the appearance of the solid phase to an instability in the liquid. They have found below a certain temperature solid-like solutions in the one-particle density distribution $\rho(\boldsymbol{r})$ by considering the coupling of one particle to the rest of the particles as a coupling constant is turned on fully. The theory involves the atomic pair potential and the radial distribution function for all coupling strengths. An important drawback is, that since the theory is based on the pair potential, the transition is not formulated in a way that is universal among liquids. Another downside is, that the phase transition obtained for argon with FCC crystal structure, is close to second order.

2.2 The RY theory

T. V. Ramakrishnan and M. Yussouff (RY) pusblished an article with the title "First-principles order-parameter theory of freezing" in the journal Physical Review B in 1979 [12], which gave the first systematic derivation of a rigorous order parameter theory, that explained the *first order* solid-liquid phase transition with a symmetry change.

Simlarly to the Landau theory of phase transitions, the aim of an order parameter theory in statistical physics is to generalize the relevant equilibrium thermodynamic potential in terms of a set of coarse-grained variables, so that the calculation of equilibrium properties can be accomplished by free energy minimization. This procedure is followed in the technical review of the RY theory in App. A.2.

The important feature of the RY theory, is that it handles the density distribution of both liquid and solid phases in the same thermodynamic framework. Since the order parameter is the average one-particle density $\rho(\boldsymbol{r}) = \langle \sum_i \delta(\boldsymbol{r} - \boldsymbol{r}_i) \rangle$, without external potentials or walls the equilibrium liquid is represented by a constant value of the density. However, in the crystalline state the one-particle density is highly inhomogeneous. The critical realization in [12] is, that the density distribution of the crystalline state can be thought of as the density distribution of a liquid placed in a highly inhomogeneous external potential. The quality of the solid state and the solid-liquid transition is thus given in terms of the microscopic properties of the homogeneous liquid state. One needs to remember, though, that this fictitious external potential goes to zero in the equilibrium solid solution, the solid properties do not depend on it.

The result of the calculations (Eq. A.9) is the grand potential difference between solid and liquid phases at the same chemical potential and temperature

$$\beta\Delta\Omega\left(\{\xi_j\}\right) = N_0\left(\sum_i \frac{\xi_i^2}{2c_i} - (1-c_0)\left(\eta + \frac{\eta^2}{2}\right)\right), \tag{2.1}$$

given in terms of the liquid response function $c(k)$ evaluated at the RLVs of the solid structure, $\{c_i\}$. The order parameters $\{\xi_i\}$ are related to the Fourier amplitudes of the solid density pattern.

2.3 Interpretation of results

The interpretation of the grand potential difference Eq. 2.1 is, that relative to the homogeneous liquid state, there is a positive energy cost associated with the lattice periodic density modulations $\propto k_{\mathrm{B}}T\sum_i \frac{\xi_i^2}{2c_i}$, but at the same time condensation (an increase in density) takes place, which increases the pressure by $\Delta P \approx (\partial P/\partial\rho)\,\Delta\rho$ and helps to lower the overall energy cost by $-V\Delta P = -k_{\mathrm{B}}T\,(1-c_0)\,\eta$. Those amplitudes will be most effective in lowering the energy, which cause the most condensation, i.e. with a high value of the correlation function c_i. So a high degree of correlation is necessary to make $\Delta\Omega = 0$, i.e. to satisfy the freezing condition.

The input material property is a response function, the Fourier transform of the direct pair correlation function $c(k)$ of the homogenenous liquid. The zero wavenumber mode c_0 is related to the thermodynamic compressibility of the system, while the rest of the $\{c_i = c(K_i)\}$ values characterize structural two-point correlations. The compressibility is taken to be fixed near the transition temperature, thus the freezing condition is expressed in terms of the degree of correlations and not in temperature or pressure, this gives a kind of universality, system independence to the theory. A separate model is required for the modeling of correlations in terms of temperature or pressure.

2.4 Classical DFT

Classical density functional theory is the study of the statistical mechanics of classical condensed systems, in particular inhomogeneous liquids. The theory is formulated in terms of the excess free energy functional, which depends on correlation functions of the homogeneous state. It is basically a response theory, which predicts the inhomogeneous structure due to external causes, or in the case of the freezing transition, due to internal causes. In the most advanced cases, the excess functional has been derived (Fundamental Measure Theory - FMT [13]) from the known interaction between the constituent particles. Some advanced theories

(Weighted Density Approximation - WDA [14]) carry the thermodynamic properties of the liquid phase through realistic equations of state. In the simplest of cases, it is a low order approximation (RY [12]) and it is easily fitted to (computer) experiments.

The RY expression of the grand potential difference is slightly reformulated in the modern exposition of density functional theory (see Ref. [3]), where it is derived based on the Helmholtz free energy of the system. The RY functional is obtained in terms of the density field $\rho(\boldsymbol{r})$ instead of the amplitudes of its Fourier modes, see Eq. A.6. After the assumption of a perfect crystalline structure, the modern form of the RY DFT Eq. 2.2 becomes equivalent to the RY result of Eq. A.8 in every respect. I must mention, that the RY derivation (see App. A.2) is significantly more illuminating, than the modern formulation.

The functional is the sum of two parts. The first is a purely entropic contribution from the ideal gas free energy

$$F_{\mathrm{id}}[\rho(\boldsymbol{r})] = k_{\mathrm{B}}T \int \mathrm{d}\boldsymbol{r}\rho(\boldsymbol{r}) \left[\log\left(\Lambda^3\rho(\boldsymbol{r})\right) - 1\right] ,$$

where $\Lambda = h/\sqrt{2\pi m k_{\mathrm{B}}T}$ is the thermal de Broglie wavelength. The second is due to short range interactions of the particles, which can be approximated as a truncation of a correlation function hierarchy. It is expressed in terms of $\delta\rho(\boldsymbol{r}) = \rho(\boldsymbol{r}) - \rho_l$ and it is called the excess free energy

$$\begin{aligned} &F_{\mathrm{ex}}[\rho(\boldsymbol{r})] = F(\rho_l) - k_{\mathrm{B}}T \int \mathrm{d}\boldsymbol{r} c^{(1)}(\boldsymbol{r};\rho_l)\,\delta\rho(\boldsymbol{r}) - \\ &-\tfrac{1}{2}k_{\mathrm{B}}T \int \mathrm{d}\boldsymbol{r}\delta\rho(\boldsymbol{r}) \int \mathrm{d}\boldsymbol{r}' c^{(2)}(|\boldsymbol{r}-\boldsymbol{r}'|;\rho_l)\,\delta\rho(\boldsymbol{r}') . \end{aligned}$$

The grand potential difference is (formally) obtained through the Legendre transform of the Helmholtz potential

$$\begin{aligned} &\Delta\Omega[\rho(\boldsymbol{r})] = \Omega[\rho(\boldsymbol{r})] - \Omega[\rho_l] = \\ &= \Delta F_{\mathrm{id}} + \Delta F_{\mathrm{ex}} - \mu \int \mathrm{d}\boldsymbol{r}\left[\rho(\boldsymbol{r}) - \rho_l\right] . \end{aligned}$$

Finally, for the grand potential difference we obtain

$$\begin{aligned} &\Delta\Omega[\rho] = k_{\mathrm{B}}T \int \mathrm{d}\boldsymbol{r}\left[\rho(\boldsymbol{r})\log\left(\rho(\boldsymbol{r})/\rho_l\right) - \left(\rho(\boldsymbol{r}) - \rho_l\right) - \right. \\ &\left. -\tfrac{1}{2}\left(\rho(\boldsymbol{r}) - \rho_l\right) \int \mathrm{d}\boldsymbol{r}' c^{(2)}(|\boldsymbol{r}-\boldsymbol{r}'|;\rho_l)\left(\rho(\boldsymbol{r}') - \rho_l\right)\right] . \end{aligned} \tag{2.2}$$

Chapter 3

The PFC model

Under practical conditions, the crystallization of supersaturated or undercooled liquids starts by either heteroepitaxial growth or by heterogeneous nucleation on surfaces, which can include container walls and foreign particles. Elastic stresses can play a major role in determining the path to equilibrium in systems with broken translational symmetry. The *microscopic* description of these phenomena requires an atomistic approach. A theoretical modeling tool, called the phase-field crystal (PFC) model [1] was developed for such purposes.

Since its inception in 2002, the PFC model has inspired many and brought together an active community. It has become an umbrella term [2] for models that work with an atomistic particle density as the order parameter and approximate the Gaussian density distribution of single atoms in the crystal lattice with only a couple of Fourier-modes. This is in contrast to density functional theory (DFT), which aims to reproduce the Gaussian density profile closely, characterized by the Debye-Waller factor.

The reduction of the Fourier-spectrum of the order parameter results in an enormous computational advantage, when it comes to simulations. As an illustration, let us consider a DFT simulation that represents the atomic maxima faithfully. This might require 64 discretization points per unit cell, per dimension. The corresponding simulation in the PFC model requires usually only 8 points, thus in three dimensions a reduction of a factor of $(64/8)^3 = 512$ can be achieved in both memory requirement and computational time.

Another advantage of the PFC model is, that it can address freezing on a diffusive time scale [1] and can handle millions of particles easily [2]. However, to address the crystallization of molecular fluids, a hydrodynamic theory based on the PFC model has been put forward in Ref. [15], which we denote here as HPFC.

The PFC model combines the continuum level description of matter with an atomistic description of the ordered phases. It can be understood as a simple DDFT of classical particles [2]. It has previously been applied to address crystal nucleation [2, 16–19] and growth under various conditions [2, 20–23]. This model incorporates the description of several crystalline structures (BCC, HCP and FCC [23]), besides liquid and glass [24, 25] phases.

It is best to think of the PFC order parameter as a time averaged one particle number density, which becomes necessarily homogeneous in the liquid state (without external potentials), since liquids do not break translational symmetry. The crystalline state, however, will possess a finite number of symmetries, fully determined by the first reciprocal lattice vector (RLV) set of the given crystal structure. A finite amplitude of those Fourier modes will lead to a periodic pattern, whose maxima are associated with the equilibrium atomic positions.

In the original version of the theory, density being a conserved quantity, the time evolution of the closed system is described by overdamped diffusive dynamics, which is appropriate for the modeling of colloidal aggregation. However, for the study of equilibrium states or when the system is open for particle exchange, a non-conserved equation of motion can be used as well, we call this the pseudo time dependent Euler-Lagrange equation.

3.1 The origin of the PFC model

The Swift-Hohenberg (SH) equation [26], formulated for the study of the effect of noise on the convective instability (which is known as Rayleigh-Bénard convection) can be derived as a non-conserved Langevin-type evolutionary equation from a Lyapunov free energy functional. It is a prime example of a spatially extended, pattern forming dynamical system. Pattern formation in these systems is the result of instabilities of spatial operators, while nonlinearities provide the mechanism responsible for the saturation of the magnitude of the order paramter.

The PFC model was originally proposed based on the observation, that the Swift-Hohenberg equation produces periodic patterns, which can be interpreted as a collection of atoms. This periodic pattern minimizes the functional, which means, that deviations from the solid-like minimum energy configuration, have a positive energy cost. This is the reason, why the PFC model is capable of describing elastic deformations.

The SH form of the Lyapunov functional is the following

$$F[\psi] = \int \mathrm{d}\boldsymbol{r} \left\{ \frac{1}{2}\psi \left(-\epsilon + \left(q_0 + \nabla^2 \right)^2 \right) \psi + \frac{1}{4}\psi^4 \right\} , \tag{3.1}$$

where the order parameter $\psi(\boldsymbol{r})$ in the PFC model is interpreted as a scaled particle density, q_0 is a wavenumber usually set to $q_0 = 1$, which sets the periodicity of minimum energy configurations and the model parameter ϵ can be related to thermodynamic variables such as temperature, to control the phase transition between the liquid (homogeneous order parameter) and solid (periodic density). In the PFC context, the Lyapunov functional takes the place of the Helmholtz free energy of the system. The re-interpretation of the SH order parameter as a particle number density, warranted the use of the simplest, conserved evolutionary equation, the diffusion equation

$$\partial_t \psi = D\nabla^2 \frac{\delta F}{\delta \psi} ,$$

in which the diffusion constant D is usually set to $D = 1$, as it only affects the scaling of time.

In the case of the RB convection, the SH model describes a stationary, non-equilibrium state, while in the PFC interpretation, the model describes an equilibrium configuration of atoms. In the SH interpretation, ϵ is related to the Rayleigh number $\epsilon = \frac{\mathrm{Ra}-\mathrm{Ra}_c}{\mathrm{Ra}_c}$, itself proportional $\mathrm{Ra} \propto \Delta T$ to the temperature difference of the hot and cold plates. Convection and thus pattern formation is possible, when ϵ takes on positive values. The use of this parameter regime was inherited in the PFC model, solidification is modeled in the positive $\epsilon > 0$ range of values.

3.2 As an approximation to RY theory

Conceptually, it is somewhat difficult to explain the solid-liquid transition in terms of linear instabilities of a pattern forming model. Fortunately, an approximation scheme was identified, that links the PFC model to the more rigorous framework of the Ramakrishnan-Yussouff density functional theory.

In the grand potential difference Eq. 2.2 between a homogeneous liquid and a highly inhomogeneous crystalline state, the fractional density change n is introduced through $\rho(\boldsymbol{r}) = \rho_l (1 + n(\boldsymbol{r}))$, which becomes

$$\Delta\Omega[n] = \rho_l \int \mathrm{d}\boldsymbol{r} \left[(1 + n(\boldsymbol{r})) \log(1 + n(\boldsymbol{r})) - n(\boldsymbol{r}) - \frac{1}{2} n(\boldsymbol{r}) \int \mathrm{d}\boldsymbol{r}' \rho_l c^{(2)}(\boldsymbol{r} - \boldsymbol{r}') n(\boldsymbol{r}') \right] .$$

The RY DFT aims to succeed in a realistic description of the equilibrium solid-

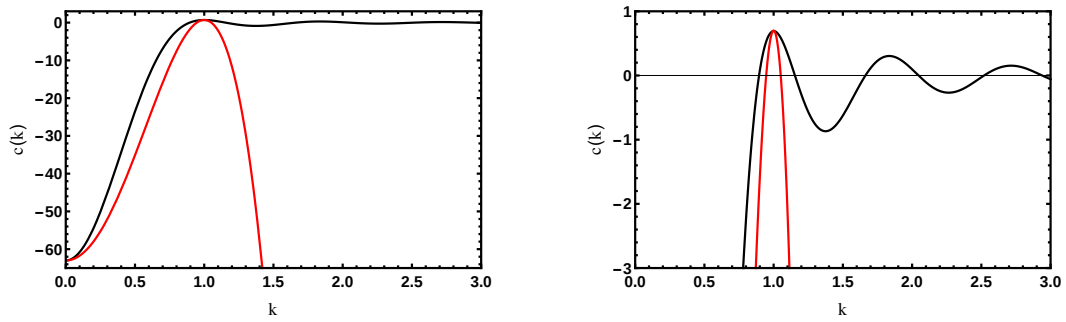

Figure 3.1: Comparison of direct correlation functions of the Percus-Yevick theory (shown as black) and the PFC approximation to it (colored red). The right panel is a magnified version of the left panel, to appreciate the oscillations around zero. The location of the first maximum is scaled to be at $k = 1$.

liquid density gap and the prediction of the location of the phase transition in terms of measurable correlations in the liquid state. The use of correlations as the basis for the theory gives it a system independent nature, as the results are not formulated in terms of pair potentials, which vary from system to system.

Two critical approximations set the PFC model apart from the Ramakrishnan-Yussouff theory. The liquid structure function pictured in Fig. 2.1, is connected to the direct correlation function through $S^{-1}(k) = 1 - c(k)$. Theoretically, all values of $S(k)$ and conversely $c(k)$ evaluated at the RLVs $k = \{|\boldsymbol{K}_i|\}$ of the solid phase would contribute to the grand potential difference and determine the location of the phase transition. The first approximation of the original PFC model is illustrated in Fig. 3.1, the Fourier transform of the liquid direct correlation function is approximated with a quartic expression

$$c_{\mathrm{PFC}}(k) = c_q + (c_0 - c_q)\left(1 - \left(\frac{k}{q}\right)^2\right)^2 . \tag{3.2}$$

The location of the first maximum q and the value of $c(k)$ at $k = 0$ and $k = q$ can be fitted in this way.

Liquid state theory is the first-principles approach to the calculation of the equation of state of real liquids and the study of correlations in terms of the pair- or multi-body potentials of the constituent liquid particles. The Percus-Yevick theory gives the analytical direct correlation function of the hard-sphere (HS) system in terms of its density. An important feature is, that as the density is increased, the maxima and especially the first maximum of $c_{\mathrm{PY}}(k)$ shifts to larger values of the

wavenumber, also the peaks and troughs get more pronounced. The connection between liquid density and the location and value of the first maximum in the direct correlation function is entirely neglected in the PFC model. The fitting parameters in Eq. 3.2 are handled independently from the liquid density, they were once connected to.

The lower the liquid density is, the smaller the oscillations in the $c\left(k\right)$ direct correlation function are around the zero correlation value, beyond the first maximum. The modeling of our ignorance of a system's correlations would correspond to the zeroing-out of the $c\left(k\right)$ function above a certain q_0 wavenumber, $c\left(k > q_0\right) = 0$. An approximation of this sort to the Ramakrishnan-Yussouff-type DFT theory exists [12], that still reproduces realistic solid density distributions, compatible with the wavenumber dependence of the solid Fourier-amplitudes $\log\left(A_{K_i}\right) \propto -K_i^2$, determined by a corresponding Debye-Waller factor. The quartic expression of Eq. 3.2 tends to $c\left(k \to \infty\right) \to -\infty$ negative infinity, intead of zero for large values of the wavenumber. Such a $c\left(k\right)$ function in the grand potential (Eq. 2.2) would associate an increasing energetic penalty to finite solid state Fourier-amplitudes for wavenumbers even as small as the second RLV set. This would make the solid-like local minimum in the grand potential disappear and forego the possibility of a solid-liquid phase transition.

The second approximation of the PFC model destroys the physical connection between the solid-like Fourier-amplitudes and the wavenumber, which comes from the purely entropic, ideal-gas term in the grand potential. The logarithmic expression is simply replaced with a fourth-order Taylor expansion $\left(1+n\right)\log\left(1+n\right) - n \to \frac{n^2}{2} - \frac{n^3}{6} + \frac{n^4}{12}$ and the real-space counterpart of Eq. 3.2 is introduced with $q = 1$, $\hat{c}_{\mathrm{PFC}} = c_1 + \left(c_0 - c_1\right)\left(1 + \nabla^2\right)^2$ which finally produces the PFC form of $\Delta\Omega$

$$\Delta\Omega[n\left(\boldsymbol{r}\right)] = \rho_l \int \mathrm{d}\boldsymbol{r} \left[\frac{1}{2}n^2 - \frac{1}{6}n^3 + \frac{1}{12}n^4 - \frac{1}{2}n\left(c_1 + \left(c_0 - c_1\right)\left(1+\nabla^2\right)^2\right)n\right] . \quad (3.3)$$

The truncation of the Taylor expansion of the direct correlation function (which amounts to a gradient expansion in real-space) together with the truncation of the expansion of the ideal-gas term, makes solid-like solutions with only a couple of Fourier-amplitudes possible. This approach eliminates the predictive nature of DFT, though the PFC model still retains the essential features of the solid-liquid transition, while also being computationally efficient at the same time.

3.3 Clarification to the PFC functional

Order parameter (OP) theories postulate, that the OP completely determines the state of the system. There is an associated, generalized thermodynamic potential, which is a function of the OP. If the OP is a function of space (inhomogeneous ground state), the thermodynamic potential takes on the form of a mathematical functional, to account for the energetic contribution of spatial variations in the OP. Possible thermodynamic potentials are mentioned in App. A.1.4 and their physical meaning is discussed. The thermodynamic principle, which states that entropy increases in an isolated system during spontaneous processes, can be used to formulate the generalized thermodynamic potentials. Depending on which thermodynamic variable is kept fixed by external conditions, the entropic maximum principle can be expressed as a free energy minimum principle, as explained in App. A.1.6.

Let us take the RY theory as a concrete example. The expression Eq. 2.2 is a functional of the inhomogeneous density $\rho(\boldsymbol{r})$. Equilibrium states of the modeled system correspond to local or global minima of the functional, variations in the order parameter around the equilibrium distribution $\rho^*(\boldsymbol{r})$, do not change the value of the functional to first order $\delta\Delta\Omega[\rho^*(\boldsymbol{r})] = \lim_{\epsilon\to 0}\{\Delta\Omega[\rho^*(\boldsymbol{r}) + \epsilon q(\boldsymbol{r})] - \Delta\Omega[\rho^*(\boldsymbol{r})]\} = 0$. Aside from some other extrema, such as maxima or saddle points, any other distribution of the OP corresponds to a *non-equilibrium* state.

Exclusively at the minimum energy configurations does the functional become equal to its corresponding thermodynamic potential. At these minima, the value of the functional and so the thermodynamic potential is determined by the *natural variables* of the potential, which are external constraints on the minimization. It is important to realize, that these external thermodynamic variables control the parametrization of the functional and thus remain constant during the non-equilibrium evolution.

How do we know, that the RY theory is a model for the generalized grand potential difference? Its order parameter is the inhomogeneous atomic number density (N/V), the conjugate variable of which is the chemical potential. It is the grand potential, which has the natural variables (T, V, μ), thus Eq. 2.2 describes an isothermal system, at constant volume and in contact with a particle reservoir at chemical potential μ. In the RY model, the exact form of the $c(k)$ direct correlation function depends on these natural variables and so does the functional $\Delta\Omega = \Delta\Omega[\rho](T, V, \mu)$. The functional connects the equilibrium liquid and solid

minima at the same values of temperature and chemical potential. At these minima the functional coincides with the thermodynamic definition $\Delta\Omega\left[\rho^*\right] = -V\Delta P$, i.e. the negative of the pressure difference, relative to the liquid pressure. The phase boundary is signaled by the absence of this pressure difference, as all intensive thermodynamic variables between solid and liquid become equal.

The PFC approximation (Eq. 3.3) to the RY DFT preserves the aforementioned qualities, however these are not appreciated in the PFC community. Since the SH form of the PFC functional [1] has appeared originally, the later discovered connection to DFT (see Ref. [2]), possibly, was biased towards the previous interpretation of the theory. The situation is such, that Eq. 3.3 is considered by the community to be a functional of the generalized *Helmholtz* free energy. Due to this misunderstanding, instead of searching for equilibrium solutions via $\frac{\delta\Delta\Omega}{\delta n} = 0$ and changing the parametrization of $c\left(k\right)$ to account for the (implicit) change in chemical potential, the Euler-Lagrange equation is written in the form $\frac{\delta\Delta F}{\delta n} = \mu$. A free parameter, called the chemical potential is thus explicitly introduced.

A comparison of the SH form (Eq. 3.1) and the RY form (Eq. 3.3) initially reveals differences in the coefficients of higher order terms, which are motivated (see Ref. [2]) by the argument, that low order contributions of higher order correlations (which are not taken into account in the formulation) influence these coefficients, so these coefficients can be considered as fitting parameters. A closer look reveals a strange correspondence between model parameters $c_1 - c_0 \equiv 1$, $1 - c_1 \equiv -\epsilon$ or expressed differently

$$c_0 \equiv \epsilon,\; c_1 \equiv 1 + \epsilon\,.$$

Mentioned in Sec. 3.1 and as can be seen on the phase diagram in Fig. 7.7, the positive range of ϵ leads to the stability of periodic phases. The value of ϵ determines the solid-liquid density gap and interface properties (see Sec. 3.4). Usually, the interval $\epsilon \in (0, 0.75]$ is explored. These values of ϵ are in grave contradiction to the physical meaning of the values c_0, c_1 of the direct correlation function. A couple of examples from Ref. [12] for $c_0 = c\left(k = 0\right)$: $c_0\left(\text{argon}\right) = -18.9$, $c_0\left(\text{sodium}\right) = -40$ and $c_0\left(\text{HS}\right) = -49$, these numbers are mainly known from compressibility κ measurements, since $\kappa^{-1} = \left(1 - c_0\right)\rho_l k_\text{B} T$. The other parameter $c_1 = c\left(k = k_\text{max}\right)$ is the height of the first maximum, which is always less than one $c_1 < 1$, otherwise the structure factor $S\left(k\right)$ would diverge, which is not compatible with a stable liquid. The corresponding c_1 values in the SH PFC model are always greater, than one. The SH form connects these parameters through ϵ, however, physically these two parameters c_0 and c_1 are not connected with one another directly.

In the RY interpretation, the stable liquid phase always corresponds to the order parameter value $n_l = 0$ (zero fractional density change) and the (implicit) chemical potential is controlled via the strength of the liquid phase direct correlation c_1, while c_0 can be set to a constant value characteristic to the given liquid, which changes little near the phase transition. The liquid density is present only (implicitly) in the direct correlation function (calculated from liquid state theory) $c = c(k; \rho_l)$ as a parameter, solely the solid-liquid fractional density change and the pressure difference is determined by the RY model.

However, in the SH interpretation, due to the presence of the free parameter μ, it is possible to use unrealistic values of the direct correlation function (as determined by ϵ) and still obtain solid-liquid phase coexistence. The connection between the strength of correlations and liquid density is completely lost, instead μ changes the liquid density. This is the reason, why the liquidus line is located at negative fractional densities $n_l < 0$. As the model parameter approaches zero $\epsilon \approx 0$, the phase transition loses its first order character and $\epsilon = 0$ denotes a critical point. In the RY interpretation the phase diagram is one-dimensional, once the compressibility is set via c_0, the remaining parameter c_1 tunes the pressure difference between the equilibrium phases. The parameter c_0 controls interface characteristics and the equilibrium density gap.

Another important aspect of the RY theory is, that while it is a nonlinear theory in the mathematical sense, meaning that the equilibrium solid order parameter is the solution to a nonlinear integral equation, physically, it is the linear response theory (see App. A.2.3) of the homogeneous liquid to an external potential, solely characterized by its direct correlation function $c(k)$. The RY level of approximation to DFT does not involve the equation of state of the liquid and the response function of the theory, namely $c(k)$ is independent of local density changes. More involved density functional theories exist, such as the Weighted Density Approximation [14], which does build upon the equation of state of the liquid phase and the Helmholtz free energy together with the chemical potential are actually accessible. The PFC approximation obviously inherits the limitations of the RY theory, so one needs to remember, that no thermodynamic insight can be gained by changing the model parameter ϵ (which controls both c_0 and c_1) freely, without concern to the liquid density and pretending that the model contains a liquid equation of state.

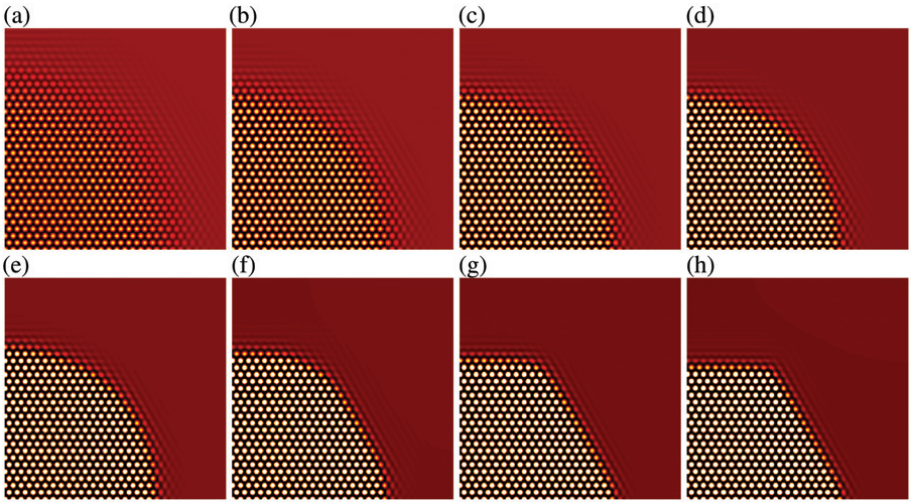

Figure 3.2: Equilibrium crystalline density profiles, so called Wulff shapes, reflecting the anisotropy of the crystal-liquid interface, shown as a function of the reduced temperature ϵ, for the same crystalline fraction of 0.3. (a through h): $\epsilon = 0.05$, 0.1, 0.15, 0.2, 0.25, 0.3, 0.325 and 0.35. The interface thickness decreases, while the anisotropy increases with an increasing distance from the critical point (located at $\epsilon = 0$).

3.4 Solid-liquid interface anisotropy

In the PFC model, as reviewed in Ref. [2], the thickness and the anisotropy of the solid–liquid interface vary with the reduced temperature ϵ, between essentially an isotropic and broad interface (near the critical point, $\epsilon = 0$) and a strongly anisotropic and sharp interface (far from the critical point, $\epsilon > 0$). Accordingly, as seen in Fig. 3.2, the two dimensional equilibrium shapes vary between circular and hexagonal. For the three dimensional equilibrium crystal shapes see Ref. [27].

As a result, by the choice of ϵ, one may select qualitative features characteristic to different classes of materials. In the small ϵ range ($\lesssim 0.25$) the model provides a small anisotropy and a broad solid–liquid interface, characteristic to metals. In the large ϵ range ($\gtrsim 0.5$), the interface is sharp on the atomic scale and strongly faceted, mimicking covalent systems.

Chapter 4

Time evolution

Thermodynamic potentials, which are state functions of homogeneous matter, are generalized in terms of order parameters (OPs), that drive the transformation under fixed external conditions. The choice of the OP determines the kind of irregularities and the possible local equilibrium states, that can be reached during phase transformation. It is paramount, to be able to faithfully represent the important aspects of the microstructure and to use realistic time evolution equations, since the final microstructure is often determined by diffusional and morphological instabilities during non-equilibrium evolution. To account for this, while retaining the essentially thermodynamic description, the concept of local thermodynamic equilibrium is introduced.

This approach involves decomposing matter into macroscopically small, but still microscopically large volume elements, that each behave according to their thermodynamic state function. Inhomogeneities in the respective intensive thermodynamic variables generate currents proportional to gradients in the intensive variables, as the system tends to a lower free energy state by elimination of inhomogeneities. However, the system may be trapped in various states, that represent local minima of the free energy functional and the lowest energy state compatible with the prescribed boundary conditions might not be reached. The choice of the time evolution equation for the order parameter and other auxiliary fields is an important one in the study of phase transformations and microstructure formation.

4.1 Euler-Lagrange equation

Stable equilibrium distributions of the order parameter $\psi(\boldsymbol{r})$ correspond to minima of the grand potential $\Omega[\psi(\boldsymbol{r})] = F[\psi(\boldsymbol{r})] - \mu \int \mathrm{d}\boldsymbol{r}\psi(\boldsymbol{r})$. At these states ψ^*, which

are the solutions to the Euler-Lagrange (EL, ELE) equation (mathematically, a boundary value problem), the first variation of the functional goes to zero

$$\frac{\delta F}{\delta \psi}\bigg\rceil_{\psi^*} - \mu = 0\,,$$

signaling the lack of driving force. The chemical potential μ sets the average particle density.

In several cases it is satisfactory to study the ELE exclusively, for example, when

- locating the phase boundary, i.e. with changing model parameters finding the coexisting densities,
- studying the equilibrium interface free energy between coexisting phases,
- finding the nucleus, the critical size cluster, which is associated with a saddle point in classical nucleation theory (CNT).

In certain cases, besides the global minimum associated with the given boundary conditions, the free energy functional also possesses local minima (related to the so called free energy landscape paradigm [3]), thus it is *physically* motivated to transform the boundary value problem of the ELE into an initial value problem. A non-conserved evolutionary equation in fictitious time is constructed that follows the steepest descent on the free energy landscape to a local minimum. In this way, by carefully choosing the initial value of the order parameter field $\psi_0(\boldsymbol{r})$ one gains control over the selection of the equilibrium state. The ELE is thus given by

$$\partial_t \psi(\boldsymbol{r}, t) = -\left(\frac{\delta F}{\delta \psi} - \mu\right),\ \psi(\boldsymbol{r}, t=0) = \psi_0(\boldsymbol{r}) \tag{4.1}$$

It must be born in mind, that the above equation is non-conservative, meaning that even if the order parameter ψ represents a conserved quantity (e.g. particle number density) this equation in its evolution is not limited by the constraint of local (and global) conservation of density. The parameter μ, which is the chemical potential of the system sets the average density. This kind of equation is called "Model A" in the Hohenberg-Halperin [28] classification.

4.2 Diffusive equation of motion

When working with the atomic number density as the order parameter, the local change in density being a conserved quantity physically can only happen via currents transporting matter from one volume element to a neighboring one due to differences in the chemical potentials in these volume elements.

The simplest conserved equation of motion (EOM) is "Model B" in the Hohenberg-Halperin [28] classification. The chemical potential is introduced as the functional derivative of the relevant free energy $\mu = \frac{\delta F}{\delta \psi}$ providing the local driving force for mass transport, gradients in this chemical potential give rise to currents according to linear response theory $\boldsymbol{j}_\psi = -D\nabla\mu$ that transport the conserved order parameter ψ through the continuity equation $\partial_t \psi + \nabla \cdot \boldsymbol{j}_\psi = 0$, which becomes the diffusion equation when the diffusion coefficient is a constant

$$\partial_t \psi = D\nabla^2 \mu \,. \tag{4.2}$$

This EOM is an overdamped evolutionary equation, meaning it has been derived for particles suspended in a carrier fluid, such as colloidal suspensions. This EOM is also motivated on the ground that approximations to DDFT lead [2, 29] to this equation. When coupled with PFC thermodynamics we frequently call this the DPFC model.

4.3 Fluctuations in continuum models

The equilibrium order parameter distribution takes the free energy functional to its minimum, where thermodynamic variables, which characterize the macrostate of the system are well defined. However, the free energy functional is defined for arbitrary distributions of the order parameter, where the value of the functional is not related to thermodynamic macrostates, these are non-equilibrium states with a driving force towards equilibrium.

Metastable phases are local equilibrium states of the functional. The order parameter characteristic to an undercooled liquid takes on a constant value, which would remain unchanged indefinitely, as the system has no way of exploring its order parameter space and leave the local minimum. Activated processes like nucleation, that must cross an energy barrier do not take place in this uniform liquid, unless thermal fluctuations are incorporated into the EOM in the form of Langevin noise. Although, this approach emulates nucleation, it is not devoid of conceptual

issues, as thoroughly discussed in the existing literature [30–32].

If we consider the particle density as a quantity that is averaged over an ensemble, then the free energy encompasses all feasible fluctuations. Therefore, introducing noise into the EOM implies that a portion of the fluctuations is counted twice. However, if we presume that the number density is a quantity that is averaged over time, then it seems rational to include noise in the EOM to simulate thermal fluctuations. This way, both crystal nucleation and capillary waves at the crystal-liquid interface are automatically taken care of.

The form of the Langevin-type diffusive EOM is the following

$$\frac{\partial \psi}{\partial t} = \nabla^2 \left(\frac{\delta F}{\delta \psi} + \zeta \right) \tag{4.3}$$

where ζ represents a Gaussian random field with zero mean and correlation given by

$$\langle \zeta (\boldsymbol{r}, t) \, \zeta (\boldsymbol{r}', t') \rangle = A_{\text{noise}} \delta (\boldsymbol{r} - \boldsymbol{r}') \, \delta (t - t') \ .$$

It is worth mentioning, that in most dynamic PFC investigations, a spatially colored noise is utilized in the EOM, obtained by filtering out the unrealistic atomic level fluctuations of very short wavelength. The noise is generated in Fourier-space and a high wavenumber cutoff is applied $\hat{\zeta} (|\boldsymbol{k}| > k_0, t) = 0$, here k_0 represents the location of the maximum in $c(k)$, the direct correlation function.

4.4 Generalized equations of motion

In the statistical mechanical description of condensed matter, the large number of individual degrees of freedom evolving according to Hamiltonian dynamics, are replaced with coarse-grained variables, that describe collective motions. In most systems, a separation of timescales can be observed, collective motions usually proceed on a longer timescale, because a large number of particles are involved or because there are conservation laws associated with those coarse-grained variables, like particle density, momentum density or energy density. The evolution equations of such slow modes are termed ”generalized hydrodynamic” equations.

The evolution equation used with PFC functionals is primarily the diffusion equation Eq. 4.2, sometimes simply referred to as EOM, which is applicable for particles suspended in a carrier fluid, as it describes overdamped dynamics, when particle acceleration is inconsequential and the slow, dissipative dynamics is of primary interest. This EOM does not support propagating modes, except, that at

large undercoolings, as the solid-liquid density gap approaches zero, the solid-liquid front advances with $\propto t$ and a so-called "fast growth mode" [2] can be observed. This EOM does not fit the definition of a hydrodynamic equation.

To more closely model the time evolution of the particle distribution, when no carrier fluid is present, as in the case of simple liquids, the momentum of particles cannot be ignored. Those equations, that contain in some form the velocity or momentum field as a first class variable, are called hydrodynamic equations of motion. In these dynamical equations the free energy does not approach equilibrium monotonously, the thermodynamic force acts as a reactive force instead of a dissipative one and these equations support propagating wave phenomenon.

4.4.1 Coupling to propagating modes

The strong desire for the computational modeling of crystallization from the undercooled melt on the molecular scale drives the development of models, that are capable of addressing a multitude of phenomena at once. These include phase coexistence, the realistic description of the solid-liquid interface and its anisotropic surface free energy. The incorporation of fluctuations of the solid-liquid interface and fluctuations in the bulk phases. The crystal carrying the proper symmetry, without the prior prescription of possible atomic positions and having propagating phonon modes, without an explicit displacement field. Capability of describing plastic deformations besides elastic ones. Possessing Galilean-invariance, which aids the mobility of grains, because they are no longer coupled to a carrier fluid, as opposed to the overdamped case.

The above requirements warrant an atomistic, free energy based description of the crystalline phase, which is provided by classical DFT. Equilibrium, static DFT was extended based on first principles to model the dynamics of Brownian liquids and colloidal systems, see Refs. [30, 32–34], this was termed Dynamical DFT (DDFT). Later in Ref. [35], the dynamics was generalized for dense atomic liquids. A combined description of molecular fluids and colloids appeared in Ref. [36]. Hydrodynamic transport equations, without the nonlinear momentum advection term have also been tried in Refs. [37, 38]

The high accuracy of DFT modeling carries a high cost of numerical computation. In the quest of modeling with as little resources as possible (which thus increases problem size), the cost-effective PFC functional became the subject of attempts in coupling atomistic thermodynamics to hydrodynamic density transport. Some models use a second time derivative to model propagating modes, but

without the complications of velocity or momentum fields, see Ref. [39]. A simple advection model was coupled to the PFC functional in Ref. [40] to describe particle motion in a carrier fluid. No comprehensive demonstration of growth and elastic processes have appeared in the literature until the publication of Ref. [15].

4.4.2 Dynamical coarse-graining

The thermodynamic and hydrodynamic responses of fluids are frequently modeled by the continuum theory of fluctuating nonlinear hydrodynamics (FNH) [41], which is the extension of traditional compressible hydrodynamics to the mesoscale, by incorporating thermal fluctuations according to the fluctuation-dissipation theorem. It is shown in Ref. [42], that FNH can be explicitly mapped to MD simulations.

The FNH equations are stochastic partial differential equations, that introduce stochastic fluxes into the conservation equations of momentum and energy to represent fluctuations around averages. The incorporation of these fluctuations makes it possible to study a diverse collection of mesoscopic phenomena, such as diffusive mixing of miscible fluids, capillary waves at fluid-fluid interfaces, Rayleigh-Taylor instability, droplet spreading or the dynamics of nanoparticles.

FNH forms the basis of the nonlinear hydrodynamic theory of crystallization, published in Ref. [15]. However, only isothermal processes are considered, similarly to basically all applications of the PFC model. Thus, the energy transport equation of the FNH model is neglected, the remaining conservation equations are the following

$$\begin{aligned} \partial_t \boldsymbol{p} + \nabla \cdot (\boldsymbol{v} \circ \boldsymbol{p}) &= \nabla \cdot [\boldsymbol{R}(\rho) + \boldsymbol{D}(\boldsymbol{v}) + \boldsymbol{S}] \\ \partial_t \rho + \nabla \cdot \boldsymbol{p} &= 0\,. \end{aligned} \tag{4.4}$$

Here, $\boldsymbol{p}$ denotes the momentum density, $\boldsymbol{v}$ the velocity field and ρ the particle number density. The tensor $\boldsymbol{R}$ is the reversible stress tensor, it is responsible for the reactive forces that drive the dynamics (normal modes propagate). Following Ref. [43], thermodynamics is coupled through this term, via the equation

$$\nabla \cdot \boldsymbol{R} = -\rho \nabla \frac{\delta F}{\delta \rho}$$

where $F = F[\rho]$ is the thermodynamic potential, a functional of the inhomogeneous density. In Ref. [15] a constant mobility approximation is introduced in the above equation $\nabla \cdot \boldsymbol{R} = -\rho_0 \nabla \frac{\delta F}{\delta \rho}$ where ρ_0 is a constant average density.

The tensor $\boldsymbol{D}$ represents dissipative stresses, it is responsible for the approach to thermodynamic equilibrium, the dissipation of the free energy (normal modes decay). It is of the same phenomenological form, that is familiar from the Navier-Stokes equation

$$\nabla \cdot \boldsymbol{D} = \mu_{\mathrm{S}} \nabla^2 \boldsymbol{v} + \left(\mu_{\mathrm{B}} - \frac{2}{3} \mu_{\mathrm{S}} \right) \nabla \left(\nabla \cdot \boldsymbol{v} \right)$$

where the transport coefficients are the bulk μ_{B} and shear μ_{S} viscosities (these are not related to the chemical potential). The momentum field is directly coupled to a stochastic variable, the noise tensor $\boldsymbol{S}$ whose correlations follow the fluctuation-dissipation theorem according to

$$\left\langle S_{ij}\left(\boldsymbol{r},t\right) S_{kl}\left(\boldsymbol{r}',t'\right) \right\rangle = 2 k_{\mathrm{B}} T \mu_{\mathrm{S}} \left[\left(\delta_{ik}\delta_{jl} - \delta_{jk}\delta_{il} \right) + \left(\frac{\mu_{\mathrm{B}}}{\mu_{\mathrm{S}}} - \frac{2}{3} \right) \delta_{ij}\delta_{kl} \right] \delta\left(\boldsymbol{r}-\boldsymbol{r}'\right) \delta\left(t-t'\right) .$$

Physically, the Langevin-type noise $\boldsymbol{S}$ makes no sense on the sub-atomic scale. Since in practice, $\boldsymbol{S}$ is generated in Fourier-space, it is easy to filter out components above a wavenumber $k_0/2$, related to the wavenumber of the atomic periodicity k_0, so the spectrum of $\boldsymbol{S}$ becomes zero above that $\boldsymbol{S}\left(|\boldsymbol{k}| > k_0/2\right) = 0$.

The above equations describe the evolution of fluctuating fluid phases, when the correct thermodynamic functional is selected (e.g. gradient-squared theory with a double well potential). A serious difficulty hides in the above equations, when the thermodynamics is taken to be the PFC equation of state. Because of the atomistic nature of the order parameter (the density), the above equations would operate on the atomic scale. According to Ref. [44] the length scale of the validity of the Navier-Stokes equations is placed above a 100 molecular diameters. Below this scale, the dissipation mechanism and the validity of the NS equations are highly questionable.

Another issue is, that in DFT the equilibrium crystalline density is well approximated by narrow Gaussian functions, centered around the average position of atoms. These functions are highly inhomogeneous and very close to zero halfway between atomic positions. In the PFC model, while the solid solution contains fewer Fourier-modes than in DFT, additional problems with the positivity of the density arise. The usual connection between momentum density and velocity cannot be inverted to get $\boldsymbol{v} = \boldsymbol{p}/\rho$.

The resolution comes in the form of a dynamic coarse-graining procedure, which provides a more macroscopic derivation of the velocity field. The microscopic particle density ρ and momentum density $\boldsymbol{p}$ are coarse-grained, i.e. a volume averaging is applied, thus the lattice periodic components are removed from their spectra. The velocity field is constructed in terms of these coarse-grained quantities simply

as

$$\boldsymbol{v}\left(\boldsymbol{r},t\right)=\frac{\left\langle \boldsymbol{p}\left(\boldsymbol{r},t\right)\right\rangle }{\left\langle \rho\left(\boldsymbol{r},t\right)\right\rangle } \tag{4.5}$$

where $\langle . \rangle$ denotes the coarse-graining operator, which is implemented as a Gaussian-filter in Fourier-space, it is equivalent to the real-space convolution of its argument with a Gaussian kernel of variance $\sigma = 2\sigma_0$ where $\sigma_0 = 2\pi/k_0$ is the lattice constant.

The exact form of the PFC functional coupled with FNH is

$$\frac{F}{n_0 k_{\mathrm{B}} T}=\int \mathrm{d}V\left[\frac{1-c_0}{2}n^2-\frac{a}{6}n^3+\frac{b}{12}n^4-\frac{C_2}{2}\left(\nabla n\right)^2-\frac{C_4}{2}\left(\nabla^2 n\right)^2\right]. \tag{4.6}$$

The order parameter is the fractional density change $n = (\rho - \rho_0)/\rho_0$, where ρ_0 is a reference density. The parameter c_0 is related to the compressibility of the liquid $\kappa^{-1} = (1 - c_0)\,\rho_0 k_{\mathrm{B}} T$ and C_2, C_4 determine the crystalline elastic response and lattice constant. In the small order parameter limit, the speed of sound c_{S} is given in the liquid phase by $c_{\mathrm{S}}^2 = (1 - c_0 - a\overline{n} + b\overline{n}^2)\, k_{\mathrm{B}} T/m_0$ with m_0 being the atomic mass, and a, b are free parameters and $\overline{n}$ is the average fractional density change in the homogeneous liquid.

The merits of the above described model have been demonstrated in Ref. [15] in simulations:

- Crystalline clusters, perturbed by a displacement field as the initial condition, have shown elastic behavior similar to a harmonic lattice. Vibrations around the equilibrium atomic positions were observed, that slowly decayed in time. The transversal and longitudinal phonon spectra were determined, that showed excellent agreement with classical theory, for phonon wavelength $\lambda > 20\sigma_0$, i.e. above 20 lattice constants. Longitudinal wave propagation was found to be $\sqrt{3}$ times faster than transversal propagation.

- Steady front propagation was observed. In this case, the solid-liquid density gap requires density transport from the far field liquid. The velocity field, generated through the long-wavelength equation of state is responsible for the decrease of the far field density and the transport of matter to the solidification front. This decrease in the far field travels at the speed of sound. When the boundary of the simulation is reached, this travelling density gap is reflected. After it has reached the solidification front, steady state growth will proceed at a slower pace, since the front now needs to propagate in a less dense liquid, this equals to lower undercooling.

- The Fourier-transform of the interface position $h(x,t)$ follows a wavenumber dependent variance $\left\langle h(q)^2 \right\rangle = \frac{k_B T}{q^2 \tilde{\gamma} L}$, where $\tilde{\gamma}$ is the interface stiffness. This is the measure of the capillary wave spectrum, which has been determined from simulations and showed good agreement with this theoretical expectation.

- In Ref. [45], the kinetic coefficient K_{sol} relating growth velocity $v_{\text{sol}} = K_{\text{sol}} \Delta\mu$ to temperature (thus undercooling), has been linked to the shear viscosity, through the expression $K_{\text{sol}} \propto \mu_{\text{s}}^{-\xi}$. What is more, it was suggested that the exponent ξ is dictated by the fragility of the liquid. It was found, that the greater the fragility, the larger the difference $1 - \xi$. Fragility is a measure of the deviation of the temperature dependence of the viscosity of glass forming liquids from the Arrhenius-type behavior. The breakdown ($\xi \neq 1$) in fragile liquids between growth kinetics and viscosity has been subsequently linked to the manifestation of heterogeneous dynamics in the supercooled liquids. In Ref. [15] simulations confirmed a scaling close to $K_{\text{sol}} \propto \mu_{\text{s}}^{-1}$ over a large range of shear viscosities. This indicates the lack of fragility in the type of liquid the HPFC model manifests. A weak dependence of the growth velocity on the bulk viscosity has also been measured, a change in bulk viscosity of a factor of 16 resulted in a corresponding change in growth coefficient of a factor of 2.5.

4.4.3 Incompressible density transport

Motivated by the desire to study nucleation and grain growth under convection (see Sec. 6.3) we have experimented with the HPFC model of Sec. 4.4.2 to investigate such a scenario. Our efforts in trying to establish a flow field, which would transport single crystals in the liquid phase, have met with disappointment.

The use of hydrodynamic EOMs is preferred, mainly because it provides fast relaxation of the density, due to not being limited by overdamped density transport. We are seeking a model, in which the velocity field is a principal variable, so that it would make the displacement of solid objects, like crystal grains in the liquid possible. The failure of the HPFC model propelled us to formulate another hydrodynamic equation of motion coupled to PFC thermodynamics, it was recently published in Ref. [46]. We call our model here, the incompressibly advected HPFC model, INCA-HPFC for short.

This new EOM is based on the convective formulation of the incompressible Navier-Stokes equation. Unlike in the dynamical coarse-graining procedure as used in the HPFC model to formulate a velocity field, we have *based* our EOM around

an incompressible velocity, which is responsible for the large scale displacement of the medium. A separation of currents were devised, based on the observation, that the Navier-Stokes equation already accomplishes a scale separation in the form of the incompressibility condition, as it excludes dynamical density variation. We have separated the velocity field into two parts $\boldsymbol{v} = \boldsymbol{u} + \boldsymbol{g}$, $\boldsymbol{u}$ is responsible for the advection of the density distribution, while $\boldsymbol{g}$ carries out the local pattern evolution and compressible microscopic density propagation.

We review its derivation briefly. First, we apply the Helmholtz decomposition to the velocity field. Here, $\boldsymbol{u}$ denotes the divergence free vector field and $\boldsymbol{g} = \nabla\phi$ is a rotation free field. Thus, the equation $\nabla \cdot \boldsymbol{v} = \nabla^2\phi$ needs to be satisfied, which is easily solved $\hat{\phi}_{\boldsymbol{k}} = (\boldsymbol{k} \cdot \hat{\boldsymbol{v}}_{\boldsymbol{k}}) \,/\, (\mathrm{i}k^2)$ by Fourier transformation. The momentum density must have the form $\boldsymbol{p} = \rho\boldsymbol{v}$ when $\boldsymbol{v}$ is a proper frame velocity, or equivalently $\boldsymbol{p} = \rho\boldsymbol{u} + \rho\boldsymbol{g}$. Here, we make our first assumption, which is that $\rho\boldsymbol{g}$ is replaced with $\rho_0\boldsymbol{g}$, ρ_0 being the average density.

The compressible Navier-Stokes equation (or the more microscopic description of fluctuating nonlinear hydrodynamics) is a coarse-grained, local equilibrium description of matter (see the introduction in Sec. 4), which handles small variations in particle density, the smallest of control volumes still contain a large amount of particles. The coupled equation of state determines the thermodynamic driving force towards homogeneity, i.e. the response function, compressibility determines the scale of density fluctuations. In a microscopic theory, like DFT, the equilibrium density distribution in the solid phase is highly inhomogeneous, Gaussian spikes represent the probability density of atoms with a close to zero value between them. In the PFC approximation of this density, represented by only a few Fourier modes, values can become even negative between atoms. While in the overdamped limit this causes no complications, an EOM based on Newton's equation for a medium suffers from the direct use of this approximated density. The solution to this problem is the reason behind the crude approximation of $\rho\boldsymbol{g} \to \rho_0\boldsymbol{g}$, basically it is a reinterpretation of the rotation free part of the velocity as a microscopic current, responsible for pattern evolution and microscopic wave phenomena. In this way, we can keep the correct definition between the momentum ($\boldsymbol{p}$, a dynamic variable) and the divergence free velocity ($\boldsymbol{u}$, a kinetic variable) and more importantly, $\rho_0\boldsymbol{g}$ will not change sign, even where the density becomes negative.

With the previous definition, the continuity equation $\partial_t\rho + \nabla \cdot \boldsymbol{p} = 0$ becomes $\partial_t\rho = -\nabla \cdot (\rho\boldsymbol{u} + \rho_0\boldsymbol{g})$, which can also be expressed as

$$\partial_t\rho = -\left(\boldsymbol{u} \cdot \nabla\right)\rho - \rho_0\nabla \cdot \boldsymbol{g}\,,$$

where the term $(\boldsymbol{u} \cdot \nabla)\,\rho$ is responsible for the divergence free advection of the scalar function ρ and $\rho_0 \nabla \cdot \boldsymbol{g}$ drives pattern formation and elastic behavior on the microscale.

The convective form of the standard incompressible Navier-Stokes equation is used for the evolution of the total velocity field $\boldsymbol{v}$, with the rate of dissipation of energy controlled by the shear viscosity μ_{S}. The other necessary change we introduce is, that the convective form of the equation requires the divergence free velocity (instead of the total $\boldsymbol{v}$) in the term $(\boldsymbol{v} \cdot \nabla)\,\boldsymbol{v}$, responsible for the advection of the velocity field. We also add the possibility of fluctuations through the Langevin noise term ζ, with these changes the dynamic equation becomes

$$\partial_t \boldsymbol{v} = -\left(\boldsymbol{u} \cdot \nabla\right) \boldsymbol{v} + \mu_{\mathrm{S}} \nabla^2 \boldsymbol{v} - \nabla \left(\frac{\delta F}{\delta \rho} + \zeta \right) .$$

This model handles arbitrary pattern formation and propagating modes on the microscale, while accomplishes incompressible large scale transport of fluid and solid parcels.

Chapter 5

Precursor assisted nucleation

Crystallization is a *first order* phase transition, which in pure liquids happens via homogeneous nucleation. Fluctuations in the undercooled melt are responsible for the creation of crystal-like nanoscale clusters. Small clusters decay with a high probability, though there exists a critical size (called the nucleus), beyond which clusters grow with a high probability. This critical size depends on the solid-liquid interface free energy and the thermodynamic driving force. During heterogeneous nucleation, foreign particles or container walls promote nucleation as wetting surfaces. Nucleation plays a part in processes, that span a diverse selection of fields, such as geophysics, materials science, physical chemistry, biophysics and in many technological applications.

During the past decades, the knowledge gained on crystal nucleation and growth by conducting experiments and molecular simulations grew spectacularly: trajectories of colloidal particles in suspensions can be tracked by scanning confocal microscopy, providing structural/dynamical information, comparable in quality to the particle scale information from molecular dynamics or Brownian dynamics simulations.

It has also been established, that two-step nucleation via dense liquid/amorphous/metastable crystalline precursors is rather the rule, than the exception, a finding in accord with a range of experiments. These findings also indicate the limitations of classical nucleation theory, which does not contain the crystal structure explicitly. Optical experiments on hard-sphere-like colloidal suspensions indicate, that the crystal structure plays an important role in heterogeneous crystal nucleation. To account for such effects, one needs a single model, which naturally contains both the amorphous and crystal structures, crystalline anisotropies and elasticity.

5.1 Classical nucleation theory

The development of a nucleation theory dates back to the works of Gibbs, who has studied phase stability. He has also realized, that there is a free energy penalty associated with the creation of the interface between the two phases, called the surface tension and it works against the driving force.

The first true nucleation theory, that managed to address transition rates was put forward by Volmer and Weber [47] for condensation, then the classical nucleation theory (CNT) by Farkas [48] (on the basis of an idea of L. Szilárd) and in final form by Becker and Döring [49]. The CNT was adopted to transitions in condensed matter by Turnbull and Fisher [50].

The long history of the research on crystal nucleation is reviewed in [51–56]. Different kinds of computational methods have been applied to its study. The discrete atomistic ones include molecular dynamics (MD) [57–62], Monte Carlo (MC) [63–65] and Brownian dynamics (BD) methods. Continuum models based on the square gradient (SG) approximation include the van der Waals/Cahn-Hilliard/Ginzburg-Landau type models [28, 66–68] and the more complex phase-field methods [69–72]. While the most rigorous continuum model is based on correlation functions, which is the classical density functional method [73–77].

5.1.1 Homogeneous nucleation

It is an experimental observation, that a quiescent, pure liquid can be cooled below its melting point significantly. According to the CNT the formation of the nucleus, a heterophase fluctuation of the critical size is needed to initiate crystallization. The size of the nucleus depends inversely on undercooling $R^* \propto (T_m - T)^{-1}$ and diverges at the melting point. As the undercooling is increased the nucleus becomes smaller and the chance of a nucleation event greater.

According to the classical picture, the heterophase fluctuations possess a spherical shape and they are bounded by a sharp solid-liquid interface, this is called the capillary approximation or the droplet model. It is also assumed, that these fluctuations are able to grow or decay via single-molecule attachment or detachment. The thermodynamically derived work of formation for these clusters is $W_{\mathrm{hom}} = 4\pi R^3 \Delta\omega/3 + 4\pi R^2 \gamma$. R denotes the radius of the droplet, $\Delta\omega$ is the thermodynamic driving force, i.e. the grand potential difference between the solid and liquid phases, which is negative for undercooling and γ is the solid-liquid interfacial free energy. For small R the positive interfacial term dominates, while for larger R the negative bulk term overcomes the surface term, thus the work of formation

has a maximum at $R^* = -2\gamma/\Delta\omega$, where the barrier height is $W^*_{\text{hom}} = \frac{16\pi}{3}\frac{\gamma^3}{\Delta\omega^2}$. The cluster of this size is called the nucleus or critical cluster.

This static picture is augmented with nucleation kinetics, which in the classical picture relates the attachment/detachment rate of single molecules to the rate of formation of critical clusters, i.e. to nucleation rate. A master equation has been formulated to model the time evolution of the size distribution of n-molecule clusters N_n according to

$$\dot{N}_n = a^+_{n-1}N_{n-1} + a^-_{n+1}N_{n+1} - \left(a^+_n + a^-_n\right)N_n$$

with the special case for $n = 1$ that characterizes the time evolution of the number of monomers, i.e. monomers are depleted by dimer formation and by attachment to larger clusters and created through their inverse processes according to

$$\dot{N}_1 = a^-_2 N_2 - a^+_1 N_1 + \sum_{n>1}\left(a^-_n N_n - a^+_{n-1}N_{n-1}\right)$$

with

$$a^+_n = O_n\Gamma\exp\left(-\left[W_{n+1} - W_n\right]/\left(2\mathrm{k_B}T\right)\right)$$

and

$$a^-_n = O_{n-1}\Gamma\exp\left(-\left[W_{n-1} - W_n\right]/\left(2\mathrm{k_B}T\right)\right),$$

that describe molecular attachment and detachment frequencies. The number of surface sites on a cluster, that monomers can attach to is given by $O_n = 4n^{2/3}$ and the timescale of this process is $\Gamma = 6D/\lambda^2$. The self-diffusion coefficient is D, which is often related to viscosity through the Stokes-Einstein formula and λ is the molecular jump distance. The cluster formation energy W_n directly influences the kinetics through the Boltzmann factors.

The above system of equations reach a steady state nucleation process after a transient time $\tau \approx K\lambda^2 k_\mathrm{B}T\left(n^*\right)^{2/3}/\left(Dv_m\Delta\omega\right)$, here K is a geometrical factor, v_m is the molecular volume and n^* denotes the number of molecules in the nucleus. The steady state nucleation rate is given by

$$J_{\text{SS}} = \left(\sum_{n=1}^{\infty}\left(a^+_n N^{\text{eq.}}_n\right)^{-1}\right)^{-1} \approx J_0\exp\left(-W^*_{\text{hom}}/\mathrm{k_B}T\right)$$

in terms of the equilibrium population $N^{\text{eq.}}_n = \rho_0\exp\left(-W_n/\mathrm{k_B}T\right)$ and $J_0 = \rho_0 O_{n^*}\Gamma Z$ is the pre-exponential factor of the nucleation rate, ρ_0 is the number density of the liquid and $Z = \left(\frac{d^2W}{dn^2}\Big|_{n^*}/\left(2\pi\mathrm{k_B}T\right)\right)^{1/2}$ is the Zeldovich factor, which

accounts for the decay of critical clusters.

5.1.2 Heterogeneous nucleation

In impure liquids, especially in non-laboratory environments, crystals usually nucleate on preferred sites, i.e. the appearance of the crystalline fluctuations can be aided by various heterogeneities, foreign particles dissolved in the liquid or even the walls containing the liquid. In this case, depending on conditions, the nucleation barrier can be significantly reduced $W_{\mathrm{het}} < W_{\mathrm{hom}}$, which leads to higher nucleation rates. Classical nuclation theory incorporates the effect of large heterogeneities on nucleation via the spherical cap model, which is a geometrical condition between the contact angle at the three phase boundary and the size of the truncated nucleus. The contact angle θ is related to the mutual interface free energies of all the phases, through the Young-Laplace equation $\gamma_{\mathrm{WL}} = \gamma_{\mathrm{WS}} + \gamma_{\mathrm{SL}} \cos\theta$, which describes a force balance at the contact point of the three phases. The modified work of formation becomes $W_{\mathrm{het}} = W_{\mathrm{hom}} f(\theta)$ where $f(\theta) = (2 + \cos\theta)(1 - \cos\theta)^2/4$ is the catalytic potency factor.

5.2 Two-step nucleation

In agreement with theory [80], molecular dynamics simulations [65] and colloid experiments [81–83], recent investigations relying on the PFC model have shown, that at large undercoolings, crystal nucleation is a two-step process, i.e. an amorphous precursor assists the formation of the crystalline phase [2, 17, 19].

In the PFC model, crystal nucleation takes place in two steps at high undercoolings: in the first step an amorphous precursor forms and helps the appearance of the crystalline BCC phase [17, 19, 23] in the second step. Apparently, this phenomenon is highly relevant not only for colloids [82–84], but for such simple systems as the Lennard-Jones (LJ) fluid [80] and the hard sphere system [65], raising the possibility, that the presence of an amorphous precursor might be a general feature of crystal nucleation in highly undercooled liquids.

We have investigated the structural aspects of this process within the framework of the PFC model. In doing this, we have relied on the bond order parameters q_l and $\overline{q}_l$ introduced by Steinhardt et al. [85] and Lechner and Dellago [78]. The bond order parameter q_l considers the first neighbor shell around the particles, whereas $\overline{q}_l$ takes into account the relative orientations of atoms in the first and second neighbor shells, they are defined in App. C.1.

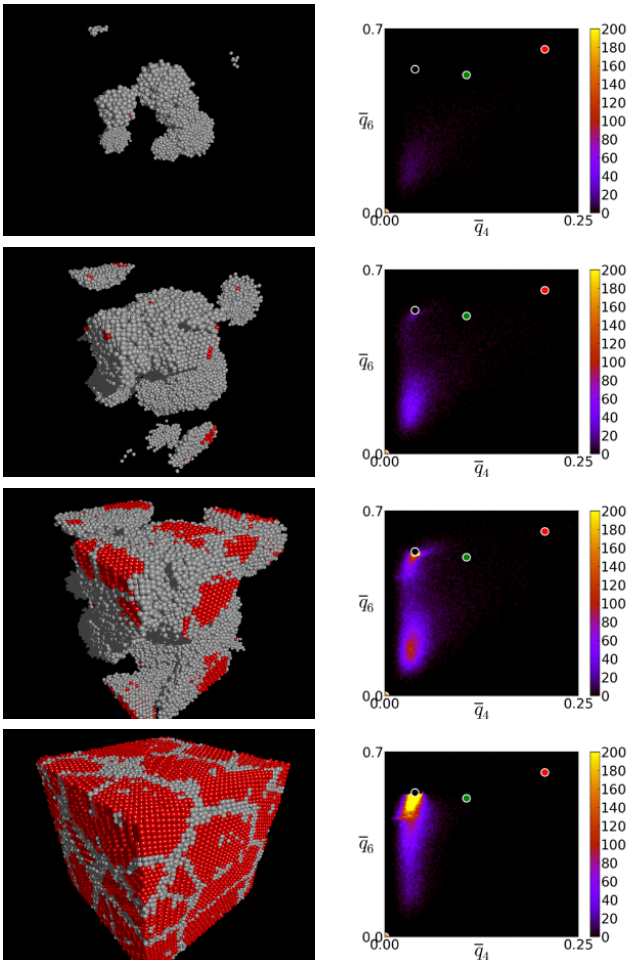

Figure 5.1: Snapshots of two-step nucleation in the PFC model at $\epsilon = 0.1684$ and $\overline{\psi} = -0.25$ at dimensionless times $t = 70$, 90, 110 and 1000, respectively. Left panel: red (bbc-like neighborhoods) - $q_4 \in [0.02, 0.07]$ and $q_6 \in [0.48, 0.52]$, white (amorphous) the remaining particles. Only the solid phase is visible. Right panel: q_4 vs. q_6 bond-order parameter map (as defined by Lechner and Dellago [78]). The circles on the right painted yellow, black, green and red indicate the positions of the ideal icosahedral, BCC, HCP and FCC structures, respectively.) Solidification appears to start with the nucleation of amorphous domains. Three-dimensional visualization of atomic structure was accomplished with OVITO, the Open Visualization Tool [79].

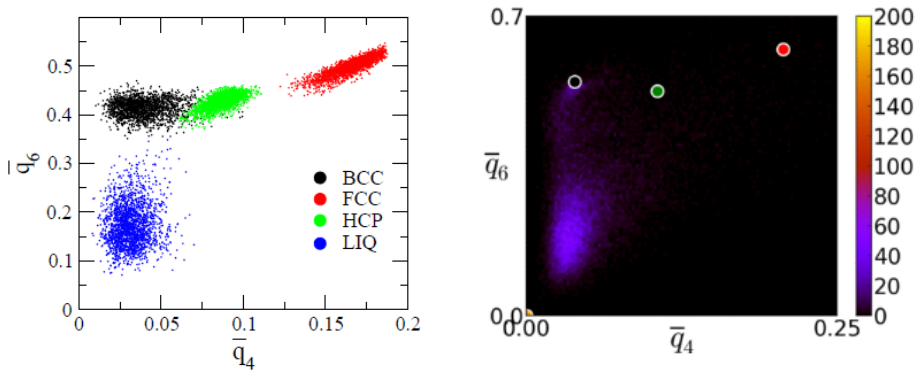

(a) (b)

Figure 5.2: Comparison of the $\overline{q}_6$ vs. $\overline{q}_4$ bond-order parameter maps obtained (a) for the Lennard-Jones system from molecular dynamics simulations (source: Ref. [78]) and (b) for the solidifying PFC system (the same as the second image from the top in Fig. 5.1). Apparently, the structure of the amorphous precursor observed in the PFC model is close to the structure of the bulk liquid in the Lennard-Jones system.

The phenomenon of two-step nucleation is illustrated in Fig. 5.1 for instantaneous quenching of the homogeneous liquid from above the liquidus line ($\epsilon = 0.1336$) to $\epsilon = 0.1667$. The scaled density of the initial liquid was $\overline{\psi} = 0.25$, while the noise strength was $A_{\text{noise}} = 0.42$. In the left column of Fig. 5.1, the particles, that have BCC-like neighborhoods are painted red, whereas the rest qualifies as amorphous (colored white).

Solidification starts with the formation of amorphous clusters and the BCC structure appears later. In the right column of Fig. 5.1, the respective $\overline{q}_6$ vs. $\overline{q}_4$ bond-order parameter maps are shown, together with the points corresponding to the ideal icosahedral, BCC, FCC and HCP neighborhoods. Indeed, the first appearing solid is the amorphous precursor, represented by the purple nebula, positioned slightly above and right of the lower left corner, whose amplitude (the amount of the amorphous neighborhoods) first increases with time, but soon disappears as BCC crystallization starts, with some remaining at the grain boundaries. Interestingly, the structure of the amorphous precursor is close to that of the liquid in the LJ system, as implied by the respective $\overline{q}_6$ vs. $\overline{q}_4$ maps (see Fig. 5.2).

Following the structural analysis employed in recent Brownian dynamics (BD) simulations [86] and colloid crystallization experiments [84], we performed a similar structural analysis for the amorphous (white) areas in Fig. 5.1. Analyzing BD simulations, Kawasaki and Tanaka arrived at the conclusion, that in the undercooled

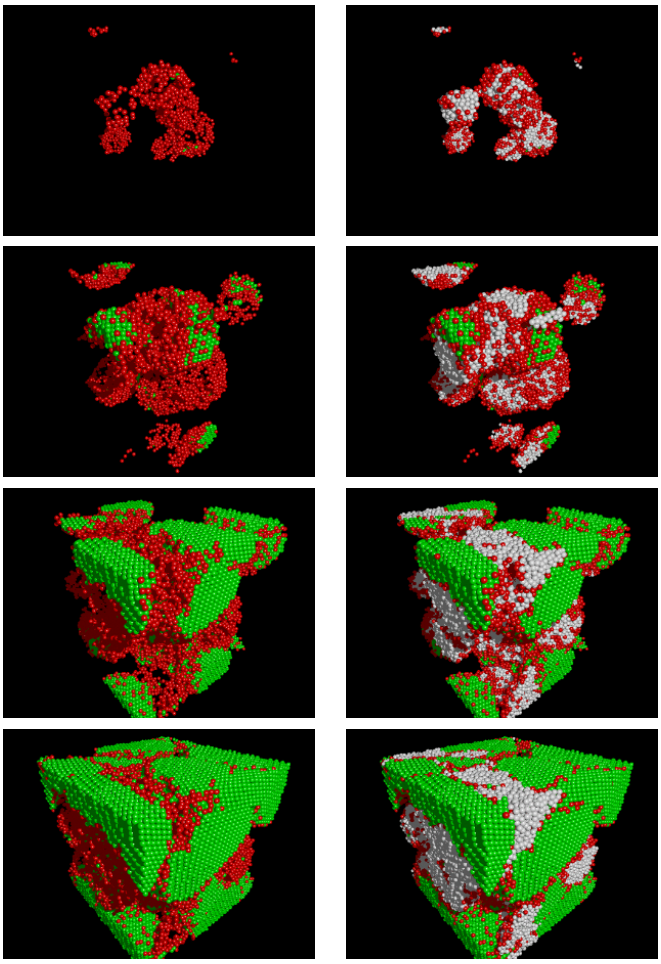

Figure 5.3: Structural analysis of two-step nucleation observed in the PFC simulation displayed in Fig. 5.1. The coloring scheme proposed by Tan et al. [84] has been used. (Here, the bottom row corresponds to dimensionless time $t = 130$, instead of $t = 1000$.) Left panel: only MRCO and BCC crystals are shown. Right panel: amorphous, MRCO and BCC domains are displayed. Coloring: green - BCC crystal - $\overline{q}_6 \geq 0.27$ and $\xi \geq 7$, where ξ is the number of solid bonds; red - MRCO - $\overline{q}_6 \geq 0.27$ and $\xi < 7$, white - amorphous - $\overline{q}_6 < 0.27$. Apparently, MRCO and the amorphous precursor appear roughly simultaneously (see Fig. 5.4), whereas the bulk BCC structure forms later in contact with the MRCO domains. It seems, that the MRCO domains evolve on the surface of amorphous domains, indicating a process akin to heterogeneous nucleation.

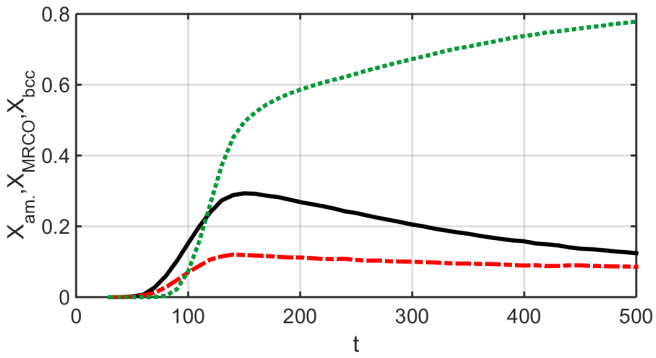

Figure 5.4: Time dependence of the fractions of particles having amorphous (black solid line), MRCO (red dashed-dotted line) and BCC (green dotted line) neighborhoods. Note the dominance of the amorphous structure at early times.

liquid the formation of a medium range crystalline order (MRCO) precedes crystal nucleation. They have categorized atomic neighborhoods according to their $\overline{q}_6$ bond order value: $\overline{q}_6 \leq 0.28$ qualifies as liquidlike, the range $0.28 < \overline{q}_6 < 0.4$ qualifies as MRCO, while $\overline{q}_6 \geq 0.4$ is BCC crystalline. Assigning white, red and green colors to the respective particles, they visualized the spatiotemporal evolution of the undercooled liquid [86].

We have adopted a similar, but slightly different procedure by Tan et al. [84] in analyzing the PFC simulations, where ξ has been introduced, see App. C.1 for its definition. It represents the number of solid bonds of an atom, calculated from the bond order correlation between neighbors. The coloring scheme by Tan et al. and also used in Fig. 5.3 is the following: white color represents amorphous neighborhoods with a low value of $\overline{q}_6 < 0.27$. MRCO ordering is colored red and it is indentified by a high value of $\overline{q}_6 \geq 0.27$ but a low number of $\xi < 7$ solid bonds, while the crystalline BCC order, colored green, belongs to a high value of $\overline{q}_6 \geq 0.27$ and a large number of solid bonds $\xi \geq 7$.

We show the respective MRCO and BCC regions in the left column of Fig. 5.3. The overall similarity between the BD and PFC simulations is fairly reasonable: in both cases, appearance of MRCO regions precedes the formation of the BCC crystals, which evolve inside/in connection with the MRCO domains. Remarkably, however, in the PFC simulations a disordered (amorphous) solid appears first (see Fig. 5.4), that is structurally similar to the liquid. Apparently, the white domains in the first row of Fig. 5.1, can be divided into two types of subdomains, one containing MRCO and the other, a solid state of liquidlike structure. We note, that the latter has not been reported in BD simulations. One may speculate, that in particle based simulations, the amorphous solid and the liquid regions might

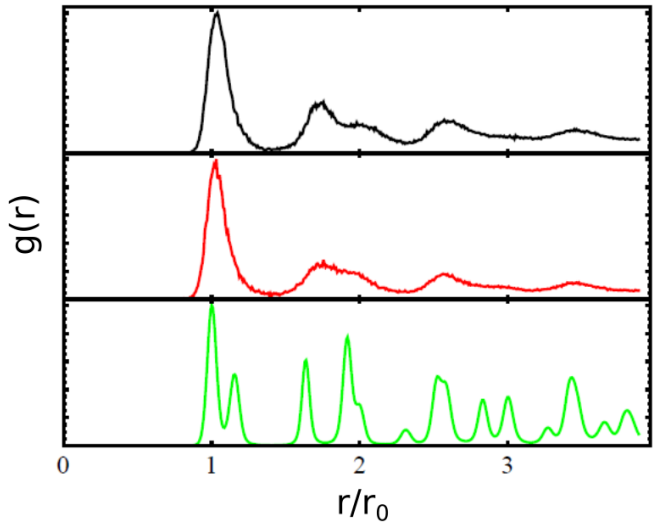

Figure 5.5: Radial distribution functions (RDFs), characterizing the amorphous (top), MRCO (middle) and BCC (bottom) structures. Note the closeness of the RDFs for the first two. The RDF for MRCO is in a good agreement with that of the BCC-like precursor observed in colloidal systems [84].

be distinguished via investigating time correlations in the local structure, which has yet to be performed for the BD simulations. The radial distribution functions for the BCC, MRCO and amorphous structures are displayed in Fig. 5.5. The RDFs predicted by the PFC model are close to those from molecular dynamics simulations for undercooled and crystalline iron [87, 88], whereas the RDFs of the amorphous and MRCO structures resemble closely the RDF of the BCC-like precursor observed in experiments on colloids [84].

We have studied the structural signatures of the amorphous precursor assisted crystal nucleation, that the PFC theory predicts at high undercoolings. An analysis in terms of bond order parameters implies, that the structure of the amorphous precursor is close to that of the LJ liquid, whereas the respective radial distribution function resembles closely those from MD simulations of undercooled iron.

5.3 Contributions

I have performed instantaneous quenches in the PFC model, to study precursor formation. Following the analysis of Tan et al., I have segmented the solid domains into amorphous, MRCO and BCC atomic neighborhoods. By analyzing the solid fractions of these species in time, I showed, that the first solid clusters are definitely amorphous and BCC ordering appears later, as a consequence. MRCO regions

are present mostly on the surfaces of the amorphous clusters and facilitate the appearance of the BCC crystal.

I have presented structural analysis of the non-crystalline precursor clusters in terms of the first neighbor averaged bond order parameters $\overline{q}_l$ by Lechner and Dellago, which places these clusters at the same region in the two-dimensional $\overline{q}_6$ vs. $\overline{q}_4$ histograms as the LJ liquid. I have shown good agreement between the RDFs of the amorphous regions from PFC simulations and those from MD simulations of undercooled liquid iron. The RDF of the BCC domains is virtually identical to those from MD simulations of crystalline BCC iron.

In summary, I conclude, that dynamical mean field theories, such as the PFC model are not limited by the assumptions of CNT and predict the non-direct appearance of the thermodynamically most stable solid phase at large undercoolings, through an amorphous solid structure.

Chapter 6

Hydrodynamic EOMs

6.1 Crystallization kinetics

The PFC model succeeded in addressing the microscopic aspects of crystallization [1, 2, 89] within the framework of continuum theories. Most PFC studies assume overdamped particle dynamics, which approximates crystalline aggregation in suspensions of *colloidal* particles reasonably well. In Ref. [15] a hydrodynamic theory of freezing (HPFC) was proposed, that applies to solidification in *molecular liquids*. The HPFC approach builds on the dynamical equation of fluctuating nonlinear hydrodynamics [41] and employs the free energy functional of the PFC model, as the reversible stress tensor. A detailed review is available in Sec. 4.4.2.

The correct dispersion relation for long wavelength acoustic phonons is reproduced by the HPFC model, and it also supports a steady state front velocity v_{sol}, which is inversely proportional $v_{\mathrm{sol}} \propto 1/\mu_{\mathrm{S}}$ to the shear viscosity μ_{S} [45]. This is quite different from the behavior observed with diffusive dynamics, in which a depletion zone forms ahead of the solid-liquid interface, due to the fact, that the crystal has a larger density, than the liquid. Matter needs to be transported to the solidification front via diffusion and the front position evolves according to $\propto \sqrt{t}$ as documented in Ref. [90], caused by a widening depletion zone. Although, other PFC-based hydrodynamic models [91–93] have become available, it is only the HPFC model, in which steady growth and the proper capillary wave spectrum has been demonstrated.

The HPFC model also describes elastic stress relaxation reasonably well. The thermodynamic force, as determined by the PFC functional, is the *reactive* force in the model, which is contrasted to the diffusive case where the same functional serves as the *dissipative* force. The HPFC model is expected to capture defect

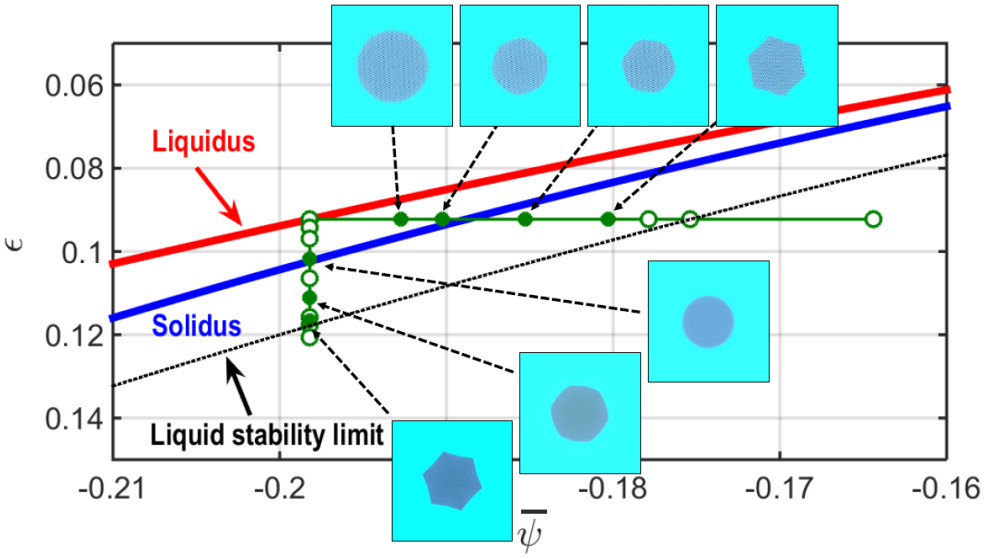

Figure 6.1: Phase diagram in the $\epsilon - \overline{\psi}$ plane with corresponding growth forms produced by the HPFC model without noise. The liquidus and solidous curves, together with the liquid stability limit are plotted. Filled green dots denote the location in the phase diagram of the corresponding growth forms.

formation and therefore produce polycrystalline growth forms on the nanoscale.

Structural aspects of crystal nucleation and growth in undercooled liquids are explored, however, due to the computational cost, only two-dimensional problems are considered. We first employ the HPFC model to show, that in this hydrodynamic approach, homogeneous and heterogeneous nucleation processes are accessible. Beyond that, the existence of growth front nucleation in highly undercooled liquids is documented, which is the formation of grains with new orientation at the solidification front.

6.1.1 Growth forms

We have started our investigations in the HPFC model by initiating growth with an atom-size external potential well, at several points in the phase diagram, graphically illustrated in Fig. 6.1. The driving force increases with an increasing distance from the liquidus line, denoted by the thick red line in the figure. Thus, either increasing the initial density (horizontal line) or increasing the reduced temperature (vertical line) can be used to increase driving force. A clear trend is visible in terms of interface properties. The vicinity of the liquidus line leads to rounded, circular crystals, see Fig. 6.2(a). With increased driving force, the underlying hexagonal symmetry of the crystal becomes visible in the growth form, edges of the closed

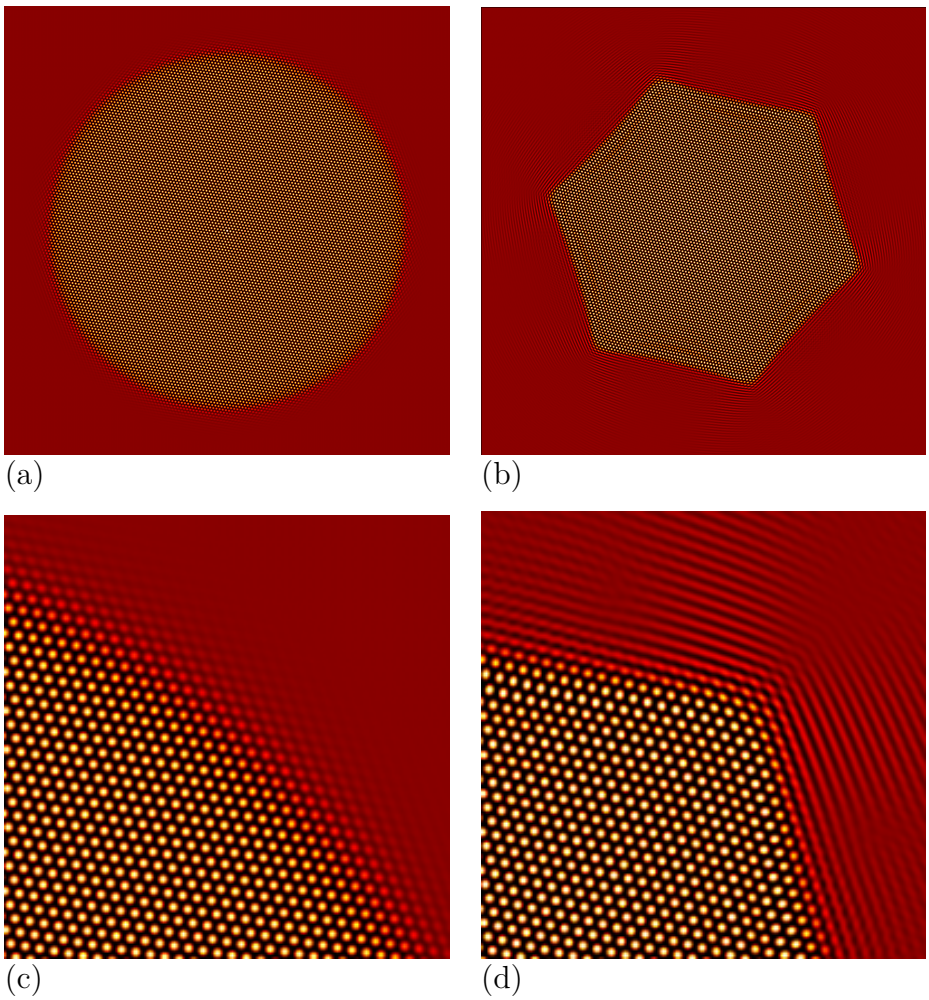

Figure 6.2: Density map of the solid-liquid interface near the liquidus line (a,c) and close to the liquid stability limit (b,d). Close-up views of the interface are shown in the second row.

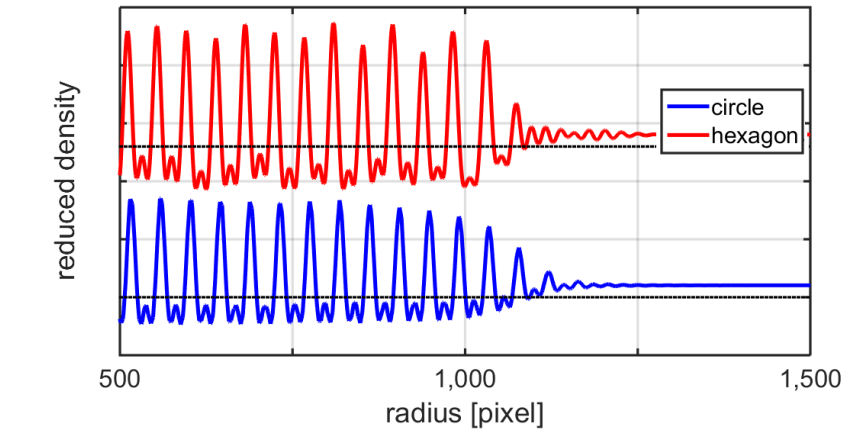

(a)

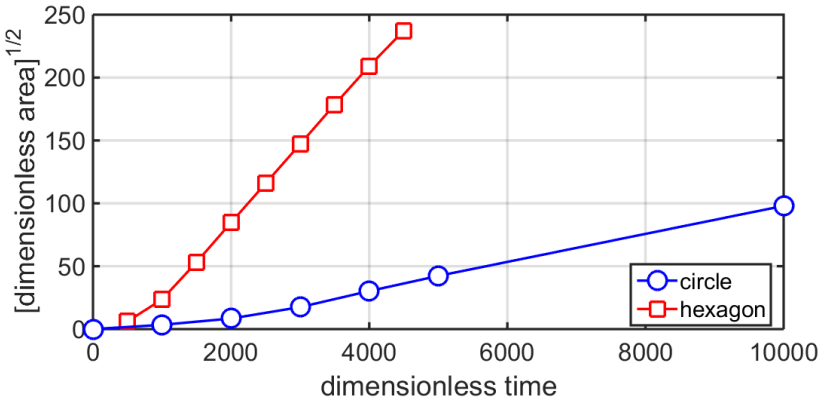

(b)

Figure 6.3: Density profile along a line of atoms across the interface in figure (a). Grain radius in time in figure (b). Blue lines belong to the rounded crystal (a) and red lines to the hexagonal crystal (b) in Fig. 6.2.

packed crystalline orientation appear with rounded corners. At still larger values of the driving force the bounding edges turn to concave faces, see Fig. 6.2(b), the corners show the fastest growth wrt. orientation. With increasing driving force the SL interface becomes more faceted and reduces in width, except near corners, where long-range density modulations in the liquid develop. Close-ups of the interfaces are visible in the second row of Fig. 6.2. The interface structure is analyzed further in Fig. 6.3(a). The time evolution of the crystal radius is displayed in Fig. 6.3(b), calculated from the enveloped area. The larger driving force (red line) corresponds to faster growth and the radius clearly increases linearly in time, as expected from the hydrodynamic density transport, see Sec. 4.4.2.

6.1.2 Solid fraction

The presence of thermal momentum fluctuations in the HPFC model gives rise to density fluctuations, which ultimately lead to homogeneous nucleation in the metastable liquid regime. We have investigated the time development of the crystalline solid fraction during polycrystalline solidification, at model parameters $\epsilon = 0.1158$ and $\overline{\psi} = -0.1982$. The simulation from Fig. 6.4 is evaluated in Fig. 6.5.

Polycrystalline growth is frequently analyzed in the literature by way of the Johnson-Mehl-Avrami-Kolmogorov [94] model, in terms of the time dependence of the solid fraction. The JMAK expression

$$X\left(t\right) = X_{\max}\left(1 - \exp\left[-\left(\frac{t - t_0}{\tau}\right)^p\right]\right)$$

predicts the solid fraction (X) to satisfy a saturating exponential curve, where t_0 is the incubation time, i.e. the time it takes for the first nucleus to appear in the sample, τ is a characteristic time, related to the nucleation and growth rates and p is the Avrami-Kolmogorov exponent. It is the result of an analytical model, which considers the time dependence of the nucleation rate and the growth rate. Several assumptions need to be made for its derivation: nucleation occurs homogeneously in the liquid part of the material, growth rate is isotropic and independent from the transformed fraction. The exponent changes, as the conditions of nucleation and growth change. For example, large nucleation rate and small growth rate produces small crystals in the final microstructure, while small nucleation rate and large growth rate leads to large final crystals. Homogeneous nucleation and steady growth predicts the exponent to be $p = 1+D$, where D is the dimensionality of space.

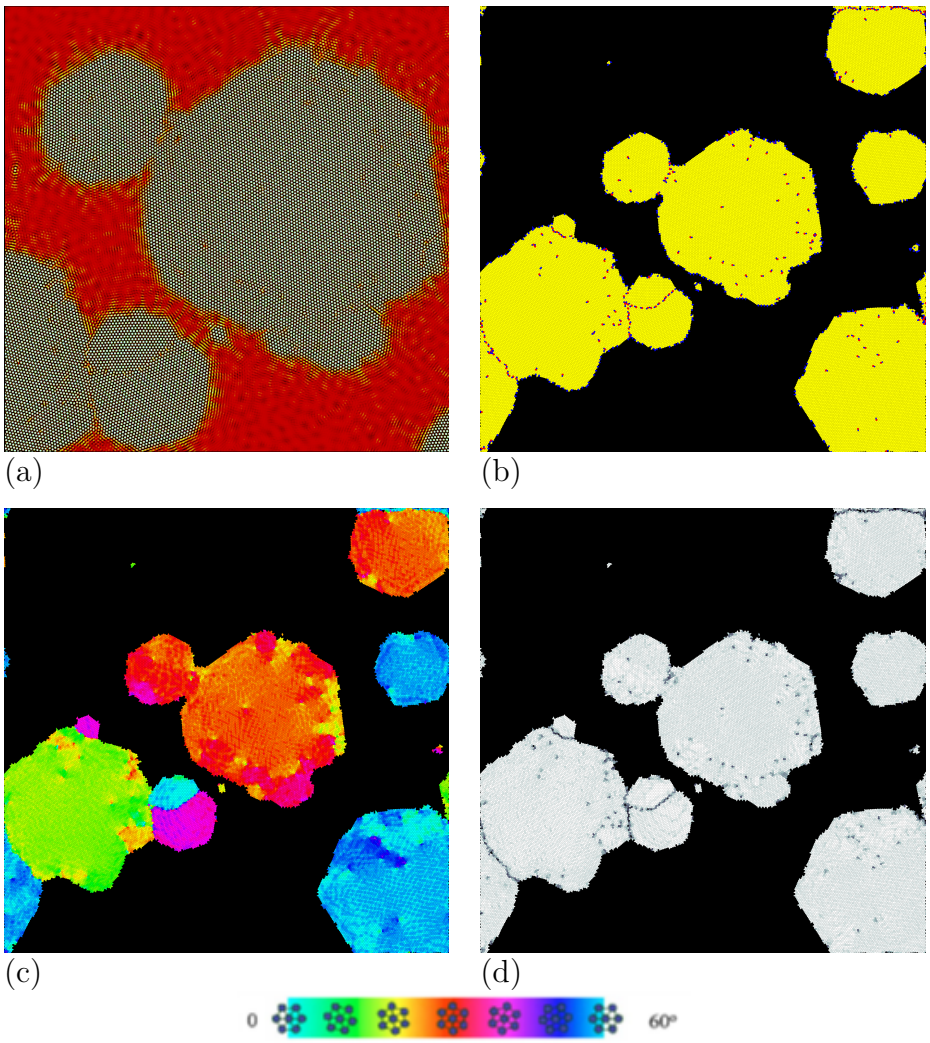

Figure 6.4: Voronoi analysis (see App. C.2) of a snapshot of a HPFC simulation at large undercooling ($\epsilon = 0.1158$ and $\overline{\psi} = -0.1982$). The presence of momentum noise in the undercooled liquid produces homogeneous nucleation and polycrystals, that later impinge on one another. The middle portion of the density map is pictured in Fig. (a), the Voronoi cells, colored according to the number of neighbors is in Fig. (b), the argument of the complex hexatic OP can be seen in Fig. (c) and the absolute value of the hexatic OP is visible in Fig. (d). The orientational color scheme is illustrated in the bottom.

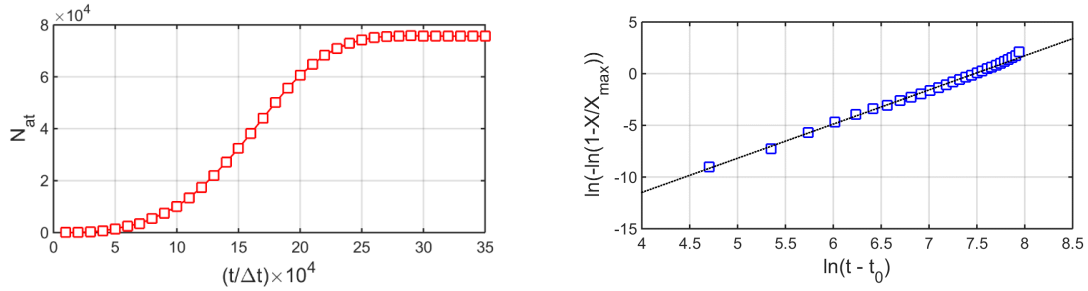

(a) (b)

Figure 6.5: Quantification of polycrystalline growth kinetics from the simulation displayed in Fig. 6.4. Figure (a) shows the number of atoms in the simulation domain in time. Figure (b) shows the Avrami plot, which gives a close to linear relationship with the fitted exponent of $p = 3.31$.

In Fig. 6.5(b) the data are transformed according to the expression

$$\log\log\frac{X_{\max}}{X_{\max} - X\left(t\right)} = p\log\left(t - t_0\right) - p\log\tau\,,$$

so that a linear fit would give the desired exponent, which turned out to be $p = 3.31$. This value, together with the fact that crystal growth is linear in time in the HPFC model, indicates, that the deviation of the measured $p = 3.31$ from the expected value of $p = 1 + D = 3$ is the result of an increasing nucleation rate in time.

6.1.3 Athermal nucleation

The free growth limited model [95, 96] of athermal nucleation describes a practically important mechanism, that helps in the understanding of the effect of undercooling in melts with foreign particle additives. Athermal nucleation is a deterministic, non-thermally activated barrier to free growth. The model predicts, that the size of the foreign particles is the crucial parameter in determining the condition of free growth for a set undercooling. Wetting of the substrate by the crystal induces the formation of some crystalline fraction on the surfaces of the foreign particles at any undercooling. However, a critical undercooling is predicted, which is a function of particle size, above which free growth of the crystalline phase takes place.

We have created a HPFC simulation with a square lattice substrate intended to mimick a foreign particle, modeled via an external potential as described in Sec. 7.2.1. Different reduced temperatures were selected for the simulation, to

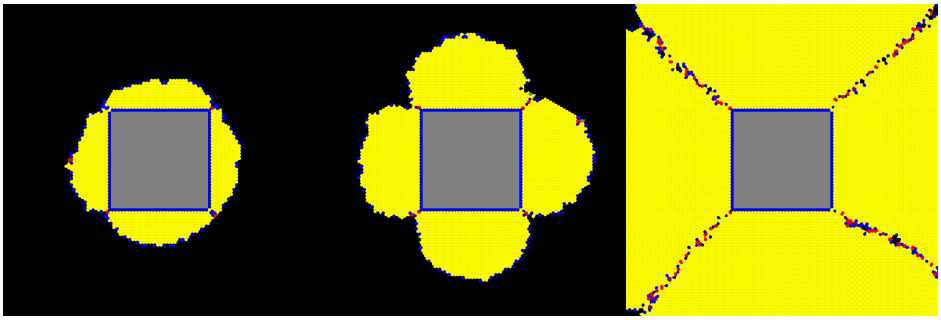

Figure 6.6: Voronoi maps of particle induced crystallization: the yellow areas indicate the perfect triangular crystalline fraction, formed on a square lattice substrate. Corners of the foreign particle induce grain boundary like lattice irregularities, due to the mismatch of the triangular and square lattices. The average density is set to $\overline{\psi} = -0.1982$, while the reduced temperature is increased from left to right: $\epsilon = 0.0932, 0.0941$ and 0.0970. Left figure shows a stable, subcritical situation, the middle figure is close to critical, while the right one shows free growth. There is an increase in the curvature of the solid-liquid interface due to an increase in undercooling. The curvature is maximum, when the solid-liquid interface is a hemisphere. Beyond that point, the onset of free growth achieves athermal nucleation.

account for an increase in undercooling. The results are summarized in Fig. 6.6, which shows, that the HPFC model indeed reproduces a critical undercooling (for fixed size of the foreign particle) beyond which, free growth sets in.

6.2 Polycrystalline growth forms

The formation of crystalline grains in the undercooled liquid via thermal fluctuations, i.e. crystal nucleation, is essential [51] to the formation of polycrystalline and nanostructured materials. The interaction of nucleation and the growth front plays the determining role in the structure of polycrystalline growth forms, such as disordered dendrites [97, 98] and spherulites [99]. The mechanism behind the creation of these complex polycrystalline growth forms, has been identified as growth front nucleation (GFN) [100–103]. It describes the formation of grains of new orientation at the propagating solid-liquid interface, the growth front.

These complex growth forms have been reproduced with conventional coarse-grained phase-field modeling of microstructure evolution, via the incorporation of an orientation field, which carries information on the local microscopic crystallographic orientation of the solid phase. However, to produce GFN, the definition of the orientation field had to be extended also to the liquid phase. In the liquid domain, the orientation field follows a uniformly distributed random variable on

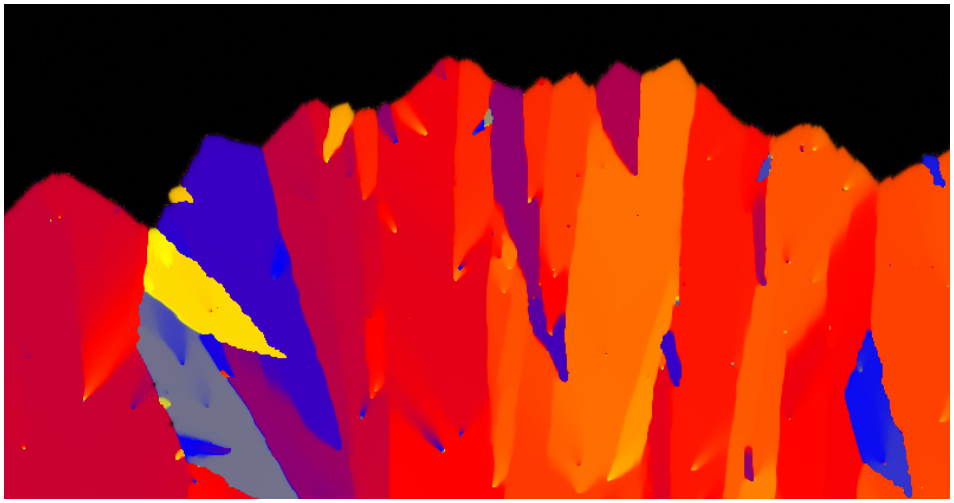

Figure 6.7: Orientation map from a phase-field simulation of spherulitic solidification [86, 87].

the interval $\Theta \in [0, \Theta_{\max})$ where $\Theta_{\max}$ is determined by crystal symmetry, the average of such a cyclic random variable bears no physical significance.

In phase-field modeling (PF), the formation of new grains at the front happens either by branching in the direction of low grain-boundary energies (at small undercoolings) [102, 103] or by quenching in orientational defects into the crystal (at large undercoolings) [101, 103]. Additionally, the effect of impurities, which act as pinning centers for the orientation, can be modeled by fixing the value of the orientation field at certain locations. A snapshot illustrating the polycrystalline growth of an initially single crystal in a PF simulation can be seen in Fig. 6.7. The formation of orientational defects at the solid-liquid interface is shown, that initiate grains with orientations distinct from the initial crystal's. Color corresponds to a continuum of crystallographic orientations. Sharp changes in color stand for grain boundaries (arrays of dislocations). Point-like orientation defects can be interpreted as pinning centers (impurities with fixed orientation). The liquid domain, where the value of the phase-field is close to zero is colored black.

While this approach, relying on a coarse-grained orientation field proved to be quite successful in capturing rather complex solidification microstructures [101–104], the microscopic kinetics of the GFN phenomenon remained largely hidden in such coarse-grained models. While it is possible to gain insight into nucleation and liquid ordering through molecular dynamics simulations, the study of GFN seems to be out of reach of MD simulations.

It is desirable to clarify our understanding of GFN in atomistic continuum studies, in which the order parameter naturally carries the symmetries intrinsic

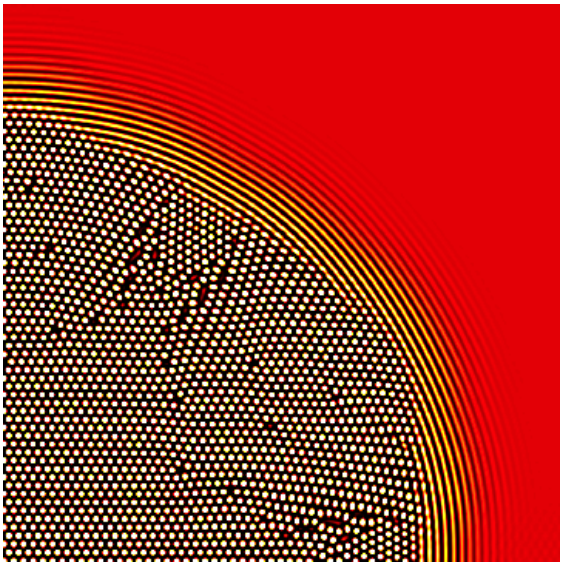

Figure 6.8: Single crystal growth in the diffusive PFC model, without fluctuations, at model parameters $\overline{\psi} = -0.45 > -0.5 \left(= \overline{\psi}_c\right)$, $\epsilon = 0.75$. This set of parameters corresponds to a part of the phase diagram, where the liquid is linearly unstable to fluctuations. The solid-liquid interface is very broad and displays a one-dimensional density modulation (similar to the lamellar phase), dislocations in the triangular lattice and grains with orientations different from the initial one can be identified. Initial crystal seed is located in the bottom left corner.

to a given crystal structure and no objectionable extension of a coarse-grained orientation field to the liquid domain is necessary. We have set out to explore the microscopic origins of polycrystalline growth by the formation of new grains at the solid-liquid interface at high supersaturations, within the framework of the PFC and HPFC models.

6.2.1 Investigations in the DPFC model

Previously, Gránásy et al. have attempted the modeling of GFN within the DPFC model (unpublished work). They have observed, that an initial single crystal seed developed into a polycrystalline structure, pictured in Fig. 6.8. The EOM was solved without thermal fluctuations, model parameters were set such, that the liquid was beyond its linear stability limit and growth was initiated by a crystal seed of the triangular lattice. Eventually, the crystal seed developed into a polycrystalline structure.

At these high supersaturations, density waves develop around the crystal, the two-dimensional atomic density modulation turns into a one dimensional modula-

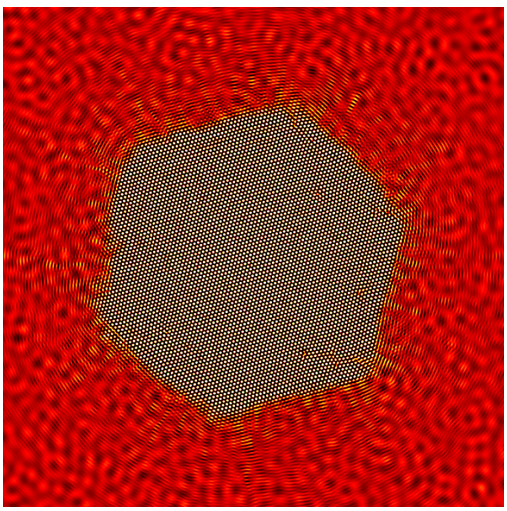

(a) Defects freeze in causing polycrystalline growth

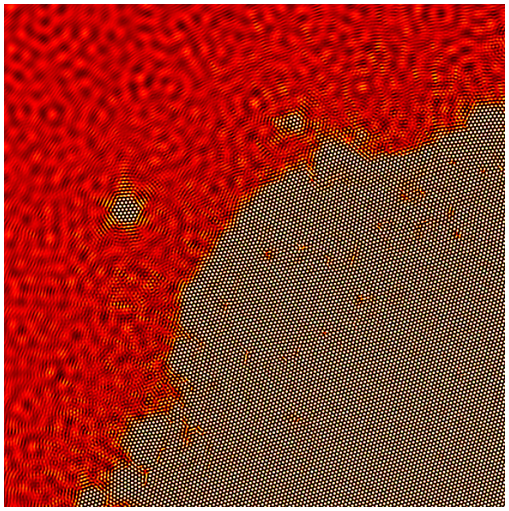

(b) Satellite crystals form near the growth front

Figure 6.9: Polycrystalline growth initiated from a single crystal seed, as evolves in the HPFC model in the metastable liquid regime. The HPFC model takes into account thermal fluctuations via momentum noise. Simulation parameters are $\epsilon = 0.0923$, $\overline{\psi} = \overline{\psi}_c - 0.11\Delta$ ($\Delta = \overline{\psi}_c - \overline{\psi}_{\mathrm{L}} = 0.0028$, liquidus $\overline{\psi}_{\mathrm{L}} = -0.1982$, stability limit $\overline{\psi}_c = -0.1754$). The number density map is shown, which displays atomic maxima, along with fluctuations of the density field in the liquid domain.

tion at the solid-liquid interface, characteristic to the lamellar phase. It is followed by the atomic density modulation in the bulk of the grain. In some directions, determined by symmetry and the compatibility of the triangular lattice with the concentric density modulation, a large number of defects appear.

While this incompatiblity mechanism might be viewed as a form of GFN, since the liquid is *unstable* to density fluctuations in this regime, it cannot bear much physical significance. The addition of thermal fluctuations to the simulation results in the nucleation of polycrystalline grains in the whole of the liquid domain. They have observed no sign of the formation of orientational defects during growth happening in the metastable part of the phase diagram.

6.2.2 Investigations in the HPFC model

Tóth et al. in Ref. [15] have developed a hydrodynamic EOM (termed HPFC here), built around the free energy functional of the PFC model and developed a dynamical coarse-graining procedure, as described in Sec. 4.4.2 to provide density transport beyond the overdamped limit of the usual diffusive EOM. We have em-

ployed this model, in the hope, that it captures a certain way of density-amplitude interaction, that would facilitate the GFN mechanisms.

This attempt proved to be fruitful at large undercoolings, simulations, that were started from an initial single crystal seed, did develop a polycrystalline microstructure at later times. Displayed in Fig. 6.9, a simulation of the HPFC model was initiated from a central seed of the triangular lattice. Initially, growth proceeds in an orderly fashion, however, at later times grain boundaries develop. This indicates, that crystalline orientations different from the one in the seed have developed, a polycrystalline domain has formed.

In Fig. 6.9, at the cited model parameters the liquid is in the *metastable* regime, i.e. stable against small fluctuations, which are incorporated via momentum noise. Copious nucleation is not hindering the results, in contrast to the diffusive PFC simulations with fluctuations.

To make the defect structure obvious, the results are analyzed with the help of Voronoi tessellation, see App. C.2, to create non-overlapping polygons, that tile the plane. In Fig. 6.10 at early times (a,c) clearly a single crystal grows without defects, 6 sided polygons colored yellow tessellate the bulk of the crystal. As time goes by (b,d), dislocations accumulate by the incorporation of inhomogeneities at and beyond the growth front, these show up later as grain boundaries. Low angle ones feature dislocations placed far apart, while high angle grain boundaries consist of dislocations placed more closely together. A dislocation shows up as a strongly bound blue-red pair of a 5 and 7 sided polygon.

Another way to quickly grasp the polycrystalline nature of the crystal grain, is to look at the hexatic order parameter map, described in App. C.3. The hexatic order parameter is sensitive to the natural ground state of the model, the triangular lattice. The polygons in Fig. 6.10(c,d), resulting from the Voronoi tessellation are colored according to the argument Θ of the complex hexatic order parameter. Grain boundaries are now clearly visible as jumps in Θ, the local orientation of the lattice.

6.2.3 GFN mechanisms

Analyzing the simulations, led us to recognize two scenarios, according to which new orientations appear at the growth front. The first one is (i), when dislocations enter the ordered crystalline lattice, initially at the corners and at the centers of the bounding faces of the grain, later at the cusps of the solid-liquid interface. These defects resemble misfit dislocations, resulting from the interaction of the

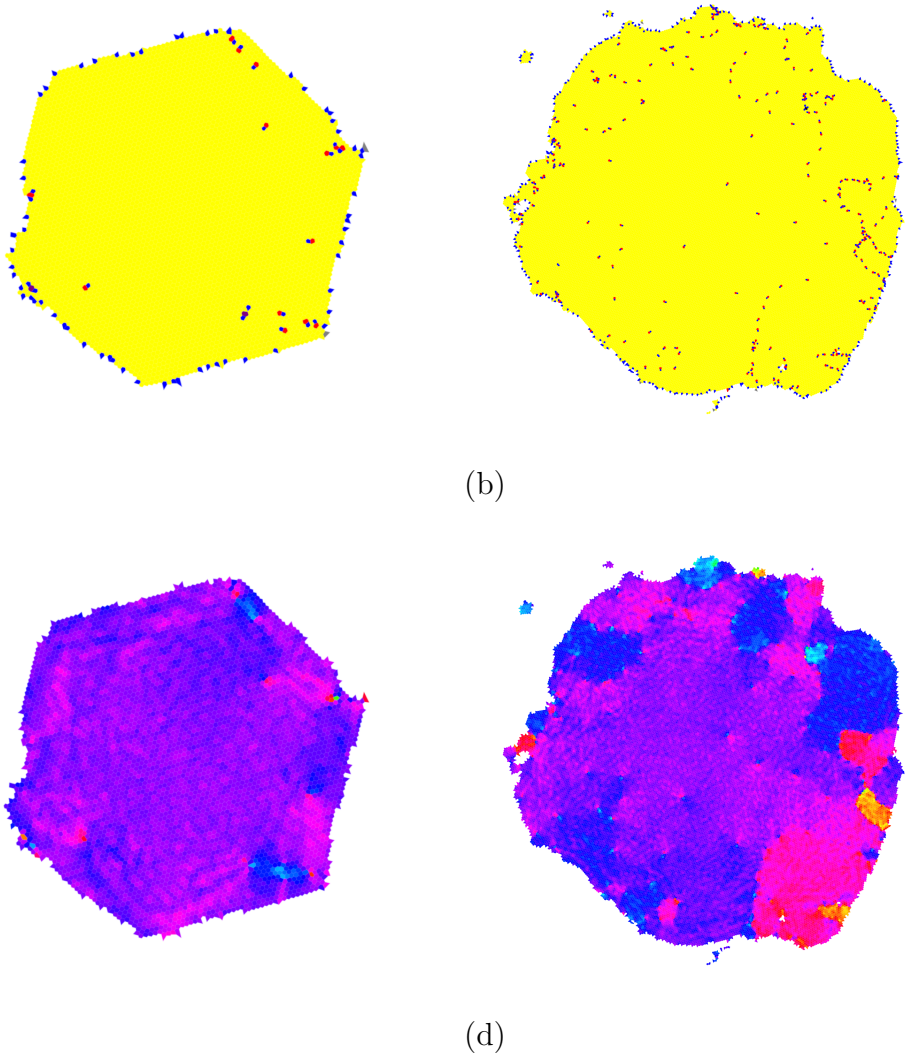

(a) (b)

(c) (d)

Figure 6.10: Upper row: analysis of GFN with the Voronoi method, 6 sided polygons, the natural ordering in two dimensions in the PFC model, are colored yellow, while polygons with 5 sides are colored blue and polygons with 7 sides are colored red. Lower row: analysis of GFN with the help of $\Theta = \arg(\hat{g}_6)$, the argument of the complex hexatic order parameter, a cyclic color scheme based on color hue is used to represent the orientation, which returns to its starting color after a maximum of 60°. Right column shows the same crystal as the left column, but at a later time, images are scaled to fit.

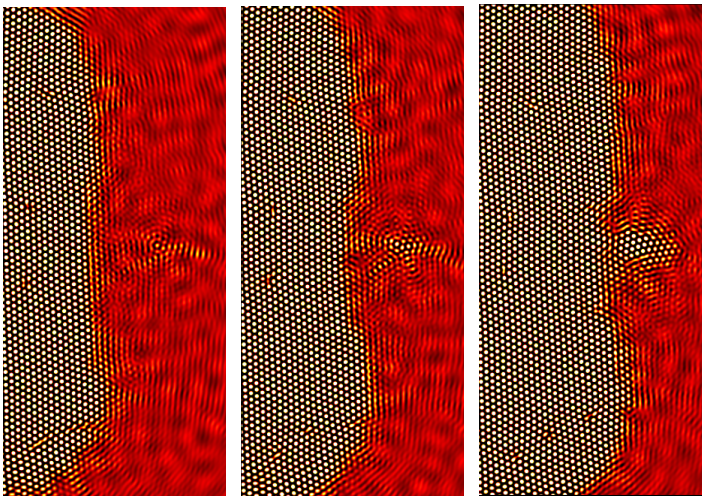

Figure 6.11: Crystal nucleation near the solidification front, interfering with density modulations of the interface and with those due to thermal fluctuations.

stress field and the fluctuations in the solidification front.

The other mechanism is (ii) the nucleation of small grains in the liquid domain, near the rough solid-liquid interface, which apparently are the result of the interference of the density waves emanating from the solid-liquid interface and the thermal fluctuations present in the liquid domain. This scenario is pictured in Fig. 6.11. The first mode (i) of GFN generally results in less deviation from the orientation of the bulk crystal, than the second mode (ii) of GFN, which essentially produces independently oriented grains.

We have observed, that mechanism (i) is active over a broad range of undercoolings. The rate, at which dislocations form increases with increasing undercooling, which suggests, that the increase in front velocity is connected to the creation of these defects. Though the second mechanism (ii) is only expressed near the liquid stability limit. For a fixed reduced temperature of $\epsilon = 0.0923$, mechanism (ii) is only active in the density range $-0.1778 < \overline{\psi} < \overline{\psi}_c = -0.1754$.

6.2.4 Stressed growth

Further deliberation is needed to understand the reasons behind mechanism (i) of defect formation. The fact, that mismatched layers grow and the interface captures imperfections of the lattice, hints at the importance of elastic effects. Similar behavior can be observed during strained epitaxial growth. The Asaro-Tiller-Grinfeld mechanism (see Refs. [105, 106]) predicts an instability towards interfacial modulations in coherently grown, strained layers. The ATG scenario assumes an initially

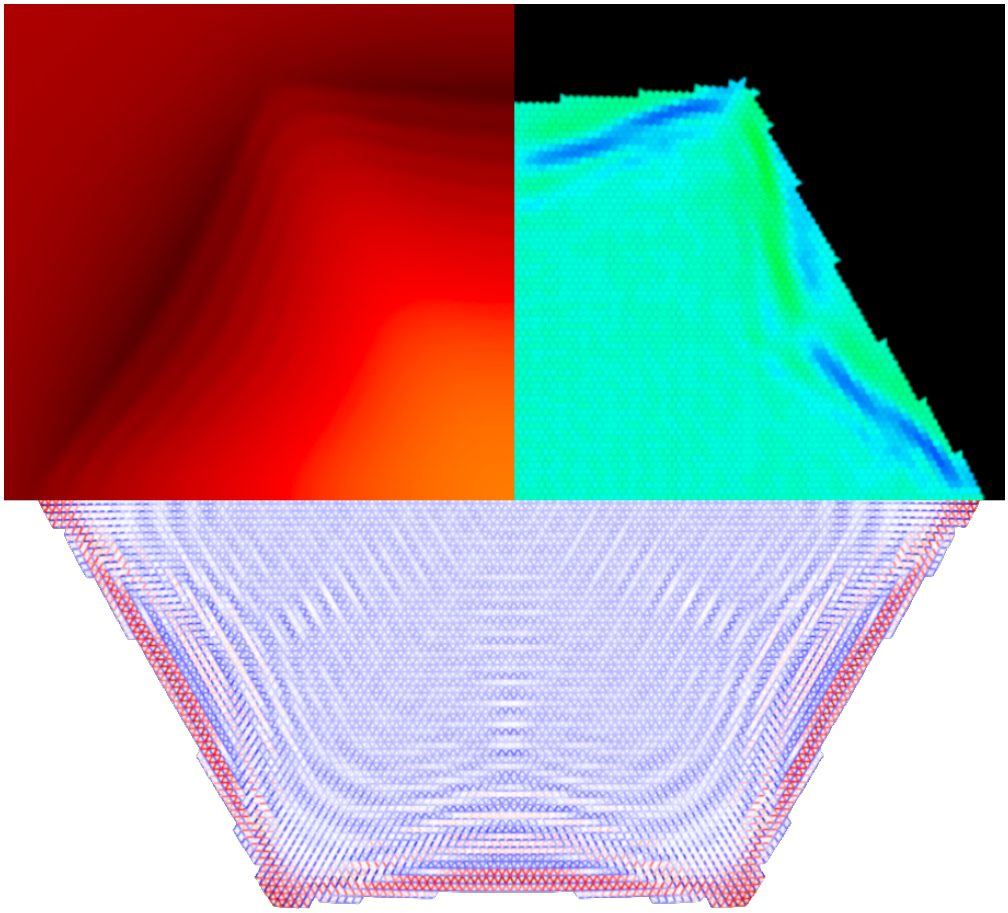

Figure 6.12: Single crystal grown in two dimensions at model parameters $\epsilon = 0.1158$ and $\overline{\psi} = -0.1982$ without thermal fluctuations. Upper left side shows the coarse grained density map, obtained by low-pass filtering $\psi(\boldsymbol{r})$ in Fourier space. Upper right side shows the local lattice orientation, calculated from the hexatic order parameter. In the lower row, bonds between first neighbors of atoms are colored according to the difference of their lengths from the ideal lattice constant. Red bonds indicate larger separation, while blue bonds indicate smaller atomic separation, white is neutral.

planar interface and an isotropic surface free energy, which is a good starting point for epitaxial studies. Fig. 7.14 from the next chapter shows the evolution of interface morphology of a strained crystal.

In the case of our investigation of GFN, a single compact crystal grows at early times. For low undercoolings the growth form is isotropic (see (a,c) in Fig. 6.2) and no irregularities appear in the lattice structure, even at late times. The situation changes drastically for greater undercoolings, when GFN is observed: the growth forms become somewhat faceted and highly anisotropic (see (b) in Fig. 6.2), modulations appear in the atomic positions close to the interface (see (d) in Fig. 6.2).

We have methods at our disposal to analyze irregularities in the perfect atomic structure, even before defects accumulate. In the upper row of Fig. 6.12 on the right side, the local lattice orientation is displayed for an anisotropic growing crystal. While the lattice orientation appears homogeneous in the bulk of the crystal, approaching the edge of the hexagon comes with a slight rotation of the lattice towards the center of the edge. The oscillation in the local orientation correlates with steps in the coarse-grained density, shown on the left side, in the upper row. The minimum of the coarse-grained density is located in front of the middle of the edge of the hexagon. Despite hydrodynamic density transport, this density distribution is mimicking a depletion zone, characteristic to diffusion controlled growth. Growth rate is slower in the middle of the edges, than at the corners of the hexagon.

The variation in local orientation must be accompanied by anisotropic changes in the lattice constant, thus stresses must be present already, in the coherent lattice. A very telling picture is in the lower row of Fig. 6.12. Bonds between first neighbors have been calculated and colored according to their lengths. White color indicates the ideal lattice constant, red means bonds are longer than the ideal and blue means shorter separations. While the neutral value used in the coloring is possibly too large (too much blue color in the bulk crystal), there is clearly an oscillation in the lattice constant, which increases in amplitude towards the edges of the hexagon.

While no externally imposed stress is present in the case of single crystals, the dynamic partitioning of the coarse-grained density can induce a surface stress. Together with the anisotropy of the surface free energy in the case of large undercoolings, these effects result in heterogeneous growth conditions along the perimeter of the hexagon. Even in the case without fluctuations, the formation of defects is observed, above a certain size of the crystal, around 450 dimensionless units. The inclusion of thermal fluctuations leads to defect formation at a much smaller

size, around 150 units. It is conceivable, that an ATG-like instability develops in the interface structure, which in the presence of fluctuations leads to an earlier symmetry breaking and formation of misfit dislocations.

6.3 Heterogeneous nucleation in forced convection

In practical situations, nucleation is frequently a heterogeneous process, container walls or other impurities lead to faster nucleation rates, than the homogeneous nucleation path would have predicted. Even if foreign particles manage to reduce the nucleation barrier, their crystal structure might not be compatible with that of the nucleated crystal. The evolving clusters would experience stress, which could influence further crystal growth.

This phenomenon is discussed in Ref. [107], where colloidal experiments and Brownian dynamics simulations were analyzed in this regard. They have found, that at first, clusters nucleate heterogeneously and grow on a seed particle, but as soon as a critical size is reached, supposedly due to elastic stress they detach from the seed particle. The detached crystals grow and remain close to the seed particle and prevent further nucleation events. This finding made us wonder, whether the presence of convection in the fluid would transport the nucleated and detached cluster away from the seed particle and repeated nucleation events would occur.

The continuum modeling of these conditions warrant a hydrodynamic approach, combined with the possibility of heterogeneous nucleation. Because of the transport of grains, the model must be able to support the displacement of solid clusters without any ”drag” from the coordinate system. The HPFC model, as described in Sec. 4.4.2 seems like the obvious choice for such a task. We have faced with difficulties, however, when we tried to create a situation, in which solid crystals would move under forced convection of the fluid. As it were, the periodic pattern of the crystal was not affected by the velocity field of the medium.

We have recently formulated [46] another hydrodynamic extension of the PFC model, called the incompressibly advected HPFC or INCA-HPFC model, described in Sec. 4.4.3 to address these difficulties and for further study of complicated crystal growth scenarios coupled to fluid flow. A situation similar to the one described in Ref. [107] has been constructed. We have applied a fixed, external potential field to represent the interaction with an unstructured circular substrate and set up source terms in the INCA-HPFC equations to force convection on the edges of the

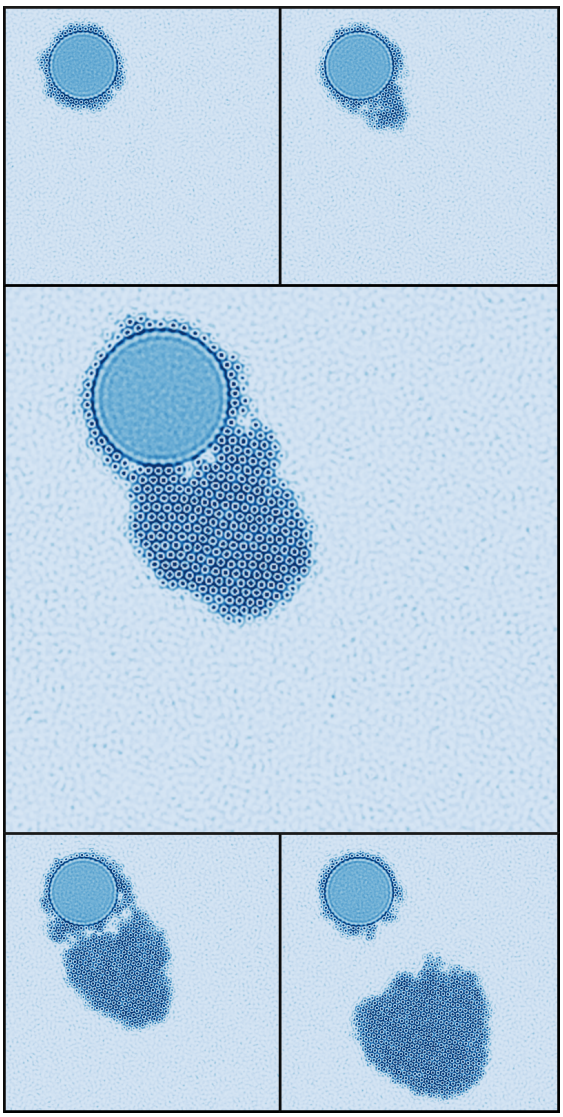

Figure 6.13: Crystal nucleation on an unstructured circular substrate in the presence of fluid flow in the INCA-HPFC model. The downwind side of the substrate provides the necessary circumstances for heterogeneous nucleation and growth. After reaching a significant size, the cluster is broken off by the force from the convection of the fluid domain and it is transported freely in the liquid.

periodic domain of the simulation.

The setup is depicted in Fig. 6.13. A flow field develops around the substrate, pointing, on average, from the upper left corner of the domain towards the lower right corner. In time, the substrate accumulates crystalline ordering on its surface and induces nucleation on its downwind side. As the nucleated crystal domain grows, soon it reaches such a large extent, that the elastic force holding the cluster attached to the substrate proves to be inadequate to hold the cluster in place. The shearing force from the surrounding fluid parcels manage to break off the cluster, free from the substrate. After this event, the cluster reaches the velocity of the fluid and it is transported away from the substrate. Finally, the substrate is able to facilitate further nucleation events. The above scenario is very likely to happen during industrial solidification processing.

6.4 Contributions

I have studied crystallization kinetics in two distinct extensions of the DPFC model, applicable to undercooled molecular liquids. In the HPFC model developed by Tóth et al., I have documented a transition of growth forms from an isotropic one at low undercoolings, to a highly anisotropic hexagonal one, at high undercoolings. I have fitted the Johnson-Mehl-Avrami-Kolmogorov model to the time development of solid fraction. The Avrami exponent turned out to be $p = 3.31$, which is larger, than the expected value of 3, indicating an increasing nucleation rate in time. I have studied athermal nucleation on a solid substrate, the results are in accord with the free growth limited model of Greer et al.

I have observed in the HPFC model, that in the presence of momentum fluctuations at large undercoolings, an initially single crystal develops new crystallographic orientations, which I have identified as GFN, the mechanism responsible for the development of polycrystalline growth forms. I have described two distinct underlying microscopic mechanisms: (1) dislocations entering the hexagonal crystal along its perimeter, which appear to be misfit dislocations, (2) small crystallites nucleating in the neighborhood of the solid-liquid interface, which emerge from the interaction of the density fluctuations in the liquid and the solid-liquid interface. The HPFC model appears to be the first atomic scale model, which supports GFN in the metastable liquid regime. I have analyzed single crystal growth without thermal fluctuations and showed clear evidence, that strain is present near the perimeter of the anisotropic growth form. While the direct cause of this change in lattice constant is not clear at the moment, I have concluded, that the first

mechanism of GFN is clearly a result of internal stresses in the solidification front, which results in the capturing of misfit dislocations during growth.

Due to a deficiency of the HPFC model, namely, that the derived velocity field was not able to transport the atomic density pattern of the crystalline domains, I have recently developed the so-called INCA-HPFC model to address the interaction of the undercooled melt with a foreign substrate. I have shown, that forced convection around a substrate in an undercooled melt results in heterogeneous nucleation of crystalline clusters on the downwind side of the substrate. When the crystal reaches a certain large size, the shearing forces from the fluid parcels tear the crystal off of the substrate, which is transported away. Afterwards, the substrate is able to facilitate further nucleation events. I have thus demonstrated, that it is indeed possible to address in a *single order parameter* model stochastic nucleation of crystals on foreign particles, elastic cohesion of crystalline particles, plastic deformation when elastic forces are overcome, interaction between fluid and solid parcels due to shearing forces and free advective transport.

Chapter 7

Epitaxial studies

The field of epitaxy is the study of nucleation and growth of crystalline materials on top of supporting crystalline substrates. When the new phase is of the same material as the substrate, we talk about homoepitaxy, otherwise it is termed heteroepitaxy.

Epitaxial growth plays a crucial role in the fabrication of advanced semiconductor devices, as it is the fundamental process that enables the integration of different materials with distinct properties into a single device structure. It is used to deposit the active semiconductor layer on a substrate, allowing precise control over its thickness, composition and doping profile, facilitating the production of integrated circuits, light-emitting diodes, laser diodes, photovoltaic devices, many electronic and optoelectronic components and other nanoscale structures.

Basically, it is the controlled growth of a thin crystalline film on a substrate, where the film adopts the crystal structure and orientation of the underlying substrate. This precise alignment between the film and substrate allows for the creation of high quality, defect free films with tailored properties. By growing epitaxial layers of semiconductor materials with specific bandgaps and refractive indices, it becomes possible to create efficient light-emitting structures, those used in the development of optoelectronic devices such as LEDs and laser diodes. These devices find applications in solid-state lighting, displays, telecommunications and optical data storage.

Bulk thermodynamics determines the stability of different crystal structures and phases under specific growth conditions, dictating the choice of growth parameters such as temperature and pressure. Kinetics, on the other hand, deals with the rate at which atoms or molecules attach to the growing surface, processes such as surface diffusion, nucleation and growth modes strongly influence the film's

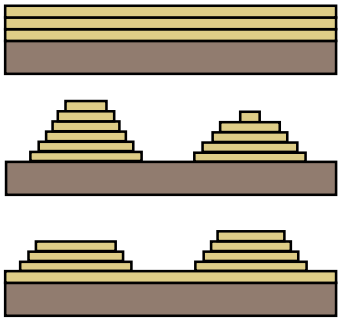

Figure 7.1: Illustration of growth modes, from top to bottom: layer-by-layer growth, island formation and the mixed Stranski-Krastanov mechanism.

morphology, crystal quality and growth rate. Since epitaxial growth involves a substrate and the growth of a controlled number of layers, it is inherently situated in dimensionality between two and three, surface effects contribute generously to the behaviour of such systems, thus surface science plays an important role in epitaxial growth, providing insights into surface structures, reconstructions and surface reactions.

Experimental techniques, such as scanning electron microscopy (SEM), scanning tunneling microscopy (STM) and reflection high-energy electron diffraction (RHEED) are used to study surface morphology, surface diffusion and layer-by-layer growth.

The PFC model of thermodynamic origin, extended with a Langevin-type mass conserving equation of motion, occupies an ideal place of modeling hierarchy, for the study of epitaxial phenomena. Since it resolves matter on the atomic scale and its functional is minimized by periodic patterns of the desired symmetry, elastic effects are naturally taken into account and coupling of the growth front with external and internal stresses are accomplished without any complication. The time scale of the model also means, that it is computationally efficient, since atomic vibrations are averaged out, their footprints can only be discerned in the shape of the atomic probability density distribution, similarly to vacancy and interstitial concentration, that only affect the average density. Topological defects, i.e. dislocations on the other hand appear as directly observable irregularities of the crystalline atomic order.

7.1 Growth mechanisms and defect formation

Epitaxial growth mechanisms are strongly influenced by the relative interaction strength between adatoms and the substrate. In liquid phase epitaxial growth, the determining factors are the relative surface free energies of the adjoining phases, γ_{CL} of the crystal-liquid, γ_{CS} of the crystal-substrate and γ_{LS} of the liquid-substrate interface. Young has studied the stability of planar interfaces in the absence of elastic effects and concluded, that the necessary condition is $\gamma_{\mathrm{LS}} > \gamma_{\mathrm{CL}} + \gamma_{\mathrm{CS}}$, which leads to the complete wetting of the substrate. For non-complete wetting, the contact angle Θ can be defined via $\cos\Theta = (\gamma_{\mathrm{LS}} - \gamma_{\mathrm{CS}})/\gamma_{\mathrm{CL}}$. With the help of the expression $\Delta\gamma = \gamma_{\mathrm{CL}} + \gamma_{\mathrm{CS}} - \gamma_{\mathrm{LS}}$, three growth scenarios can be distinguished, see Fig. 7.1:

- layer-by-layer growth occurs for $\Delta\gamma < 0$, the Frank-van der Merwe mechanism,
- island formation occurs for $\Delta\gamma > 0$, the Volmer-Weber mechanism,
- layer-by-layer growth up to a critical thickness followed by island formation, occurs for $\Delta\gamma \approx 0$, the Stranski-Krastanov mechanism.

A common occurrence during epitaxial growth is the presence of mismatch between the crystal lattice of the substrate and that of the epitaxial layers. The simplest way to quantify this mismatch is through the misfit parameter $f = (\sigma_s - \sigma_f)/\sigma_f$, defined as the strain present in the coherent, stressed epilayers. Similarly to the definition of elastic strain $\frac{L-L_0}{L_0}$, it is expressed as the difference between the lattice constants of the stressed layer (equivalent to σ_s of the substrate) and the unstrained epilayers σ_f (that would grow on a perfectly matching substrate), relative to the latter. This definition is unfortunately not consistently used in the literature, one can come across expressions for the misfit parameter with the lattice constants interchanged. This elastic strain has a strong influence on the growth morphology and has a direct and indirect effect on the above pictured growth scenarios.

7.1.1 Heterogeneities during epitaxial growth

The properties of the epitaxial film, including its electronic band structure and transport characteristics depend on the structural integrity of the film. It is recognized, that if the mismatch between a substrate and the growing epilayers is sufficiently small ($f \lesssim 7\%$ [108]), the initial atomic layers deposited will be strained

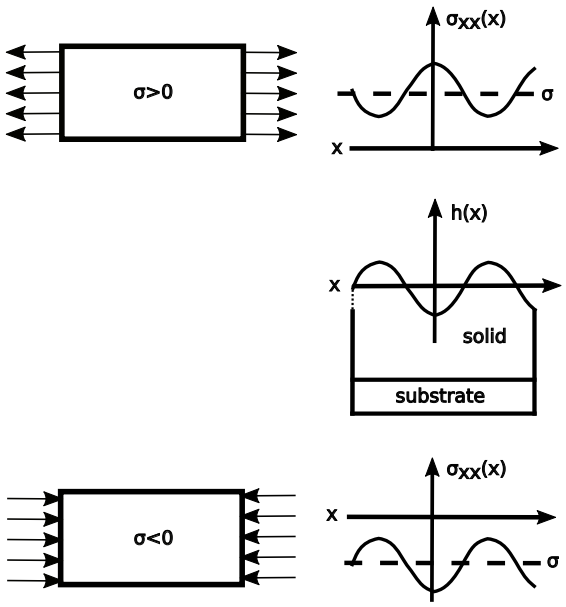

Figure 7.2: Externally strained solid slab develops surface undulations to relieve stress. The upper row shows the tensile, while the lower row shows the compressive case. The middle row depicts the change in surface morphology of the initially planar free surface of the epitaxial layers. Here, σ denotes the stress in the x-direction without surface undulations and σ_{xx} denotes the stress in the presence of undulations.

to conform to the substrate, resulting in the formation of a coherent interface. Inhomogeneities would act as scattering centers in applications, it is thus preferred that films grow defect free and coherent with the substrate.

As the thickness of the coherently growing layers increases (the Frank-van der Merwe scenario), the accumulated excess elastic stress energy becomes more and more significant. Mechanisms have been discovered that act to reduce or eliminate this excess energy.

7.1.1.1 The ATG instability

The equilibrium shape of an inclusion of one phase in another is the result of surface free energy minimization, when the volume of the inclusion is kept fixed. Areas of high curvature are avoided and faces with low values of the surface free energy dominate the equilibrium shape. Planar boundaries between phases at equilibrium tend to remain planar, since modulations in surface geometry have an associated energy cost.

However, taking into account elasticity, leads one to conclude that a change in surface geometry has an effect even on the bulk energy of a strained solid,

thus surface morphology cannot be solely described by the minimization of the surface free energy. Areas of high stress give rise to mass transport to areas of low stress. A perturbation of a planar interface will generally increase the surface free energy contribution and decrease the level of stress, thus the two effects will compete with one another. A sufficiently large reduction in elastic energy will overcome the increase in surface energy and leads to the morphological instability of a planar interface, this became known as the Asaro-Tiller-Grinfeld (ATG) [105, 106] instability.

A transversal sinusoidal surface modulation $h(x)$ along the x-direction is depicted in the middle row of Fig. 7.2, and the x-component of the stress tensor $\sigma_{xx}(x)$ is plotted in the upper and lower rows. The stress distribution is such, that at the peaks of the modulation the stress level is closer to the unstressed state, while at the troughs the stress level is the highest in absolute value.

When the total change in surface and elastic energy is calculated, e.g. as in the review article by Müller and Saúl [109], one obtains that an overall free energy reduction is possible when the wavelength of the modulation λ exceeds a critical one $\lambda > \frac{\gamma\pi}{\sigma^2}\frac{E}{1-\nu^2} = \lambda_c$ where γ is the surface energy, E is Young's modulus and ν is Poission's ratio. In this approximation the sign of the stress has no effect on the instability. Thus ubiquitous thermal fluctuations in the shape of the interface, above this critical wavelength, will be more pronounced.

The stress distribution in the interface as described above will also have an effect on the growth velocity of the interface. The time evolution of the system is driven by free energy minimization, the crystal (F_e) grows due to occupying a lower free energy state $\Delta F_e = F_e - F_l < 0$ than the liquid (F_l), and the growth velocity as a first approximation is proportional $v_{\text{sol}} \propto |\Delta F_e|$ to this free energy difference. This difference $|\Delta F_e|$ is largest for the unstressed crystal, and smaller for crystals under stress (energy closer to liquid's), thus areas of reduced stress (peaks in the modulation) will grow at a faster rate compared to areas of increased stress (troughs in the modulation). This effect will in time increase the amplitude of an initially small modulation, as displayed in the series in Fig. 7.15.

The late time growth morphology of such an instability has been studied in [110] with the help of phase-field modeling extended with linear elasticity theory. It is notable that troughs of the modulation develop into deep, crack-like features. This result is in contrast to PFC simulations that predict dislocation nucleation at late times, thanks to the natural incorporation of the crystal lattice in the modeling, as opposed to the lack of such lattice in the phase-field model.

Figure 7.3: Dislocation lines running perpendicular to viewing plane, in the case of an incoherent interface between substrate (A) and epilayers (B). Periodicity is determined by the misfit parameter, as to fully relieve strain in the epilayers.

7.1.1.2 Formation of misfit dislocations

It has been observed, that during layer-by-layer growth of a mismatched, but coherent epitaxial layer, elastic energy continuously builds up, until a point is reached, when the system could attain a lower energy state by the creation of a so called misfit dislocation and cease further accumulation of elastic strain in successive layers.

van der Merwe (VDM) [111] was first, to develop a theoretical understanding based on an energy balance argument. According to the geometry depicted in Fig. 7.3, the interfacial energy between the substrate (A) and the epilayers (B) was calculated for a given value of the misfit parameter f, meaning a constant linear density of dislocations in the interface was presumed. With the help of a harmonic lattice model the calculated excess interfacial energy is $\epsilon_I \approx 9.5 f \frac{Gb}{4\pi^2}$, G being the shear modulus, b is the length of the Burger's vector, and (for later) ν is Poisson's ratio. This expression is independent of film thickness and is applicable for small ($f \lesssim 4\%$) misfits. This was contrasted with the case without dislocations, i.e. a coherent interface between substrate and epilayers. The areal energy density in this case becomes $\epsilon_H = 2G\left(\frac{1+\nu}{1-\nu}\right) f^2 h$ which is naturally proportional to layer thickness h and quadratic in the misfit, since $f = 0$ represents the lowest energy possible for homogeneously strained layers.

Van der Merwe concluded that there exists a critical layer thickness, above which it is energetically favorable to relieve further stress by the incorporation of dislocations. The condition of total elimination of defects is obtained by equating $\epsilon_I = \epsilon_H$ the above expressions, the approximate critical layer thickness is given by

$$h_c \approx 0.13 \left(\frac{1-\nu}{1+\nu}\right) \frac{b}{f} \,. \tag{7.1}$$

Matthews and Blakeslee (MB) [112] conducted an experimental investigation of multilayered epitaxial growth, it was found that for a given misfit strain, the multilayer structure was devoid of threading dislocation lines below a certain layer

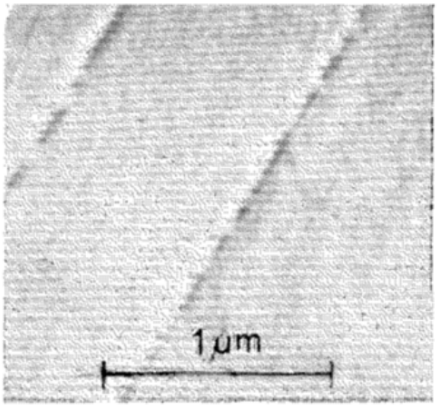

Figure 7.4: Side view of a multilayer structure on a scanning electron micrograph, taken from Ref. [112], layer thickness is around 440Å, dislocation lines run perpendicular to the viewing plane and repeat in each layer.

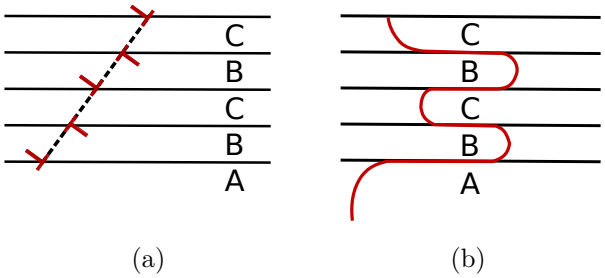

(a) (b)

Figure 7.5: The graphical representation of a threading dislocation, originating from the substrate (A) and running through the multilayer structure (of alternating composition, B and C). Left panel is the same view as in Fig. 7.4 and the right panel shows the section congruent with the dashed line.

thickness, while an array of dislocation lines appeared in the prepared samples as shown in Fig. 7.4 above this critical layer thickness. The graphical representation of the same view is seen on the left panel of Fig. 7.5, while the extent of the dislocation line along the section indicated by the dashed line is seen on the right panel.

MB have developed a more involved theoretical model than van der Merwe, for the prediction of the critical layer thickness, to resolve the discrepancies between theory and experiment. They have approached the problem from a force balance perspective. Fig. 7.6a depicts epilayers of different thickness (B) on top of a substrate (A) with a threading dislocation already present at the beginning of the growth process. The figure shows the progression of changes in the shape of the dislocation line as the epilayer thickens. Starting from state (a), initially the

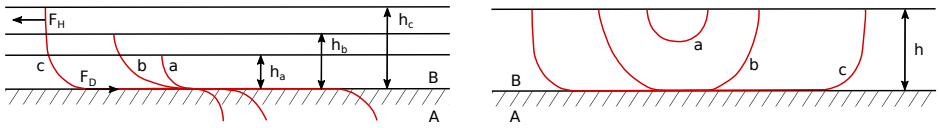

(a) (b)

Figure 7.6: Dislocations in an epitaxial layer, viewed from the same direction as Fig. 7.5b. On the left side (a) the Matthews-Blakeslee force balance is illustrated in the case of a pre-existing threading dislocation, originating in the substrate. Layer thickness directly influences the force acting on the dislocation line, a - subcritical, b - critical and c - supercritical case. For layer thicknesses larger than h_b, the dislocation spreads freely in the substrate-epilayer interface. On the right side (b) a half-loop dislocation line is illustrated, which nucleated in the free surface of the epilayer. The labels a,b,c belong to the same cases as on the left side, the same explanation applies.

dislocation stays in place, the line tension (denoted by F_D in the figure), which is always present in a dislocation line is large enough to pin its position down. However, there is already a force exerted on the dislocation line (F_H) due to the stress field, caused by the strain in the epilayer. As the thickness increases beyond a threshold value, in this case denoted by h_b, the stress induced force F_H on the dislocation line overcomes the pinning effect of the line tension, and the dislocation line begins to grow in length, leaving misfit dislocations along the substrate-epilayer interface, case (c) in the figure. MB have identified case (b) when the two forces balance out, as the criterion for the appearance of misfit dislocations.

The line tension in Ref. [112] is approximated by the expression $F_D \approx G\left(\frac{1+\nu}{1-\nu}\right) bhf$. In the same work, the force acting on the dislocation line due to the stress field is taken to be $F_H \approx \frac{Gb^2}{4\pi(1-\nu)}\left[\log\left(\frac{h}{b}\right)+1\right]$. Force balance gives the critical layer thickness approximately as

$$h_c/b \approx \frac{1}{4\pi\left(1+\nu\right)f}\left[\log\left(\frac{h_c}{b}\right)+1\right]. \tag{7.2}$$

The above picture depends on the presence of dislocations in the substrate, however MB showed, that essentially the same force balance argument holds in the case, when a dislocation nucleates in the free surface of the epitaxial layers, as illustrated in Fig. 7.6b.

People and Bean (PB) [113] put forward yet another way to calculate critical thickness, motivated by the unsatisfactory results, trying to interpret their experimental data according to the previously described results from both van der

Merwe and Matthews-Blakeslee. Over a significant range of the misfit parameter, severe deviations between the theoretical and the experimental curves for critical thickness was observed.

Rather than considering mechanical equilibrium, PB's argument is more in line with that of van der Merwe. The thickness dependent stress energy is calculated similarly, but instead of the approximation with a harmonic lattice model of the interfacial energy between the substrate and epilayers, the self-energy of an isolated dislocation is used in the determination of energy balance. The presumed position of the dislocation is again in the interface between the substrate and the epilayers, the areal energy density of an edge dislocation, a distance h from the free surface is given by the expression

$$\epsilon_D = (1-\nu)^{-1} \left(\frac{Gb^2}{8\pi a\sqrt{2}} \right) \log \frac{h}{b}$$

with a being the lattice constant of the layers. The energy balance $\epsilon_H = \epsilon_D$ can be written in the following form

$$h_c \approx (1+\nu)^{-1} \frac{1}{16\pi\sqrt{2}} \frac{b^2}{a} \frac{1}{f^2} \log \frac{h_c}{b}. \tag{7.3}$$

The physical picture implied by the above explanation, is that the homogeneous volumetric elastic energy density present in the coherent expitaxial layers, multiplying with the layer thickness, can be regarded as an areal energy density present in the substrate-layer interface. Also, the volumetric elastic energy density of an isolated dislocation line can be integrated in the perpendicular plane which results in a line energy density, see e.g. Ref. [114], and it is hypothetically converted to an areal energy density, by dividing it with the lattice constant a. Thus, the condition of the appearance of a dislocation is that the surface energy from elastic stresses at any point in the surface-epilayer interface be larger, than the energy density of an isolated dislocation distributed over the width of the lattice constant.

Apparently PB (erratum in Ref. [115]) have found excellent agreement between this theoretical result and their own experimental data over a range $1\% \lesssim f \leq 4\%$ of misfit parameter.

7.2 Two-dimensional PFC modeling of epitaxy

The PFC theory is an ideal tool for the modeling of epitaxial growth. The use of the one-particle atomic number density as order parameter, inherited from classical

density functional theory, means, that crystal symmetry and elasticity are modeled with ease, these turn out to be essential for these studies. Changes in microscopic structure are reflected as changes in free energy. The thermodynamic driving force for crystallization is easily tuned by changing the chemical potential. Material parameters, such as the elastic properties of the solid or the width of the solid-liquid interface are easily adjusted with model parameters, which represent the strength of correlations in the homogeneous liquid.

The diffusive dynamics is driven by free energy minimization, which has the benefit of not resolving fast degrees of freedom associated with non-dissipative processes, such as phonon propagation, since these do not contribute essentially to the growth process. Time dependent studies are vital, since the final state of the solidified pattern is path dependent, in many of the technologically important cases the system will stay in a metastable local equilibrium, for a significant amount of time.

7.2.1 Accounting for substrates

Different ways of constructing a substrate exist in the framework of the PFC model. Depending on the specific needs of the study, technically simpler or more complicated solutions can be selected. For example, if differences in properties such as lattice structure, driving force, miscibility, diffusion constant between the substrate and the crystal are important, one might use a two-component or binary (see Ref. [1]) extension of the PFC model, which to our knowledge has not been cosidered for the modeling of epitaxy.

Our investigations concern the effect of misfit strain on epitaxial growth, thus from our perspective the most important aspect of a substrate is, that it strains the growing layers along a selected dimension. The aim is to introduce an inert substrate, that acts similar to a boundary condition for the evolution of the order parameter. The substrate can be characterized by its crystal symmetry, lattice constant and interaction strength. The tuning of these parameters are easily accomplished using an external potential, which are frequently employed in DFT studies, set out to model the changes in liquid properties under conditions of confinement, often in porous media or in the presence of surfactants.

A spatially inhomogeneous external potential $V(\boldsymbol{x})$ has the effect on the system of changing the intrinsic chemical potential $\mu = \frac{\delta F}{\delta \rho}$, i.e.

$$\mu_{\text{tot.}} = \mu_{\text{int.}} + \mu_{\text{ext.}} = \frac{\delta F}{\delta \rho} + V(\boldsymbol{x}) = \frac{\delta}{\delta \rho}\left[F + \int \mathrm{d}\boldsymbol{x} V(\boldsymbol{x})\, \rho(\boldsymbol{x})\right]$$

it thus appears as a linear coupling term in the free energy expression. In this chapter, the external potentials used with the PFC model are constructed from a one-mode solution of the PFC functional, as described in App. A.3.

In dynamical simulations, an initial condition for the density field needs to be specified. Had we started the simulations from a liquid state of constant density, since the diffusion equation's eigenmodes relax with $\propto Dk^2$, it would have takes a long time for the density to relax on the largest scales $k \approx 0$ and attain a minimum energy configuration as determined by the external potential. Our aim, is to prepare an inert substrate, which is in equilibrium with the stable liquid. This slow relaxation process to a new equilibrium due to the substrate is not interesting from the perspective of epitaxial growth, it results from the means of the incorporation of the substrate. It is therefore advantageous, to obtain an initial density distribution for the dynamical simulations using the Euler-Lagrange equation, described in Sec. 4.1. During this initial relaxation, the system is open to particle transfer. As boundary condition, the chemical potential is specified at such a value, that leads to the required far-field density. The model parameter ϵ is chosen to represent (together with the far-field density) a stable liquid equilibrium point in the phase diagram, outside the coexistence region, but as close as possible to the value used later in the dynamical simulation, when undercooling is required to initiate growth.

In our simulations, the substrate produces uniaxially strained epilayers. Only one-dimensional strains are considered, much like in the previously mentioned theories. In three-dimensional simulations (two-dimensional substrate-epilayer interface) the possibilities for inducing strain are numerous and the problem can get quite complicated due to three-dimensional crystal structures, but it is not clear, whether that increased complication would lead to a better understanding of the basic principles of defect formation.

7.2.2 Prior PFC studies

Since the inception of the diffusive PFC (DPFC) model [1], there have been numerous studies on liquid phase epitaxy. As a first application of the PFC model in Ref. [1] and later in Ref. [89] a good agreement with the theoretical and experimental work of Matthews and Blakeslee [112] was obtained regarding the misfit dependence of the critical layer thickness. The necessary qualities to successfully model such behavior, namely the morphological instability to interface buckling and the nucleation of dislocations, was demonstrated to be present in the frame-

work of the PFC model. Additionally, compositional instability during heteroepitaxial growth, i.e. the effect of phase separation of multiple species during film growth was addressed in Ref. [20], using the binary extension of the PFC model.

An inconsistency in definitions has to be pointed out. As described in Sec. 7.1, the definition of the misfit strain is $\frac{L-L_0}{L_0}$, L being the stretched or contracted length, and L_0 denotes the stress-free length. In the above cited works, an alternative definition is employed, see Ref. [1], the misfit parameter is defined as $\frac{\sigma_{\text{film}}-\sigma_{\text{bulk}}}{\sigma_{\text{bulk}}}$ in which σ_{film} stands for the unstrained (ideal) lattice constant of the epilayer and σ_{bulk} for that of the substrate's. Unwisely, in our publications [116, 117] the same convention was used. This oversight is corrected in this dissertation and the definition $f = \frac{\sigma_{\text{substrate}}-\sigma_{\text{film}}}{\sigma_{\text{film}}}$ is used consistently.

7.2.3 Continuous cooling study

We have completed continuous cooling simulations, along the path denoted by thick red bars in Fig. 7.7, in which the model parameter ϵ was increased in time, from a lower value in the liquid part of the phase diagram, up to a higher value, coinciding with the liquid stability limit. A square lattice substrate was employed, whose lattice constant was varied according to the desired misfit. The change in ϵ serves as a means to a constant, low rate of solidification. The density increase upon freezing would cause the depletion of the liquid part of the domain and ultimately decrease undercooling and solidification velocity, due to the local and global conservation of density. The noise parameter was set to $A_{\text{noise}} = 10^{-4}$ for all the simulations, except the ones concerning Fig. 7.10, where the noise dependence of the critical thickness was investigated explicitly.

7.2.3.1 Small interface anisotropy

The model parameter ϵ was increased from $\epsilon = 0.1$ up to $\epsilon = 0.1875$, this amounts to low, metal-like anisotropy values. The cooling path during the simulation is represented by the thick red bar on the right in Fig. 7.7. Depending on the magnitude of misfit, we have observed all three growth modes of heteroepitaxy (as described in Sec. 7.1). The change in surface morphology is presented in Fig. 7.8, where together with the atomic number density, the Voronoi cells, calculated from the positions of the atomic density peaks are also shown. As described in App. C.2, Voronoi analysis is a useful tool in two dimensions to visually differentiate regions of intact ordering from defected ones. In the minimum energy state of the PFC model, atoms occupy the vertices of a triangular lattice, while the geometrical dual

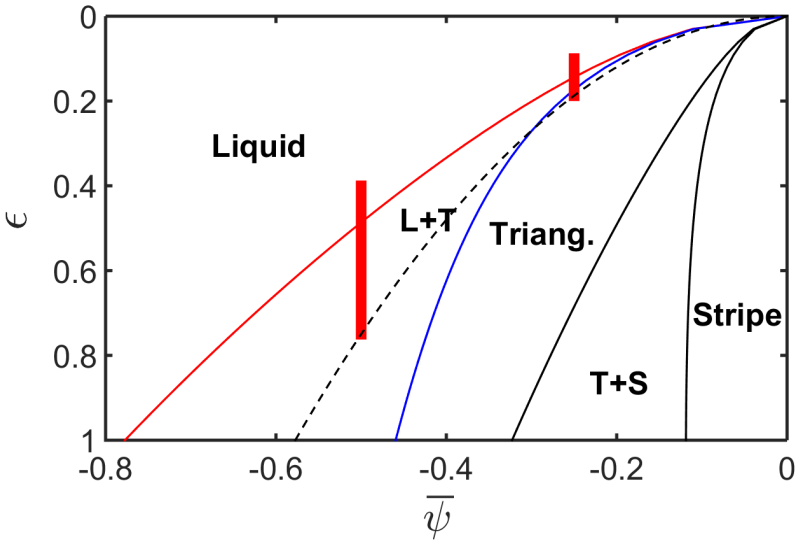

Figure 7.7: Phase diagram (from Ref. [116]) of the two dimensional PFC model in the reduced temperature ϵ vs. reduced density $\overline{\psi}$ plane. The thin solid lines denote the borders of the domains of stability: liquidus, red, 1st from left, solidus, blue, 2nd from left. The dashed line is the linear stability limit of the liquid $\left(\epsilon = 3\overline{\psi}^2\right)$, beyond which it is unstable to fluctuations and unconditionally transforms to a solid. "L + T" stands for the coexistence region of the liquid and triangular phases, "Triang." denotes the triangular crystal structure, "Stripe" stands for a striped or lamellar phase, irrelevant from the point of view of this study, but can be reached at large supersaturations, whereas "T + S" denotes the coexistence domain of the triangular and striped phases. The thick red bars indicate the cooling paths as described in the text, the left for large and the right for small anisotropy.

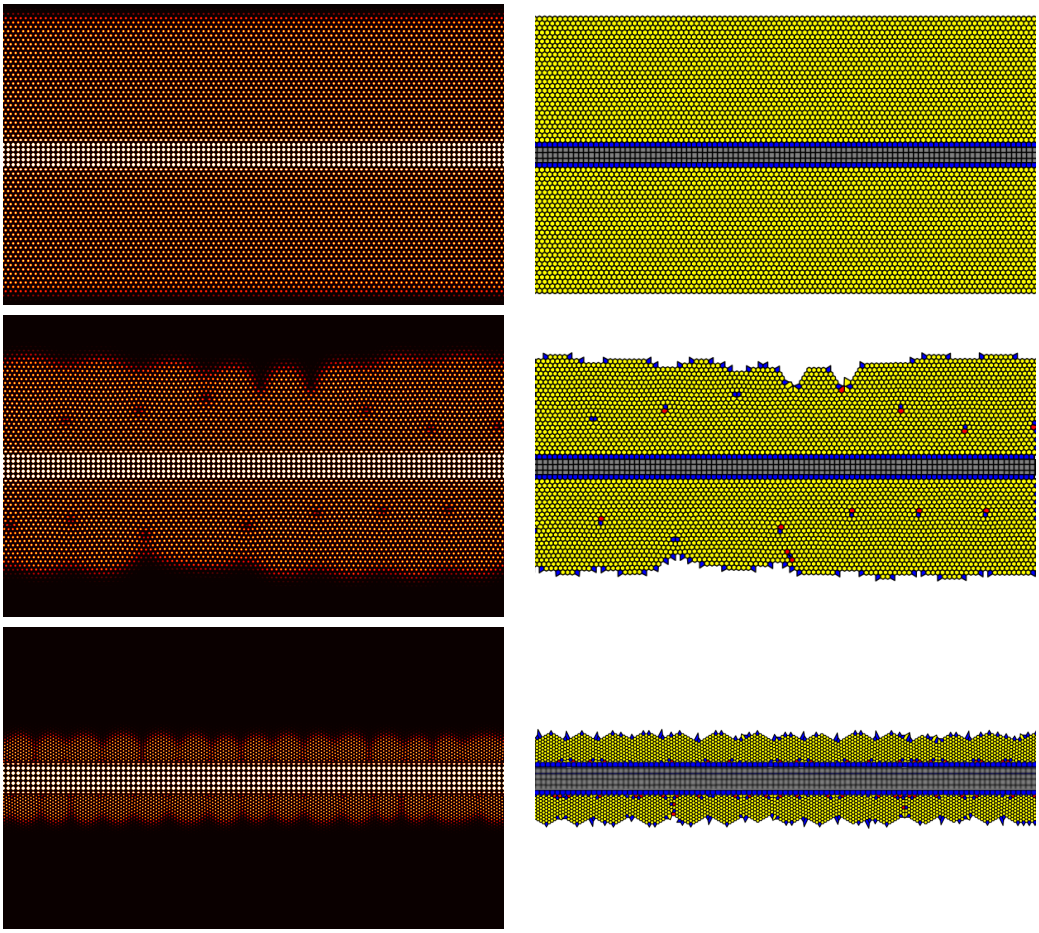

Figure 7.8: Change in surface morphology solely due to lattice mismatch, low anisotropy. The substrate is a square lattice, of varying lattice constant. Model parameters are $\overline{\psi} = -0.25$, $\epsilon = 0.1 \rightarrow 0.1875$ (continuous cooling), top row: $f = 0$, middle row: $f = 0.07$, bottom row $f = 0.6$. In the left column the atomic density field $\psi(\boldsymbol{r})$ is plottted, while in the right one, the Voronoi cells are shown. Polygons are colored according to the number of their sides, with 6 sides, the natural ordering in two dimensions of the PFC model are colored yellow, while polygons with 4, 5 and 7 sides are colored gray, blue and red.

of this point set is a hexagonal lattice, in which each and every hexagon belongs to a single atom and represents the space closer to that atom, than to any other. A dislocation, which in two dimensions is the presence of an additional row of atoms in a finite region of otherwise topologically perfect lattice, shows up as a pair of 5 and 7 sided (blue-red) Voronoi cells. Because of issues of numerical precision, these do not show up as 5-7 pairs in every instant, but perturbations in the atomic positions lead, on average, to the same statement.

All three theoretical results for the critical thickness, Eqns. 7.1,7.2,7.3 predict a diverging thickness for $f = 0$ zero misfit, this coincides with the top row of Fig. 7.8, where layer-by-layer growth is observed with a flat, but diffuse interface. For small values of misfit, the vertical size of the simulation window limits the largest observable critical thickness.

For large enough misfits ($f = 0.07$ in the second row of Fig. 7.8), an initially flat interface grows, that develops undulations due to the Asaro-Tiller-Grinfeld instability, as described in Sec. 7.1.1.1. The ATG interface modulation mitigates stress, for the price of change in lattice constant in the interface. Crystal growth, however, cannot proceed indefinitely with a lattice constant, that is different from that in the bulk crystal. This is the reason, why the initially sinusoidal interface modulation breaks down, as cusps form which shortly engulf dislocation cores, that are not possible to remove due to their topological nature. On a long enough timescale, the dislocations so nucleated proceed towards the substrate, since stress in the coherent layers can be eliminated by the placement of the dislocations closer to the substrate, dislocations screen the elastic field present in the coherent layers. For even larger values of misfit ($f = 0.6$ in the third row of Fig. 7.8), layer-by-layer growth is inhibited from the very beginning, only island formation is realized.

7.2.3.2 Large interface anisotropy

Next, we present the results of continuous cooling simulations of high anisotropy, covalent-like materials, ϵ changes linearly, from $\epsilon = 0.4$ to $\epsilon = 0.75$, see the thick red bar on the left in Fig. 7.7. It is again possible to influence the heteroepitaxial growth mode by tuning the misfit parameter. A diverging critical thickness is recovered for low misfit values, top row in Fig. 7.9, while beyond a larger value of misfit than in the small ϵ case, island formation inhibits the determination of the critical thickness. The amplitude of the ATG modulation at the time of defect formation is significantly smaller, than in the small anisotropy case.

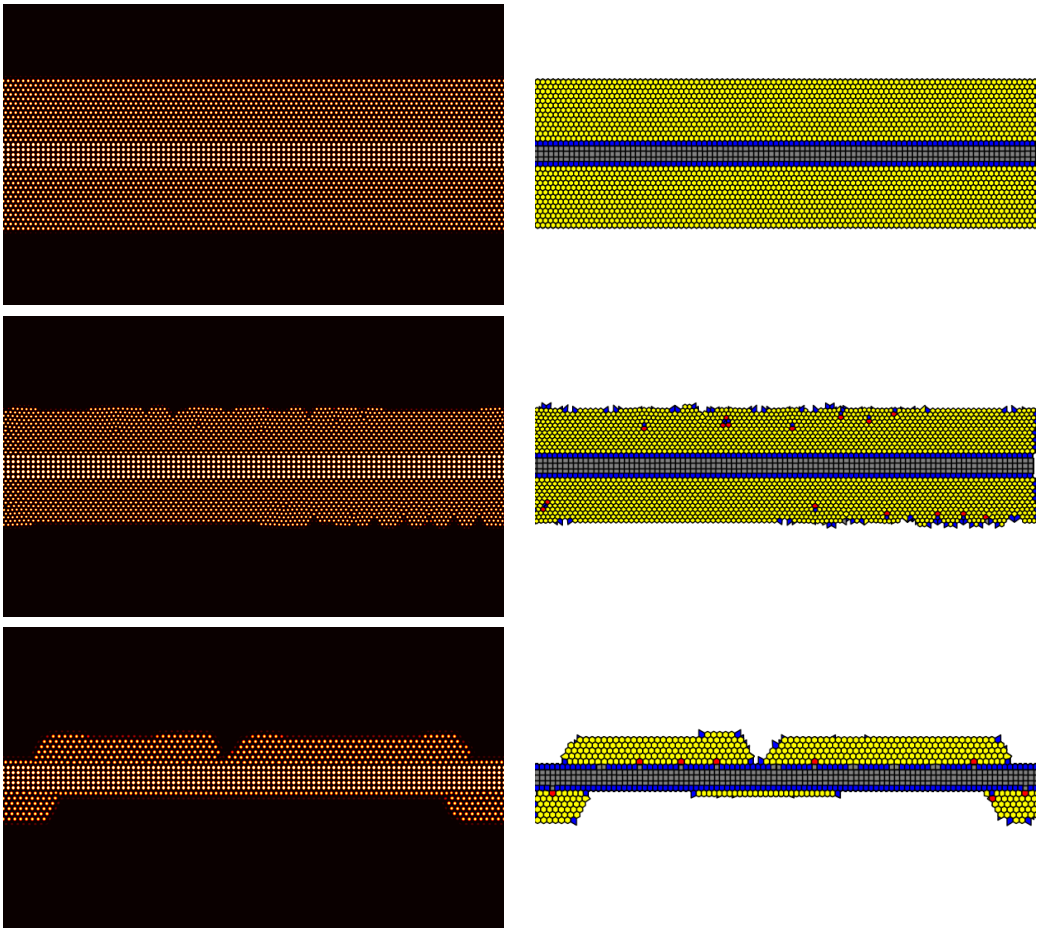

Figure 7.9: Change in surface morphology solely due to lattice mismatch, high anisotropy. The substrate is a square lattice, of varying lattice constant. Model parameters $\overline{\psi} = -0.5$, $\epsilon = 0.4 \rightarrow 0.75$, top row: $f = 0$, middle row $f = 0.19$, bottom row $f = -0.14$. In the left column the atomic density field is plottted, while in the right one, the Voronoi cells are shown. Polygons are colored according to the number of their sides, with 6 sides, the natural ordering in two dimensions of the PFC model are colored yellow, while polygons with 4, 5 and 7 sides are colored gray, blue and red.

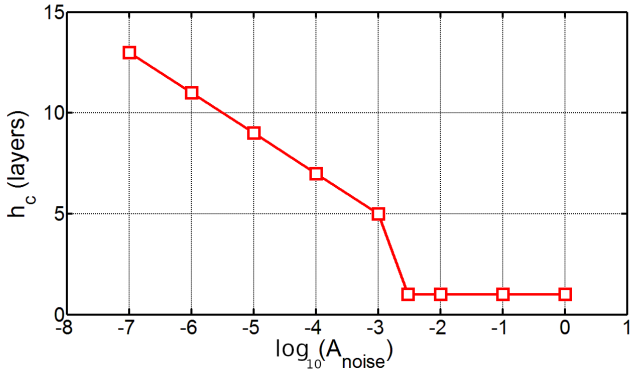

Figure 7.10: Critical thickness plotted against the logarithm of noise strength, explained in Sec. 4.3. Critical thickness drops suddenly to a monolayer approximately above the noise amplitude of 10^{-3}.

7.2.3.3 Effect of noise strength on critical thickness

Apparently, the addition of noise to the EOM influences the onset of the ATG instability, though the qualitative behavior remains the same in a broad range of A_{noise} noise amplitude. The critical thickness has been determined for the case of large anisotropy ($\overline{\psi} = -0.5$, $\epsilon = 0.4 \rightarrow 0.75$), during continuous cooling. The noise amplitude (described in Sec. 4.3) was varied in the range $A_{\text{noise}} \in [10^{-7}, 1]$, the results are summarized in Fig. 7.10. Remarkably, over several decades, the critical thickness decreases linearly wrt. $\log_{10} A_{\text{noise}}$, whereas above $A_{\text{noise}} = 10^{-3}$, it drops suddenly to a monolayer. It is worth noting that in the latter regime, defects appear directly at the substrate-crystal interface, from the very beginning.

7.2.4 Isothermal study

In addition to the continuous cooling studies, we have ivestigated the critical layer thickness in isothermal simulations, which means that the reduced temperature was set to a fixed value of $\epsilon = 0.18$. Three values of the noise parameter were also used, $A_{\text{noise}} = (0, 10^{-4}, 10^{-2})$. A typical situation is depicted in Fig. 7.11 where a crystal of 6 fold symmetry grows from right to left, on top of a square substrate on the right hand side. The Voronoi analysis clearly shows a modulation of $7\lambda = 92\sigma_{\text{film}}$, i.e. $\lambda = 13.143\sigma_{\text{film}}$ is the wavelength of the modulation expressed in unstressed lattice constants. This differs from the number of periods, necessary for total stress elimination, which would be $8\lambda = 92\sigma_{\text{film}}$, i.e. $\lambda = 11.5\sigma_{\text{film}}$. In these isothermal simulations, the divergence of the critical thickness, when approaching zero misfit, is observed yet again.

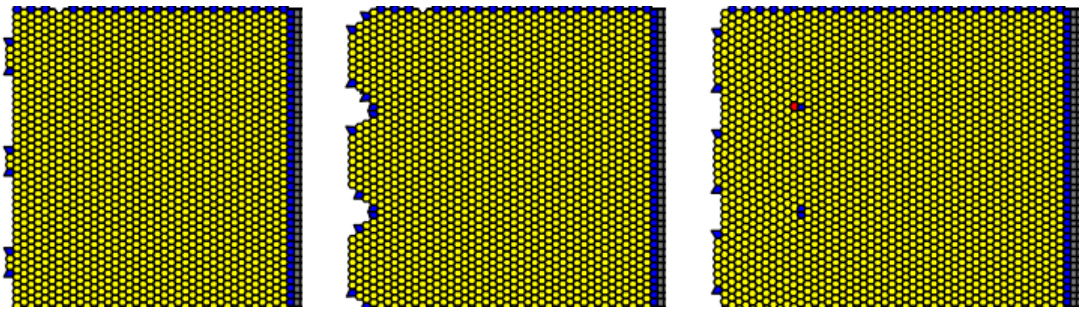

Figure 7.11: Consecutive snapshots of isothermal heteroepitaxial growth of a triangular crystal in a PFC simulation at parameter values $\epsilon = 0.18$, $\overline{\psi} = -0.25$ and $A_{\text{noise}} = 0$, growing on a square lattice substrate. Substrate is on the right hand side, periodic boundary conditions apply in the vertical direction. The simulation cell size in the y-direction is $L_y = 100\sigma_{\text{st}} = 92\sigma_{\text{film}}$, i.e. the lattice constant of the substrate is smaller than that of the unstressed film's, initially the film is under compressive stress. Calculated misfit is $f = -0.08 = -8\%$, there are 8 additional atoms present in the substrate and in the coherent layers. It is remarkable, that only 7 defects form, instead of the 8 expected from the number of extra atoms.

7.2.5 Critical thickness vs. misfit

Simulation results from Secs. 7.2.3,7.2.4 are collated in Fig. 7.12. Looking at the figure, it is obvious that noise has a significant overall effect on the scale of the variation in h_c, also confirmed in Fig. 7.10. The amplitude of the Langevin noise has the effect of shifting the equilibrium phase diagram, but from experience, in the range of $A_{\text{noise}} \in [0, 10^{-2}]$ explored in Fig. 7.12, this effect should be negligible.

In the works mentioned in Sec. 7.2.2, in Refs. [1, 89] and in our own work in Ref. [116], the results for h_c were interpreted in light of the Matthews-Blakeslee theory for epitaxial defect formation (Par. 7.1.1.2). Based on the MB formula (see Eq. 7.2) $h_c/b \approx \frac{1}{4\pi(1+\nu)f}\left[\log\left(\frac{h_c}{b}\right)+1\right]$, when the expression $\left[\log\left(\frac{h_c}{b}\right)+1\right]\frac{b}{h_c}$ is plotted against the misfit f, a linear relationship is expected. The results of this transformation are displayed in Fig. 7.13b.

The MB transformation in some cases clearly does not result in a linear relationship, the smaller the noise amplitude, the worse the correlation becomes. More importantly, the MB expression predicts a diverging critical thickness when zero misfit is approached, however these plots in almost all cases violate the requirement, that straight lines should go through the origin.

Confronted with such discrepancies, in Ref. [117] we have applied the People-Bean theory of defect formation, the expression (see Eq. 7.3) f vs. $\sqrt{\frac{b}{h_c}\log\frac{h_c}{b}}$ is used for the transformation, pictured in Fig. 7.13c. Overall, the plots are closer to straight lines, however most of them still miss the origin, thus we cannot escape

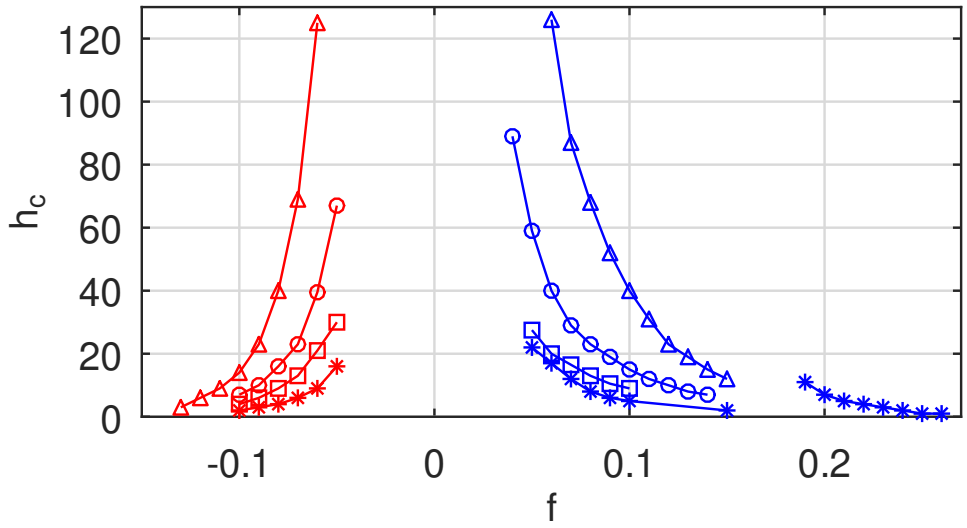

Figure 7.12: Critical layer thickness h_c (measured in the number of layers) vs. misfit f. Compressive strain ($f < 0$) is shown in red, while tensile strain ($f > 0$) is colored blue. Symbols have the following meaning: asterisks denote the continuous cooling studies with $A_{\text{noise}} = 10^{-4}$, the line on the right at high positive misfits is the high anisotropy case, while the other two, at lesser misfits, belong to the low anisotropy case of Sec. 7.2.3. Isothermal studies are plotted according to the value of the noise parameter A_{noise}, triangles for $A_{\text{noise}} = 0$, circles for $A_{\text{noise}} = 10^{-4}$ and squares for $A_{\text{noise}} = 10^{-2}$.

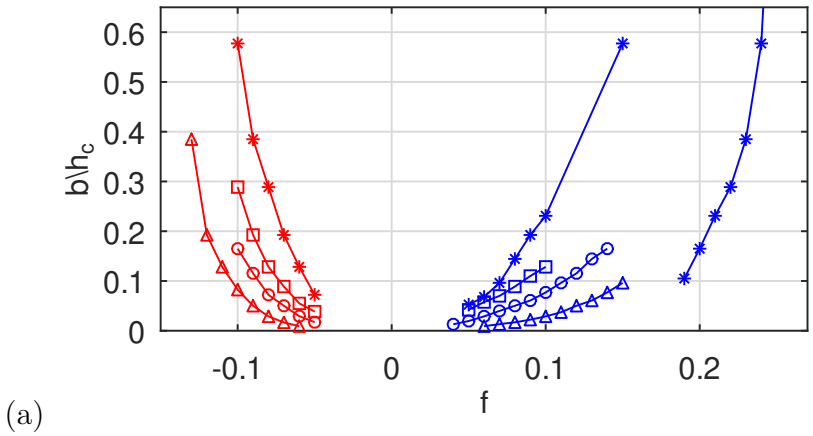

(a)

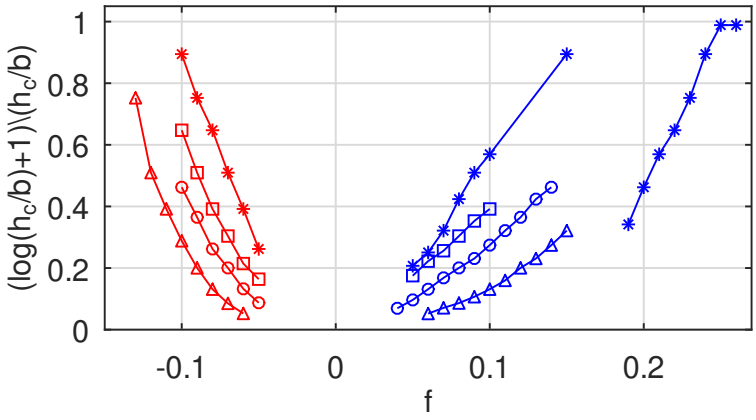

(b)

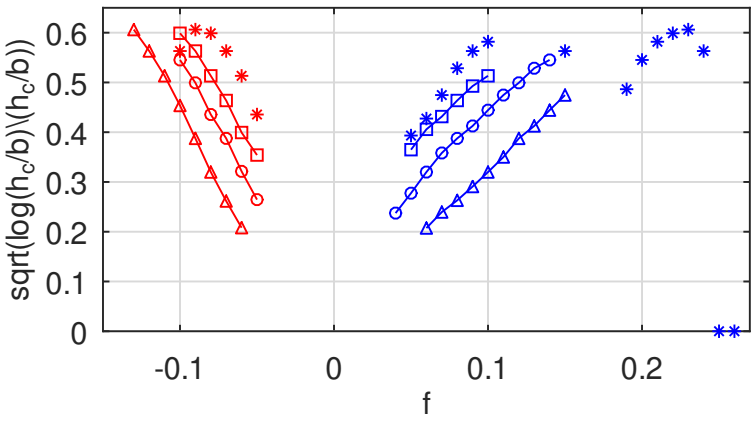

(c)

Figure 7.13: Transformation of the critical thickness values, according to the (a) van der Merwe, (b) Matthews-Blakeslee and (c) People-Bean expressions. Linear relationships were expected, that go through the origin. In (c), data points from the continuous cooling study (asterisks) are not connected, because they no longer "guide the eye".

the conclusion, that the diverging layer thickness is not associated with the zero value of misfit. The results from the isothermal simulations in the zero noise limit for tensile stresses achieve the best fit.

For completeness, in Fig. 7.13a the van der Merwe expression (see Eq. 7.1) f vs. $\frac{b}{h_c}$ is applied as the transformation, unfortunately the graphs are far from straight lines.

7.2.6 Critical assessment of misfit dislocation formation in the PFC model

The theoretical results of Sec. 7.1.1.2 all have in common, that they are based on a static, energetic argument. The Matthews-Blakeslee force balance reasoning can be expressed too, as an energetic extreme value problem, see Ref. [112]. Interface kinetics, i.e. the growth velocity and the development of the ATG instability, do not influence the results of Eqns. 7.1,7.2,7.3. Surprisingly, material properties, such as the shear modulus drop out of the expressions, only the length of the Burger's vector and Poisson's ratio remain. What is more, even the effect of thermodynamic stability is missing, through which temperature could have played a role. It is hard to incorporate the kinetic picture of defect formation into this fully equilibrium, path-independent picture.

In Sects. 7.2.3,7.2.4 we have presented simulations, in which for a set misfit and undercooling, liquid phase epitaxial growth initiates on top of a substrate. It is not immediately obvious, how would these energy balance considerations from Sec. 7.1.1.2 help in explaining the kinetics of defect formation we see *during growth* in the PFC model. Compared to experiments, in a simulation we have significantly more freedom to isolate distinct phenomena and look for an explanation. If defect formation in the PFC model depended chiefly on layer thickness, and not the kinetics, then starting the simulation with different number of epitaxial layers, as long as the initial layer thickness was below the critical thickness, we should be observing defect formation at around the same thickness. Going further with this train of thought, we can actually prepare close to equilibrium initial conditions, with zero growth velocity of the strained, coherent crystal. The free energy of the strained crystal relative to the unstrained one $\Delta\Omega = \Omega_C(f) - \Omega_C(f=0) \propto f^2$ is proportional to the strain squared. The undercooled liquid occupies a higher free energy than the crystal $\Omega_L > \Omega_C$, the difference is termed the driving force of crystallization. For a fixed misfit and reduced temperature ϵ, we can find the appropriate reduced density $\overline{\psi}$ so that the strained crystal is in thermodynamic

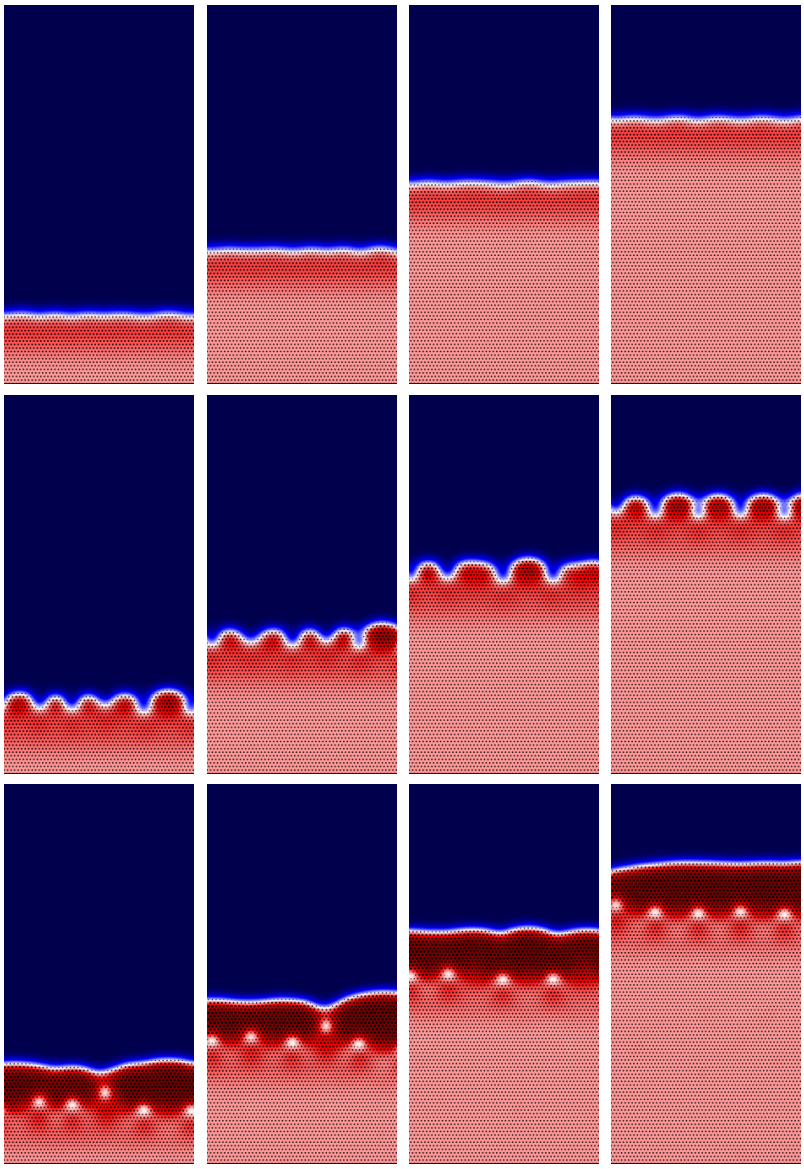

Figure 7.14: Snapshots from EL simulations. Simulation time increases from top to bottom, same system per column. Initial strained layer thickness increases from left to right. The coarse-grained amplitude field (described in App. C.4 is color coded, blue indicates the liquid domain where the amplitude is zero, while in the crystal it reaches a finite, large value. The interface between liquid and crystal shows up as a white stripe in this color scheme. Black dots indicate the position of atoms, the size of the dots correlate with the value of the maxima in the density field. Model parameters are $\epsilon = 0.12$, $\overline{\psi} = -0.2157$, the strained crystal is in equilibrium with the liquid. Compressive strain on the system was induced by an additional 17 atoms over the 200 in the ideal lattice, this amounts to a misfit of $f = -7.8\%$.

equilibrium with the liquid. This point in the phase diagram would correspond to an undercooled state (finite growth velocity) as far as an unstrained crystal is concerned.

If the static energetic scenario is responsible for defect formation in PFC simulations, it should be adequate to study the pseudo time dependent Euler-Lagrange (EL) equation from Sec. 4.1, which describes the time evolution of a hypothetical, open system, in which the chemical potential is kept fixed. We have simulated the change of interface morphology in time. Simulations started from a different number of coherent epitaxial layers, were compared in terms of the time necessary for defect formation. The findings are displayed in Fig. 7.14, in each column the same system is shown at increasing simulation times, from the top to bottom. In the rows, different systems are compared at the same simulation time, initial layer thickness increases from the left to the right.

The effect of strain is clearly visible in the color coded amplitude field (described in App. C.4), blue indicates liquid regions where the amplitude is zero, while the crystal reaches high values of the amplitude. Black dots show the atomic positions, the larger the dot the greater the maximum is in the order parameter at that atom. The unstrained crystal after defect formation clearly reaches higher values in both the amplitude and the atomic maxima.

The main takeaway from this series is, however, that we see no correlation between initial layer thickness and the time and quality of defect formation, which validates the argument that morphological changes in the solid-liquid interface are not connected directly to the ”build-up” of stress energy in the epitaxial layers, as expounded in Sec. 7.1.1.2. It is also clear, that the front velocity has no direct effect on interface morphology, the ATG instability and later, interface buckling happens even at zero growth velocity, although past defect formation a finite growth velocity is observed as expected, since the unstrained crystal experiences a driving force wrt. the unchanged liquid.

To appreciate more the kinetics of defect formation, in Fig. 7.15 a series of snapshots are presented, which display the evolution of a single misfit dislocation, initially in (metastable) thermodynamic equilibrium. After some waiting time, which depends on the amplitude of noise, the ATG interface modulation of a certain wavelength becomes visible. The peaks of the modulation experience a driving force for crystallization, which induces morphological changes beyond the applicability of the ATG linear stability analysis. The interface then buckles and peaks fuse together, covering over a misfit dislocation. Growth then proceeds with the ideal number of atoms per row.

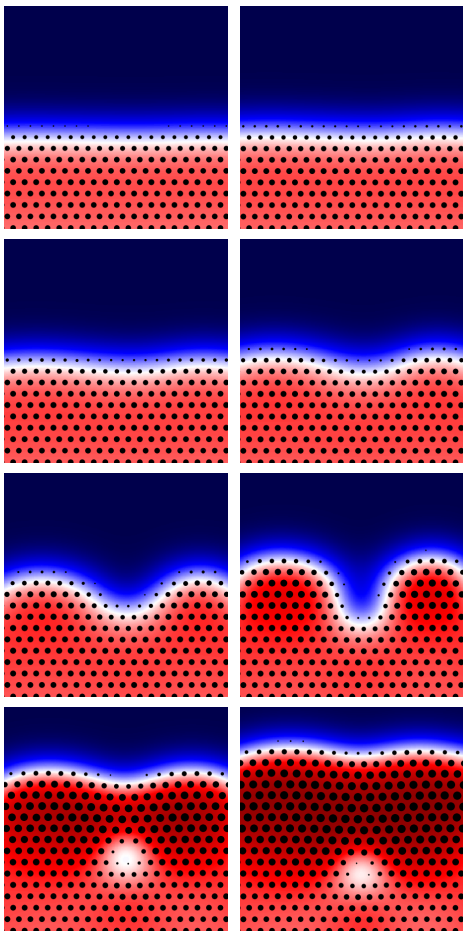

Figure 7.15: Close-up view of single defect formation (dislocation) in an equilibrium EL simulation. Model parameters are $\epsilon = 0.12$, $\overline{\psi} = -0.2157$. Compressive strain of $f = -7.8\%$ is applied. A small portion of the simulated domain is displayed. Time progresses from left to right and top to bottom. Some noise is present in the system, the ATG instability is responsible for the selection and amplification of a certain wavelength of interface modulation. Atomic neighborhoods near the peaks in the modulation of interface position experience a smaller (absolute value) of strain, while neighborhoods near the troughs are strained more, the resulting inhomogeneity in the driving force of crystallization means, that peaks are able to grow, accentuating the initial morphological instability. Eventually the peaks fuse and grow over a defected region of the lattice and the dislocation begins to migrate towards the substrate.

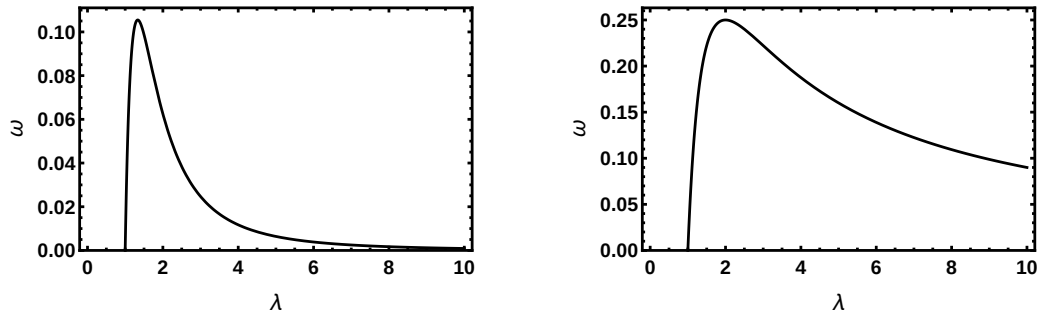

(a) (b)

Figure 7.16: ATG growth factor ω vs. the wavelength of the modulation. In figure (a) the case for a closed system while in figure (b) the case for an open system is shown. The difference between the two comes from an extra factor of k^2 coming from the diffusive mass transport in the case of the conserved dynamics.

Whether the coherent epitaxial layers experience a driving force or not, the dynamical process of the formation of defects starts with the ATG instability. A theory of the critical layer thickness must contain some elements of this phenomenon. We are thus motivated to take a look at the ATG result, once again. In the article by Müller and Saúl [109], linear elasticity coupled to a surface curvature dependent chemical potential in a sharp interface model is reviewed, the prediction for the time evolution of the amplitude $h(t)$ of a surface modulation of wavelength λ is

$$h(t) = h_0 \exp[\omega t], \ \omega = \frac{\gamma D_s n_s \Omega^2}{k_B T} \left(\frac{2\pi}{\lambda}\right)^4 \left(\frac{\lambda \sigma^2}{\pi \gamma} \frac{1-\nu^2}{E} - 1\right).$$

Both thermodynamic and elastic parameters, γ the surface tension, $k_B T$ the temperature, E Young's modulus appear in ω, the growth factor. In the above result the growth prefactor $\left(\frac{2\pi}{\lambda}\right)^4$ depends on the constraint of mass conservation at the modulated interface (surface diffusion results in a factor of $\left(\frac{2\pi}{\lambda}\right)^2$). In an alternative derivation of the growth factor in Ref. [109], when only the free energy difference of the perturbed and unperturbed interface is considered, this energy difference becomes

$$\Delta F = -\frac{\gamma h^2}{4} \left(\frac{2\pi}{\lambda}\right)^2 \left(\frac{\lambda \sigma^2}{\pi \gamma} \frac{1-\nu^2}{E} - 1\right).$$

In our simulations modeling an open system (not limited by surface diffusion), driven by the Euler-Lagrange equation, the time derivative of the amplitude of the modulation is proportional to the negative of the chemical potential, which is the

derivative of the free energy wrt. the changing quantity

$$\partial_t h \propto -\frac{\partial \Delta F}{\partial h} = \frac{\gamma}{2}\left(\frac{2\pi}{\lambda}\right)^2\left(\frac{\lambda\sigma^2}{\pi\gamma}\frac{1-\nu^2}{E}-1\right)h = \omega h\,.$$

The important message is, that a perturbation will grow as long as the wavelength of the modulation $\lambda > \frac{E}{1-\nu^2}\frac{\sigma^2}{\pi\gamma}$ is above a critical one. The growth factor is plotted in Fig. 7.16a for a closed system, the factor λ^{-4} severely limits the growth rate for large values of the wavelength. The same plot for an open system is displayed in Fig. 7.16b.

In the PFC simulations our experience is, that during strained growth, almost as many dislocations form as necessary for total elimination of stress. In Ref. [111] van der Merwe has calculated the interface energy due to the presence of dislocations in the substrate-epilayer interface. He has used the hypothesis, that a given misfit f leads to a linear density of dislocations, that perfectly eliminate the elastic stress in the upper layers. We use the same hypothesis, which in our simulations has some empirical justification. Thus, a direct connection between misfit and the modulation wavelength can be established at this point, since the defintion of misfit $f = \frac{\sigma_{\mathrm{st}}-\sigma_{\mathrm{f}}}{\sigma_{\mathrm{f}}}$ can be inverted, using the relation $\lambda = n\sigma_{\mathrm{f}} = (n \pm 1)\,\sigma_{\mathrm{st}}$ (+ for compressive, − for tensile stresses) as $n = (f+1)\,/\,|f|$. This expression determines the wavelength of the modulation in units of the layer's ideal lattice constant. It is plotted in Fig. 7.17 according to the absolute value of the strain $|f|$, so that we can see the asymmetry between compressive (red) and tensile (blue) strains. This asymmetry is often seen in experiments, however, the theories in Sec. 7.1.1.2 are completely symmetric in the sign of the strain.

The growth factor for an open system with this choice of λ and with the stress expressed as $\sigma = \frac{E}{1-\nu}f$ can be rewritten in the following form

$$\omega \propto \left(\frac{|f|}{f+1}\right)^2\left(\frac{\sigma_f E}{\pi\gamma}\frac{(1-\nu^2)}{(1-\nu)^2}\,(f+1)\,|f|-1\right)\,. \tag{7.4}$$

The constant $\frac{\sigma_f E}{\pi\gamma}\frac{\left(1-\nu^2\right)}{(1-\nu)^2} = \chi$ in Eq. 7.4 can be calculated from model parameters. From Ref. [89] we know, that $\nu = 1/3$, Young's modulus is $E = A_t^2/6$ where the amplitude of the triangular single-mode solution is $A_t = \frac{4}{5}\left(-\overline{\psi} + \frac{1}{3}\sqrt{15\epsilon - 36\overline{\psi}^2}\right)$, the interface free energy from Ref. [27] at $\epsilon = 0.12$ and $\overline{\psi} = -0.2157$ is $\gamma = 0.0011$, so after substitution $\chi \approx 50$ results. In Fig. 7.18 we have plotted the results of several Euler-Lagrange simulations, like the one in Fig. 7.15. The strained epitaxial layers were prepared in thermodynamic equilibrium with the liquid, this meant

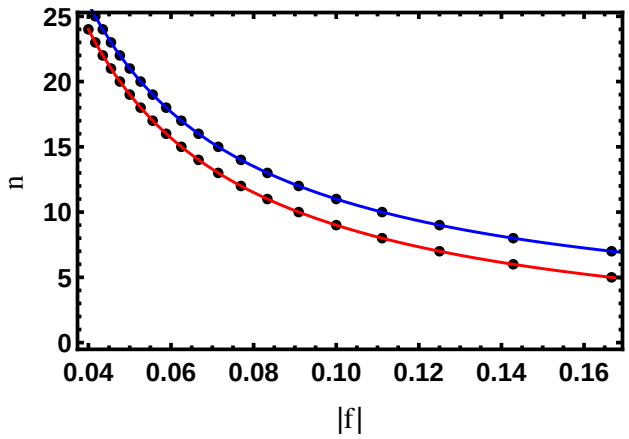

Figure 7.17: The criterion of total elimination of stress, connecting the strain with the wavelength of modulation $\lambda = n\sigma_{\mathrm{f}} = \sigma_{\mathrm{f}}\,(f+1)\,/\,|f|$ results in an asymmetry for compressive (red) and tensile (blue) strains, missing from the basic theories of defect formation, that are symmetric under change of sign.

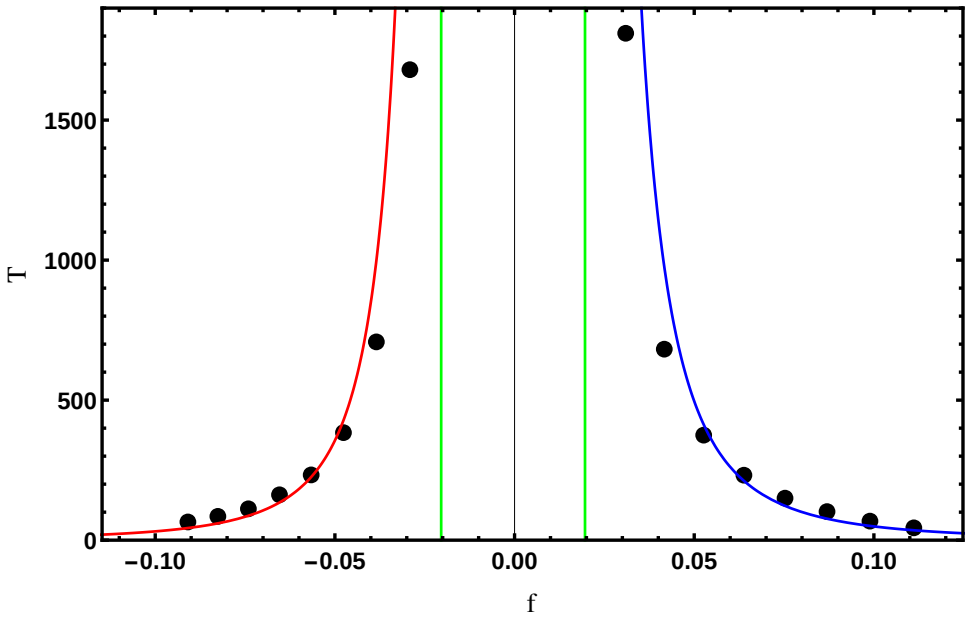

Figure 7.18: Waiting time T (in arbitrary units) for the creation of misfit dislocations during equilibrium (zero growth velocity), in strained triangular epilayers vs. initial strain. The Euler-Lagrange pseudo time dependent equation was solved at a reduced temperature of $\epsilon = 0.12$, average density was set according to the condition of zero growth. The free parameter K was fit in the expression $T = \frac{K}{\omega}$, with ω from Eq. 7.4 and $\chi = 50$. The red line represents a fit for compressive strains and the blue line is a fit for tensile strains. Green vertical lines mark the positions of critical misfits, present in Eq. 7.4.

that the average density needed to be changed according to the misfit parameter. The morphological instability of the interface resulted in surface undulations, close to the previously calculated wavelength corresponding to total stress elimination. The smaller the strain was on the system, the longer it took for defects to form. The time T it took the interface to overgrow a misfit dislocation is plotted on the T-axis in the figure. The exponential time evolution equation for the amplitude of the modulation (strictly applicable only for small amplitudes) $h(t) = h_0 \exp[\omega t]$ can be used to obtain an approximate time for defect formation, when we assume that a defect is formed when a certain value of the amplitude is reached. We obtain $T = \frac{\log \frac{h(T)}{h_0}}{\omega}$ for the defect creation time. This expression is fitted to the data in Fig. 7.18 using the expression for the growth rate from Eq. 7.4 and the value of $\chi = 50$, thus only the scale of the T-axis was changed during the fitting procedure. Because we decidedly wanted the fit to err on the side of low misfits (where the input has larger variance), the fit was done after a logarithmic transformation of the data.

The growth rate expression, Eq. 7.4 contains two relevant divergences, one at positive and one at negative misfits $f_{\text{crit}} = \frac{1}{2}\left(\sqrt{\frac{\chi \pm 4}{\chi}} - 1\right)$ which for $\chi = 50$ is around $|f_{\text{crit}}| \approx 0.02$, shown as vertical lines colored green in Fig. 7.18. The calculated model parameter χ clearly overestimates the size of this critical misfit, otherwise Fig. 7.18 shows a good agreement with theory, considering that it is only a one parameter fit.

7.2.7 Interpretation of results

The investigations published in Refs. [116, 117], expounded in Secs. 7.2.3,7.2.4, along with publications made by other authors, namely Refs. [1, 89] share several traits. One of them is that defect formation was studied during a non-equilibrium simulation while epitaxial growth took place. They acknowledge the presence and importance of the ATG interface instability, which is the reason why small perturbations in interface position grow to significant sizes and eventually lead to the incorporation of defects. However, the theoretical results in light of which the simulations were interpreted, contained no mention of the ATG phenomenon. This seems like an omission, and necessitated further deliberation on the subject.

The explanation for the EL results in the previous section illustrated that when the interface free energy anisotropy (i.e. the reduced temperature ϵ) is small and thus the solid-liquid interface is wide, the ATG instability with its growth factor clearly determines the time it takes for defects to form. There is no direct

dependence of the critical thickness on the misfit in this case, since defects form even at an equilibrium, stationary solid-liquid interface. The growth velocity clearly has a large impact on the critical thickness, since that is the determining factor in the number of epilayers the crystal can accumulate in the amount of time, that the instability takes to fully engulf a misfit dislocation. In an isothermal, closed system such an epitaxial front proceeds with $\propto \sqrt{t}$ (Ref. [117]), while in the case of continuous cooling (Ref. [116]), the effect of the growth inhibiting density depletion zone can be somewhat mitigated and growth rate can approach $\propto t$, not unlike in situtations when the crystal-liquid density difference is accounted for in the fashion of a moving boundary condition (Ref. [89]). Thus the quality of front dynamics and the kind of EOM the PFC functional is coupled with makes a difference in the comparability of results of critical thickness.

Another complicating factor is, that for larger values of the interface free energy anisotropy, which means large reduced temperature ϵ and a thin, faceted interface, the front growth mechanism changes drastically. New layers do not form by the uniform adsorption of atoms over the whole solid-liquid interface at once, rather the new layers form by surface nucleation at random sites, followed by the in-plane completion of layers.

EL simulations show, that at large anisotropy ($\epsilon = 0.45$) the equilibrium, stationary interface remains stable against the ATG instability, while at increased undercoolings, during front growth the instability develops. The explanation for this could be, that the growth of each layer needs to proceed via surface nucleation which itself resembles an undulation in the surface position and further nucleation sites will more easily develop at the peaks of the modulation where the driving force for growth and nucleation is larger. This mechanism can overcome the stabilizing force of the larger surface free energy and its anisotropy, a.k.a. surface stiffness.

The plausibility of the ATG scenario of defect formation is further supported, when we consider the dependence of the critical thickness on the noise amplitude, that was applied in the simulations. According to the initially exponential growth model of the ATG interface modulation $A_c(T) = A_0 \exp[\omega T]$, the amplitude of the modulation reaches a large value of $A_c(T)$ at time T, when defects are fully formed. These modulations, however, start from a small value, which is related to the perturbations present in the simulation $A_0 \approx A_{\text{noise}}$, i.e. the noise amplitude. In Fig. 7.10 the critical layer thickness h_c is plotted against $\log_{10}(A_{\text{noise}})$ obtained in continuous cooling simulations. The interface position vs. time relationship is close to linear in this case, $h_c \propto T$. Thus we can establish an approximate relationship

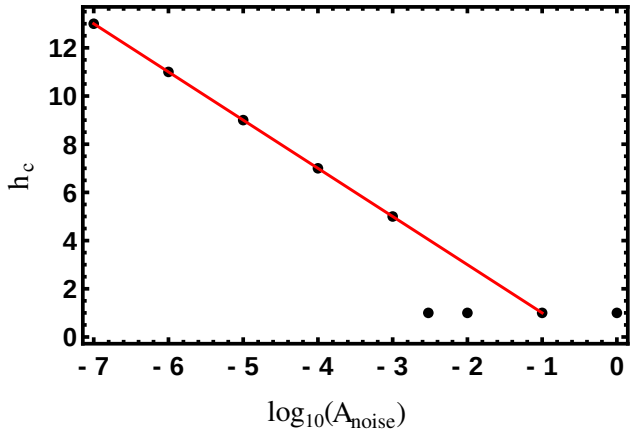

Figure 7.19: Critical thickness vs. noise amplitude, as predicted by the ATG scenario of defect formation. Red line is the fit of the expression $h_c = K_1 - K_2 \log_{10} A_{\text{noise}}$.

between critical thickness h_c and the noise amplitude A_{noise} in these simulations as

$$h_c \propto \log_{10} A_c\,(T) - \log_{10} A_{\text{noise}}\,.$$

We have illustrated the logarithmic dependence of h_c on the noise ampliude in Fig. 7.19, using the dataset from Fig. 7.10, extended with a fit of the above formula. For small values of the noise amplitude, the data follows the prediction, however, there is clearly a mechanism, that breaks down this prediction for large values of the noise, as it leads to defects appearing immediately on the surface of the substrate.

In the adaptation of the ATG growth factor to the EL simulations, we recognized a non-zero critical misfit. Simulation data are compatible with the assertion, that (at least for stationary or slow fronts) there exists a critical strain $|f_c|$, both tensile and compressive, below which the interface instability does not develop. This result is in stark contrast with the theories from Sec. 7.1.1.2, which all place the divergence of the critical thickness at zero misfit. The conclusion we are able to draw from all this, is that those theories of defect formation all relate to situations in which the ATG instability plays no role in the creation of defects, for example when dislocations are already present in the substrate. Otherwise, the kinetic pathway to defect formation must be considered for a complete analysis.

7.3 Contributions

I have performed systematic investigations in two dimensional PFC simulations of the heteroepitaxial critical thickness h_c, on top of a square lattice substrate, in the section perpendicular to the substrate-epilayer interface. I have showed, that h_c increases with decreasing strain. This is in qualitative agreement with experiments and static, energy-balance based approaches, such as the van der Merwe (VDM), the Matthews-Blakeslee (MB) and People-Bean (PB) models. However, I have found large discrepancies when the simulation data from the h_c vs. strain relationship is analyzed in terms of the theoretical results from the VDM, MB and PB models.

For the resolution of this issue, I have investigated the mechanism behind defect formation from the kinetic perspective, based on the Asaro-Tiller-Grinfeld (ATG) instability. I have simulated open systems in equilibrium in PFC simulations and showed, that the formation of misfit dislocations is governed by the growth factor of the ATG instability and not by the number of epitaxial layers, indicating, that the dynamics of defect formation and solidification velocity does play a decisive role in the determination of h_c. I have showed, that basing the estimation of h_c on the ATG growth factor, leads to the divergence of h_c for *non-zero* values of strain, this important fact being the reason, that expressions of the static models when applied to the simulation data miss the origin. Positive and negative values of strain lead to distinct values of h_c, this can be observed experimentally as well as in my simulations. Static theories, however, are symmetric in the sign of strain. Thus, I have recovered the asymmetry, due to the assumption of total stress elimination, since *this* leads to distinct values of the periodicity of the appearance of defects for positive and negative strains.

The ATG growth scenario can also be used to recover the logarithmic noise strength dependence of h_c, which I have observed in my numerical simulations. I have thus concluded, that h_c is more than likely determined by the ATG mechanism, thus defect formation kinetics cannot be neglected.

Appendix A

Theory

A.1 The equilibrium framework of thermodynamics

The study of aggregate matter is the purview of thermodynamics. During the 19th century, this branch of physics experienced a great deal of development, in parallel with the foundation of the modern form of classical mechanics. Newton's formally simple equation of motion provided the basis for the mathematical description of celestial motions. Used in a more mundane and practical context, it also provided the solution for the trajectories of projectiles.

It soon became evident, that knowing the exact equation of motion of classical bodies, led only to complications further down the road. While there exists a general analytical solution for the case of two gravitating bodies, it is not the case even for three bodies. The study of the infamous three-body problem led to the understanding, that even simple mechanical systems behave chaotically, i.e. they show an extreme sensitivity with respect to initial conditions. This has to do with the fact, that the dynamical system that represents matter as a collection of atoms, does not possess attractors, i.e. the microscopic nature of equilibrium is such, that atoms remain in motion, energy is passed between kinetic and potential degrees of freedom indefinitely.

Classical mechanics describes the energy transfer between mechanical degrees of freedom, i.e. the rate of change of the momentum of every particle, equals the gradient of a potential energy function. Irrespective of the complexity of the system under study, total energy is conserved, when the system is isolated from its environment. In general, the change of internal energy of a system equals the work exerted on it, by its environment. When the microscopic details of the system are

not of concern, it seems prudent to study its energy balance.

However, the mechanical energy balance equation for aggregate matter was still not complete. An everyday observation is, that bodies can also exchange energy simply by coming into contact with each other, without any kind of mechanical work taking place. Another effect, that showed the limits of mechanical concepts is related to temperature: gases become warmer, when work is exerted on them in a short amount of time. These phenomena could not be *understood* on the sole basis of mechanical concepts.

Thermodynamics was born out of the study of this other kind of energy transfer, called heat. The complete energy balance equation takes on the form $\mathrm{d}U = đW + đQ$, where an important distinction is made between the exact differential of internal energy and the other inexact differentials. Internal energy is a *property* of the system, something it possesses. On the other hand, work and heat represent *path dependent changes* of internal energy, something that is experienced by the system.

Thermodynamics builds on the concept of state variables, which are well defined in equilibrium. In general, transitions between different states of the system can happen in various ways. An important concept is the quasi-static process, which proceeds arbitrarily slowly and the system goes through equilibrium state points, thus it can be represented as a continuous trajectory in the space of state variables. For general processes, such a trajectory does not exist, this fact is represented by the use of the inexact differentials in the internal energy equation.

The quasi-static mechanical work exerted on the system by its environment can be expressed in terms of state variables as $\mathrm{d}W = -p\mathrm{d}V$. The question arose, whether there is an analogous expression for the case of the heat transfer, in terms of state variables. Through the study of cyclical thermodynamic transformations, it was found, that the ratio of the exchanged heat to the temperature Q/T remained unchanged. This result means, that this quantity behaves like a state function. With this discovery, the formalism of thermodynamics was finally complete.

This new state function was coined entropy. It does not have a direct mechanical analogy. The reversible heat transfer could thus be written as $\mathrm{d}Q = T\mathrm{d}S$. The crucial difference between energy and entropy is, that the former is *conserved* when the system and its environment as a whole is considered, irrespective of processes. Total entropy, on the other hand, is only conserved in *reversible* processes, by definition. In irreversible processes entropy is created, and the ”universe” cannot go back to its previous state. Thus, in a general process, one can only make the statement, that the heat transferred serves as a lower bound for the change in

entropy $\mathrm{d}Q \leq T\mathrm{d}S$.

Thermodynamics is broadly the study of bulk, aggregate matter, the study of transitions between phases of substances and the study of chemical reactions. The framework is general, in the sense, that it has to be augmented with experimental measurements or microscopic calculations to account for the details of specific systems, in the form of response functions. Even the very existence of atoms were debated, when thermodynamic concepts emerged.

Entropy is a quantity that cannot be directly measured, but has to be accounted for. Sometimes a fuzzy concept of the degree of disorder is associated with it. It became clear, that some microscopic details of the system had to be considered for progress to be made, in relation to entropy. The turn came with the realization, that a thermodynamic macrostate is compatible with many microstates of the system, states that differed in the exact microscopic properties of the constituent particles. Boltzmann realized, that the more microstates were available for a given macrostate, the larger its entropy was. From the necessity of extensivity of the entropy, followed its definition in statistical mechanics as $S = \mathrm{k_B} \ln W$. The new study of aggregate systems in a combinatorial way is aptly named statistical physics. Thermodynamics took the role of an asymptotic limiting case for this new field.

A.1.1 The fundamental equation

The particular properties of a system are carried by the functional dependence of the internal energy $U(S, V, N)$ on its natural variables. In the thermodynamic limit the boundary effects are not taken into account, the internal energy and its natural variables are all extensive quantities, i.e. they scale with system size. Partial derivatives give the connection to intensive variables

$$\mathrm{d}U = \left.\frac{\partial U}{\partial S}\right|_{V,N} \mathrm{d}S + \left.\frac{\partial U}{\partial V}\right|_{S,N} \mathrm{d}V + \left.\frac{\partial U}{\partial N}\right|_{S,V} \mathrm{d}N$$

where $\left.\frac{\partial U}{\partial S}\right|_{V,N} = T$ is the temperature, $-\left.\frac{\partial U}{\partial V}\right|_{S,N} = p$ is the pressure and $\left.\frac{\partial U}{\partial N}\right|_{S,V} = \mu$ is the chemical potential. The first term on the RHS describes the change in internal energy due to heat transfer, which really is just energy transfer, without change in volume or the number of particles. The second term describes change in internal energy due to volumetric work, while the third term describes the change in internal energy due to the change in the number of particles. Since the natural variables of energy are all extensive quantities, this function describes a closed and isolated

system, neither energy nor particles can be exchanged with the environment.

A.1.2 Entropy

There is a profound difference between entropy and other extensive thermodynamic quantities. The internal energy U, the volume V and particle number N are connected to conserved mechanical variables. This is not the case for entropy, which has no mechanical analogue. From the celebrated hypothesis of statistical mechanics, it is clear that entropy is related to the way energy is distributed among microscopic degrees of freedom, thus entropy is intrinsically statistical in nature. When certain conditions apply, namely processes progress infinitely slowly (in a quasi-static process) and differences in relevant intensive thermodynamic variables between the equilibrating bodies are infinitesimal, total entropy remains unchanged. However, most processes in nature are not like this, spontaneous processes result in an overall increase in entropy, thus in general $\mathrm{d}S \geq 0$ applies. Of course, the entropy of a body can be decreased, but only at the expense of an equal or larger increase in the entropy of the surrounding environment.

A.1.3 Equilibrium between bodies

Thermodynamic equilibrium is based on the concept of the maximization of entropy, which results in the homogenization of intensive thermodynamic variables. When heat transfer is allowed between bodies, the difference in temperature determines the tendency for the hotter body to lose energy to the colder one. Similarly, when volumetric work is allowed between bodies, the one with the higher pressure will do work on the one with the lower pressure. Particles will be exchanged between bodies, when the chemical potential is different between them. Thus, the thermodynamic equilibrium condition is, that the respective intensive variables be equal, when transfer of the corresponding extensive variable is allowed between them.

When two phases of the same material are in equilibrium with one another, it means that all of their intensive variables p, T, μ are equal and homogeneous, since they must be free to exchange energy in all ways possible, without restriction.

A.1.4 Thermodynamic potentials

Thermodynamic properties of a system in equilibrium are fully determined by the internal energy function U, expressed in terms of its natural variables (S, V, N).

The internal energy is an example of a thermodynamic potential, it describes a closed system with no contact with its environment, since it is expressed in terms of extensive variables. Extensivity is formulated mathematically as $U(\lambda S, \lambda V, \lambda N) = \lambda U(S, V, N)$, which means that the internal energy is a homogeneous function of degree one and as such, differentiation wrt. λ lets us express the internal energy as

$$U = \left.\frac{\partial U}{\partial S}\right|_{V,N} S + \left.\frac{\partial U}{\partial V}\right|_{S,N} V + \left.\frac{\partial U}{\partial N}\right|_{S,V} N\,,$$

where we can identify the partial derivatives from the fundamental equation, thus we get the Euler equation

$$U = TS - pV + \mu N\,.$$

The internal energy is manifestly the sum of three enegy terms. If we imagined, that the system was brought into existence in a constant T temperature environment, then its entropy would correspond exactly to a change in internal energy of TS. The internal energy less this heat obtained from the environment at a constant temperature T, gives rise to a variation of the internal energy, which does not include the heat energy freely supplied from the environment. This energy, $F = U - TS$ is called the Helmholtz free energy and it is the thermodynamic potential of a system, that can exchange heat with its environment. The change in this quantity

$$\mathrm{d}F = \mathrm{d}U - T\mathrm{d}S - S\mathrm{d}T = -S\mathrm{d}T - p\mathrm{d}V + \mu\mathrm{d}N$$

implies, that it is $F = F(T, V, N)$ a natural function of the more familiar temperature, instead of entropy.

A similar argument leads to the identification of the term $-pV$ with the change in internal energy of the system due to change in volume in a constant p pressure environment. Subtracting this from the internal energy gives the enthalpy $H = U + pV$ with natural variables $H = H(S, p, N)$.

A very useful potential is the Gibbs free energy $G = U - TS + pV$, which is the internal energy of a system, with the heat and volumetric work removed, i.e. a system created at constant T, p, with natural variables $G = G(T, p, N)$. An interesting property of the Gibbs free energy is that $G = \mu N$, thus the Gibbs free energy per particle is actually the chemical potential.

Another combination, which will come handy later on, is the grand potential $\Omega = U - TS - \mu N$, which subtracts the energy due to particle exchange with a constant chemical potential environment from the Helmholtz free energy, so its

natural variables are $\Omega = \Omega\,(T, V, \mu)$.

A.1.5 Thermodynamic degrees of freedom

The Euler equation, when differentiated

$$\mathrm{d}U = T\mathrm{d}S + S\mathrm{d}T - p\mathrm{d}V - V\mathrm{d}p + \mu\mathrm{d}N + N\mathrm{d}\mu$$

after substitution of the differential form of the fundamental equation, yields

$$0 = S\mathrm{d}T - V\mathrm{d}p + N\mathrm{d}\mu\,,$$

which is called the Gibbs-Duhem relation. It connects changes in the intensive variables of the system. It is clear, that this equation represents a constraint on the changes in intensive variables, any two variable will fix the state of a one component system, for example $\mu = \mu\,(T, p)$.

A.1.6 Irreversible processes

In general, we need to take into consideration, that the change in entropy $\mathrm{d}S \geq \delta Q/T$ can bn your search, and export your marked results in BibTeX format.e larger, than the transferred heat in the corresponding process, thus for irreversible processes the fundamental equation changes to

$$\mathrm{d}U + p\mathrm{d}V - \mu\mathrm{d}N \leq T\mathrm{d}S\,.$$

Considering a closed system ($\mathrm{d}N = 0$) in an isothermal, isochoric ($\mathrm{d}V = 0$) process, the inequality can be expressed through the Helmholtz free energy as

$$\mathrm{d}\,(U - TS) = \mathrm{d}F \leq 0$$

which states, that during an irreversible process under such conditions, the Helmholtz free energy tends to a minimum. Again, considering a closed system in an isothermal, isobaric ($\mathrm{d}p = 0$) process, the inequality can be expressed through the Gibbs free energy as

$$\mathrm{d}\,(U - TS + pV) = \mathrm{d}G \leq 0\,.$$

It is preferable, to study phase transitions in terms of the intensive control variables of temperature and pressure, thus the minimization of the Gibbs free energy is often considered.

A.1.7 Phase diagrams

At any given point in the space of extensive thermodynamic parameters, the equilibrium state of a system is not necessarily homogeneous. It is perfectly possible, that two adjoining phases of a given material coexist with one another. Equilibrium means, that both phases have reached the same values of the intensive variables T, p, μ, thus total entropy is maximized.

Phase diagrams are a way to visually organize in the space of thermodynamic variables, the global stability of phases. It is advantageous to illustrate this in the space of intensive variables, we take a $p - T$ diagram, for example. As each point represents a state in p, T space, states of phase coexistence appear as lines. These lines separate regions, where different phases attain absolute stability. The chemical potential μ which is the Gibbs free energy per particle, is minimized as a two phase system is subjected to conditions of constant p, T, thus in homogeneous regions of the phase diagram, the phase with the lower chemical potential will be most stable, while at lines representing phase boundaries, the chemical potentials of those adjoining phases are the same.

A.1.8 Equilibrium phase transformations

For the sake of concreteness, let us take the example of a liquid-gas coexistence. When the two phases are in equilibrium, no phase transformation is taking place. There is a difference in internal energy per particle between the two phases. If we wish to increase the liquid fraction (i.e. condense the gas) we need to extract energy from the system (latent heat of transformation), so that particles of the gaseous phase will become liquid particles with less internal energy (more bound state). This transformation process, by controlling the rate of heat transfer, can proceed arbitrarily slowly, thus it is a quasi-static process, during which the intensive variables will remain close to their equilibrium values. If energy is still extracted, after all the gas has turned into liquid, the thermodynamic variables of the system will change according to the liquid's equation of state, thus the system leaves the coexistence line.

A.1.9 Special lines and points

If one considers a system of a single phase, then the phase boundary in the phase diagram *does not* denote special states, there are no singularities or discontinuities in the thermodynamic variables. The phase boundary merely means, that the chemical potential of the other phase will be lower on the other side of the phase boundary.

Phase boundaries in a $p-T$ phase diagram can end in a critical point for phases with only quantitative differences. This signifies, that phase separation is no longer possible. The quantitative differences, between the phases on either side of the coexistence line cease to exist, jump quantities tend to zero, when approaching such a point.

A.2 Brief derivation of the RY theory

A.2.1 The RY order parameter

A classical system of N particles occupying volume V described by the Hamiltonian H_N formally has the grand canonical potential

$$Z_G = \exp\left(-\beta\Omega\right) = \mathrm{Tr}\exp\left[-\beta\left(H_N - \mu N\right)\right]$$

where the trace goes over the particle number, all the momenta and coordinates of the particles, $\beta = 1/k_\mathrm{B}T$ and μ is the chemical potential. The density operator is $\hat{\rho}\left(\boldsymbol{x}\right) = \sum_{i=1}^{N}\delta\left(\boldsymbol{x}-\boldsymbol{x}_i\right)$ with its Fourier transform as $\hat{\rho}_{\boldsymbol{q}} = \sum_{i=1}^{N}\exp\left(\mathrm{i}\boldsymbol{q}\cdot\boldsymbol{x}_i\right)$. The equilibrium average $\rho\left(\boldsymbol{x}\right) = \langle\hat{\rho}\left(\boldsymbol{x}\right)\rangle$ of the density operator has finite lattice periodic Fourier components in the crystalline phase with amplitudes $\langle\hat{\rho}_{\boldsymbol{q}=\boldsymbol{K}_i}\rangle \equiv \langle\hat{\rho}_i\rangle$ at the reciprocal lattice vectors (RLVs) $\boldsymbol{K}_i$, while they vanish in the liquid state. Thus it makes sense to express the grand potential in terms of order parameters $\{\lambda_i\}$ related to the Fourier amplitudes $\langle\hat{\rho}_i\rangle$. For the calculations the RLVs of the crystal structure need to be specified apriori.

The order parameters $\{\lambda_i\}$ are introduced with the help of the normalized Gaussian integrals

$$\int\Pi_i\left(\frac{\mathrm{d}\lambda_i}{\pi}\right)\exp\left(-\left|\lambda_i-\epsilon_i\hat{\rho}_i\right|^2\right) = 1 \tag{A.1}$$

the parameters ϵ_i are real constants determined later, and the integration is over the whole number line in the real and imaginary components of the λ_i. The above

indentity operator is inserted into the expression for the grand potential

$$\exp\left(-\beta\Omega\right) = \mathrm{Tr}\left\{\int \Pi_i \left(\frac{\mathrm{d}\lambda_i}{\pi}\right) \exp\left(-\left|\lambda_i - \epsilon_i\hat{\rho}_i\right|^2\right) \exp\left[-\beta\left(H_N - \mu N\right)\right]\right\}$$

by interchanging the integration over the order parameters $\{\lambda_i\}$ and phase space the previous expression is rewritten as

$$\exp\left(-\beta\Omega\right) = \int \Pi_i \left(\frac{\mathrm{d}\lambda_i}{\pi}\right) \exp\left(-\beta\Omega\left(\{\lambda_j\}\right)\right)$$

with the help of

$$\exp\left(-\beta\Omega\left(\{\lambda_j\}\right)\right) = \mathrm{Tr}\left\{\exp\left(-\sum_i \left|\lambda_i - \epsilon_i\hat{\rho}_i\right|^2 - \beta\left(H_N - \mu N\right)\right)\right\}$$

which is exactly the desired expression for the conditional grand potential, as the exact result holds

$$\epsilon_k \left\langle\hat{\rho}_k\right\rangle = \exp\left(\beta\Omega\right) \int \Pi_i \left(\frac{\mathrm{d}\lambda_i}{\pi}\right) \lambda_k \exp\left(-\beta\Omega\left(\{\lambda_i\}\right)\right) = \left\langle\lambda_k\right\rangle \tag{A.2}$$

that shows the expectation value of the Fourier amplitudes of the density is related to the expectation value of the order parameters.

Next, it is argued that for stable equilibrium systems the conditional free energy $\Omega\left(\{\lambda_j\}\right)$ must possess minima at the order parameter values $\{\lambda_j\} = \left\{\lambda_j^m\right\}$, but in the thermodynamic limit the lowest minimum becomes overwhelmingly more important than other ones, thus a saddle point approximation is employed, the fluctuations in the order parameter $\{\lambda_i\}$ are ignored and equilibrium statistical averages are replaced with values evaluated at the lowest minimum $\left\{\lambda_j^{lm}\right\}$ of $\Omega\left(\left\{\lambda_j^{lm}\right\}\right)$.

When the lowest minimum corresponds to $\left\{\lambda_j^{lm}\right\} \equiv 0$ according to Eq. A.2 the Fourier amplitudes represent the liquid phase, otherwise the system is a crystalline solid. As the undercooling increases the lowest minimum corresponding to the liquid phase will switch to that of the crystal's, the phase transition point is signalled when the two minima have the same value of the thermodynamic potential.

To proceed further, the expression $\left|\lambda - \epsilon\hat{\rho}\right|^2$ is approximated by introducing the average value (fixed by the set of order parmeters $\{\lambda_j\}$) of the operator $\hat{\rho}$ with the indetity $\hat{\rho} = \left\langle\hat{\rho}\right\rangle + \left(\hat{\rho} - \left\langle\hat{\rho}\right\rangle\right)$ and keeping terms up to first order in the deviation

$(\hat{\rho} - \langle\hat{\rho}\rangle)$ the square of the operator $\hat{\rho}^2$ is approximated as follows

$$\hat{\rho}^2 \approx \langle\hat{\rho}\rangle^2 + 2\langle\hat{\rho}\rangle(\hat{\rho} - \langle\hat{\rho}\rangle) = 2\langle\hat{\rho}\rangle\hat{\rho} - \langle\hat{\rho}\rangle^2 .$$

Ramakrishnan-Yussouff assumes $\langle\hat{\rho}\rangle, \lambda \in \mathbb{R}$ holds in a centrosymmetric potential, so that

$$-(\lambda - \epsilon\hat{\rho})(\lambda^* - \epsilon\hat{\rho}^*) = -\lambda\lambda^* + \epsilon\hat{\rho}\lambda^* + \epsilon\hat{\rho}^*\lambda - \epsilon^2\hat{\rho}\hat{\rho}^* \approx -\lambda^2 + \epsilon^2\langle\hat{\rho}\rangle^2 + \left(2\epsilon\lambda - 2\epsilon^2\langle\hat{\rho}\rangle\right)\hat{\rho}$$

With this, the equation for the conditional grand potential becomes

$$\begin{aligned}\exp(-\beta\Omega(\{\lambda_j\})) \approx \quad & \exp\left[\textstyle\sum_i\left(-\lambda_i^2 + \epsilon_i^2\langle\hat{\rho}_i\rangle^2\right)\right]\cdot \\ & \cdot\mathrm{Tr}\left\{\exp\left(-\beta(H_N - \mu N) + \textstyle\sum_i(2\epsilon\lambda_i - 2\epsilon_i^2\langle\hat{\rho}_i\rangle)\hat{\rho}_i\right)\right\}\end{aligned}$$

after taking the logarithm

$$\begin{aligned}\Omega(\{\lambda_j\}) = \quad & k_\mathrm{B}T\textstyle\sum_i\left(\lambda_i^2 - \epsilon_i^2\langle\hat{\rho}_i\rangle^2\right) - \\ & -k_\mathrm{B}T\log\mathrm{Tr}\left\{\exp\left(-\beta(H_N - \mu N) + \textstyle\sum_i(2\epsilon_i\lambda_i - 2\epsilon_i^2\langle\hat{\rho}_i\rangle)\hat{\rho}_i\right)\right\}\end{aligned}$$

thus the grand potential formally is the sum of two terms, the first one disappears at the minimum of the grand potential and the second one is the grand potential of a fluid that has been placed in a periodic external potential

$$v(\boldsymbol{r}) = k_\mathrm{B}T\sum_i 2\left(\epsilon_i^2\langle\hat{\rho}_i\rangle - \epsilon_i\lambda_i\right)\exp(\mathrm{i}\boldsymbol{K}_i\cdot\boldsymbol{r}) . \tag{A.3}$$

Taking the derivative of $\Omega(\{\lambda_j\})$ wrt. the order parameter λ_k the following general result is obtained

$$-\frac{\partial}{\partial\lambda_k}\left(\beta\Omega(\{\lambda_j\}) - \sum_i\lambda_i^2\right) = 2\epsilon_k\langle\hat{\rho}_k\rangle \tag{A.4}$$

thus once the Fourier amplitudes $\{\langle\hat{\rho}_i\rangle\}$ are known for a given $\{\lambda_i\}$, i.e. for a fixed external potential $v(\boldsymbol{x})$ the grand potential can be calculated by integrating the amplitudes wrt. the order parameters.

It is important to note that in classical systems the average density $\langle\hat{\rho}(\boldsymbol{x})\rangle$ can always be written in the following way $\langle\hat{\rho}(\boldsymbol{x})\rangle \propto \exp(-\beta v_\mathrm{eff}(\boldsymbol{x}))$ where the effective potential $v_\mathrm{eff}(\boldsymbol{x}) = v(\boldsymbol{x}) + v_\mathrm{resp}(\boldsymbol{x})$ is the sum of an external potential and the response potential of the system. This response potential will be calculated as a functional of the density change $(\langle\hat{\rho}(\boldsymbol{x})\rangle - \rho_0)$. At equilibrium, at the minimum of the grand potential $\Omega(\{\lambda_j\})$ the expression $\epsilon_k\langle\hat{\rho}_k\rangle = \lambda_k^m$ holds, so the above

external potential Eq. A.3 becomes zero, thus if the response potential is nonzero $v_{\text{resp}}(\boldsymbol{x}) \neq 0$ the system is stable and the density has lattice periodic components, i.e. a crystalline solid is formed. The system does not experience any external potential at the fluid or solid minima, the freezing criterion is obtained without an artificial construct and involves properties of the actual fluid.

A.2.2 Fluid in an external potential

It is the purview of liquid state theory to calculate the change in density of a homogenenous fluid when placed in an external potential, such as a confining wall. Another well established situation is when a test particle is fixed at the origin that imposes an external potential on the rest of the fluid with the same pair potential that acts between all the particles. In this case the resulting density modulation will correspond directly to the two-body density correlation function, or radial distribution function $g(r)$ in the liquid.

Several approximation schemes exist for the calculation of such problems, the two major ones are the Percus-Yevick (PY) and the Hypernetted Chain (HNC) approximations. The PY scheme results when $[\rho(\boldsymbol{r}) \exp(\beta v(\boldsymbol{r})) - \rho_0]$ is expanded as a functional Taylor series in the density change $[\rho(\boldsymbol{r}') - \rho_0]$ and only the first term is kept. The HNC scheme on the other hand expands $\log[\rho(\boldsymbol{r}) \exp(\beta v(\boldsymbol{r}))/\rho_0]$ as a functional Taylor series in $[\rho(\boldsymbol{r}') - \rho_0]$.

According to the argument of Ramakrishnan-Yussouff the external potential $v(\boldsymbol{r})$ which appears in the above problem is smoothly varying, long range and not too large, around $\approx k_{\text{B}}T$ thus the HNC approximation scheme is more appropriate to calculate the inhomogenenous density $\rho(\boldsymbol{r})$.

A.2.3 The pair correlation approximation

As previously stated the HNC approximation expands $\log[\rho(\boldsymbol{r}) \exp(\beta v(\boldsymbol{r}))/\rho_0]$ in terms of the density difference $[\rho(\boldsymbol{r}') - \rho_0]$ (relative to the unperturbed fluid) evaluated at a different point, in terms of a hierarchy of n-point direct correlation functions. In the Ramakrishnan-Yussouff model the expansion stops at the two-particle level, thus in the equation

$$\log[\rho(\boldsymbol{r}) \exp(\beta v(\boldsymbol{r}))/\rho_0] = -\beta[v_{\text{eff}}(\boldsymbol{r}) - v(\boldsymbol{r})] \approx \int \mathrm{d}\boldsymbol{r}' c(\boldsymbol{r} - \boldsymbol{r}')[\rho(\boldsymbol{r}') - \rho_0] \tag{A.5}$$

the two-point direct correlation function

$$c\left(\boldsymbol{r}-\boldsymbol{r}'\right)=\left(\partial\log\left[\rho\left(\boldsymbol{r}\right)\exp\left(\beta v\left(\boldsymbol{r}\right)\right)/\rho_0\right]/\partial\rho\left(\boldsymbol{r}'\right)\right)_{\rho(\boldsymbol{r})=\rho_0}$$

is taken from the homogeneous fluid state with ρ_0 density. This makes the theory manifestly a linear response theory in the density change.

Physically, the Fourier transform of the direct pair correlation function $c\left(q\right)$ originates, through the Orstein-Zernicke (OZ) equation, from the liquid structure factor $S\left(q\right)=\left(1-c\left(q\right)\right)^{-1}$, which is accessible experimentally.

A.2.4 The density ansatz

As the order parameters are related to the Fourier transform of the average density, it is advisable to look for a solution of the inhomogeneous density in terms of an explicit Fourier series also, thus

$$\rho\left(\boldsymbol{r}\right)=\overline{\rho}+V^{-1}\sum_i\left\langle\hat{\rho}_i\right\rangle\exp\left(\mathrm{i}\boldsymbol{K}_i\cdot\boldsymbol{r}\right)=\rho_0\left(1+\eta\right)+\rho_0\sum_i\mu_i\exp\left(\mathrm{i}\boldsymbol{K}_i\cdot\boldsymbol{r}\right)\quad\text{(A.6)}$$

where the fractional density change upon freezing $\eta=\left(\overline{\rho}-\rho_0\right)/\rho_0$ and new amplitudes $\mu_i=\left\langle\hat{\rho}_i\right\rangle/N_0$ (unrelated to the symbol of the chemical potential) are introduced. The Fourier series of the direct correlation function is $c\left(\boldsymbol{r}\right)=N_0^{-1}\sum_{\boldsymbol{q}}c_{\boldsymbol{q}}\exp\left(\mathrm{i}\boldsymbol{q}\cdot\boldsymbol{r}\right)$ and the potential Eq. A.3 are used as well to write Eq. A.5 as

$$\log\left[\rho\left(\boldsymbol{r}\right)/\rho_0\right]=c_0\eta+\sum_i\left[\mu_ic_i-2\epsilon_i^2N_0\mu_i+2\epsilon_i\lambda_i\right]\exp\left(\mathrm{i}\boldsymbol{K}_i\cdot\boldsymbol{r}\right)\,.\quad\text{(A.7)}$$

In this equation the average density $\rho\left(\boldsymbol{r}\right)$ depends explicitly on the order parameters $\{\lambda_i\}$ as well as implicitly through the Fourier amplitudes $\eta,\{\mu_i\}$, thus the coupled equations A.6 and A.7 would need to be solved self-consistently.

Ramakrishnan-Yussouff argues that this problem can be avoided by choosing the so far unspecified constants $\{\epsilon_i\}$ appropriately. In the expression $[\mu_ic_i-2\epsilon_i^2N_0\mu_i+2\epsilon_i\lambda_i]$ the choice $\epsilon_i^2=c_i/\left(2N_0\right)$ eliminates the Fourier amplitudes altogether. The reduced equation looks like

$$\log\left[\rho\left(\boldsymbol{r}\right)/\rho_0\right]=c_0\eta+\sum_i\lambda_i\sqrt{2c_i/N_0}\exp\left(\mathrm{i}\boldsymbol{K}_i\cdot\boldsymbol{r}\right)\,.$$

By inverting the log and plugging in the Fourier series of the density

$$1+\eta+\sum_i \mu_i \exp\left(\mathrm{i}\boldsymbol{K}_i\cdot\boldsymbol{r}\right)=\exp\left[c_0\eta\right]\exp\left[\sum_i \lambda_i\sqrt{2c_i/N_0}\exp\left(\mathrm{i}\boldsymbol{K}_i\cdot\boldsymbol{r}\right)\right]$$

we arrive at closed equations for the amplitudes, which can be solved for, after an inverse transformation

$$\begin{aligned}1+\eta &= \exp\left[c_0\eta\right]V^{-1}\int \mathrm{d}\boldsymbol{r}\exp\left[\sum_i \lambda_i\sqrt{2c_i/N_0}\exp\left(\mathrm{i}\boldsymbol{K}_i\cdot\boldsymbol{r}\right)\right]\\ \mu_k &= \exp\left[c_0\eta\right]V^{-1}\int \mathrm{d}\boldsymbol{r}\exp\left(-\mathrm{i}\boldsymbol{K}_k\cdot\boldsymbol{r}\right)\exp\left[\sum_i \lambda_i\sqrt{2c_i/N_0}\exp\left(\mathrm{i}\boldsymbol{K}_i\cdot\boldsymbol{r}\right)\right]\end{aligned}\tag{A.8}$$

because on the LHS only the amplitudes while on the RHS only the order parameters appear.

A.2.5 Solving for the amplitudes

New variables $\xi_i=\lambda_i\sqrt{2c_i/N_0}$ are introduced and the function

$$\phi\left(\{\xi_i\}\right)=V^{-1}\int \mathrm{d}\boldsymbol{r}\exp\left[\sum_i \xi_i\exp\left(\mathrm{i}\boldsymbol{K}_i\cdot\boldsymbol{r}\right)\right]$$

is defined so the equation for the fractional density change is reduced to $1+\eta=\exp\left[c_0\eta\right]\phi\left(\{\xi_i\}\right)$, but since $\eta\ll 1$ is a small quantity the approximation $1+\eta\approx\exp\eta$ turns it into $\eta=\log\phi\left(\{\xi_i\}\right)/\left(1-c_0\right)$ an explicit equation for the fractional density change. Taking the derivative of $\phi\left(\{\xi_i\}\right)$ wrt. ξ_k generates equations for the amplitudes, which can be used to our benefit

$$\mu_k=\frac{1+\eta}{\phi}\frac{\partial\phi}{\partial\xi_k}=\left(1+\eta\right)\frac{\partial\log\phi}{\partial\xi_k}$$

thus the scalar quantity ϕ plays a central role in the solution. We are in a position to finish the expression Eq. A.4 for the grand potential, plugging in the amplitudes

$$-\frac{\partial}{\partial\lambda_k}\left(\beta\Omega\left(\{\lambda_j\}\right)-\sum_i\lambda_i^2\right)=2\epsilon_k N_0\left(1+\eta\right)\frac{\partial\log\phi}{\partial\xi_k}\,.$$

However, the RHS is not in the form of a total derivative yet. Let us take the derivative of the expression $\frac{(\log\phi)^2}{2(1-c_0)}$

$$\frac{\partial}{\partial\xi_k}\frac{\left(\log\phi\right)^2}{2\left(1-c_0\right)}=\frac{\log\phi}{\left(1-c_0\right)}\frac{\partial}{\partial\xi_k}\log\phi=\eta\frac{\partial}{\partial\xi_k}\log\phi$$

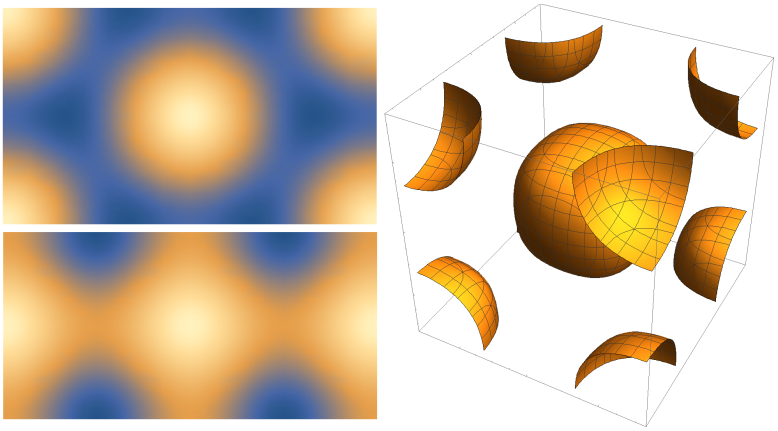

Figure A.1: Bravais-cells of one-mode test functions. Left panel shows in two dimensions the triangular lattice (upper image) and (two cells) of the square lattice. Right panel shows a contour surface of the three-dimensional BCC test function.

which can be used in the equation for the grand potential

$$-\frac{\partial}{\partial\lambda_k}\left(\beta\Omega\left(\{\lambda_j\}\right)-\sum_i\lambda_i^2\right)=2\epsilon_k N_0\frac{\partial}{\partial\xi_k}\left(\log\phi+\frac{(\log\phi)^2}{2\left(1-c_0\right)}\right)$$

and the connection between the derivatives $\partial\xi_i=\sqrt{2c_i/N_0}\partial\lambda_i$ finally give

$$-\frac{\partial}{\partial\lambda_k}\left(\beta\Omega\left(\{\lambda_j\}\right)-\sum_i\lambda_i^2\right)=N_0\frac{\partial}{\partial\lambda_k}\left(\log\phi+\frac{(\log\phi)^2}{2\left(1-c_0\right)}\right)$$

which when integrated results in

$$\beta\Omega\left(\{\lambda_j\}\right)-\beta\Omega\left(\{0\}\right)=\beta\Delta\Omega\left(\{\lambda_j\}\right)=\sum_i\lambda_i^2-N_0\left(\log\phi+\frac{(\log\phi)^2}{2\left(1-c_0\right)}\right)$$

or even simpler

$$\beta\Delta\Omega\left(\{\xi_j\}\right)=N_0\left(\sum_i\frac{\xi_i^2}{2c_i}-\left(1-c_0\right)\left(\eta+\frac{\eta^2}{2}\right)\right). \tag{A.9}$$

This is the Ramakrishnan-Yussouff expression for the grand potential in terms of the rescaled order parameters $\{\xi_i\}$ and the fractional density change $\eta=\eta\left(\{\xi_i\}\right)$, which itself is the function of the order parameters.

A.3 One-mode approximations

Any function of a given crystal symmetry can be constructed as a Fourier sum (see App. A.2.4) over the reciprocal lattice vectors (RLVs) of the crystal ($\boldsymbol{K}_{jl}$, vector j in set l), in general

$$\psi(\boldsymbol{r}) = \overline{\psi} + \sum_l A_l \sum_j \exp\left(\mathrm{i}\boldsymbol{K}_{jl}\cdot\boldsymbol{r}\right), \forall_j : |\boldsymbol{K}_{jl}| = K_l\,.$$

When we say, that the PFC model is a one mode dominant theory, we mean, that at small values of the model parameter ϵ, the periodic pattern $\psi(\boldsymbol{r})$, which minimizes the PFC functional is approximated to a good degree by a Fourier sum over the first RLV set of the crystal structure, i.e. by

$$\psi_{\mathrm{SM}}(\boldsymbol{r}) = \overline{\psi} + A\sum_j \exp\left(\mathrm{i}\boldsymbol{K}_{j1}\cdot\boldsymbol{r}\right)\,.$$

Such a single-mode function is parameterized by the length of the RLVs, which determines the lattice constant, A is the amplitude, equal for the RLVs in the set and finally $\overline{\psi}$ is there to control the average density, as the plane waves have zero mean.

A one-mode or single-mode approximation to the PFC model is achieved by substituting the above test function into the functional and minimizing it analytically. This procedure can be used for example, to analytically calculate an approximate phase diagram. In two dimensions, the most important pattern is the triangular lattice, given by the RLVs

$$\boldsymbol{K} \in \left\{q\begin{pmatrix}1\\0\end{pmatrix}, q\begin{pmatrix}1/2\\\sqrt{3}/2\end{pmatrix}, q\begin{pmatrix}-1/2\\\sqrt{3}/2\end{pmatrix}, q\begin{pmatrix}-1\\0\end{pmatrix}, q\begin{pmatrix}-1/2\\-\sqrt{3}/2\end{pmatrix}, q\begin{pmatrix}1/2\\-\sqrt{3}/2\end{pmatrix}\right\},$$

the sum simplifies to

$$\psi_{\mathrm{TR}}(\boldsymbol{r}) = \overline{\psi} + A\left[\cos(qx/2)\cos\left(qy\sqrt{3}/2\right) + \cos(qx)/2\right]\,.$$

The two-dimensional square lattice is specified by

$$\boldsymbol{K} \in \left\{q\begin{pmatrix}1\\0\end{pmatrix}, q\begin{pmatrix}-1\\0\end{pmatrix}, q\begin{pmatrix}0\\1\end{pmatrix}, q\begin{pmatrix}0\\-1\end{pmatrix}\right\},$$

and the one-mode test function is

$$\psi_{\mathrm{SQ}}(\boldsymbol{r}) = \overline{\psi} + A\left[\cos(qx) + \cos(qy)\right]\,.$$

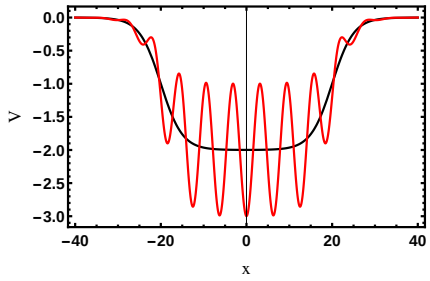

Figure A.2: One-dimensional substrate potential in red, limited in extent to $x \in [-20, 20]$, with an average value of -2 (responsible for adsorption), transition factor 5 and amplitude 1 is achieved with $V(x) = \Theta\left(\frac{x+20}{5}\right)\Theta\left(\frac{-x+20}{5}\right)(-2-\cos x)$. Black line represents the average potential, without the single-mode function.

For small ϵ the preferred three-dimensional crystal structure is BCC, which has the single-mode approximation built from the following RLVs:

$$\boldsymbol{K} \in \left\{ \frac{q}{\sqrt{2}} \begin{pmatrix} 1 \\ 1 \\ 0 \end{pmatrix}, \frac{q}{\sqrt{2}} \begin{pmatrix} 1 \\ 0 \\ 1 \end{pmatrix}, \frac{q}{\sqrt{2}} \begin{pmatrix} 0 \\ 1 \\ 1 \end{pmatrix}, \frac{q}{\sqrt{2}} \begin{pmatrix} 1 \\ -1 \\ 0 \end{pmatrix}, \frac{q}{\sqrt{2}} \begin{pmatrix} 1 \\ 0 \\ -1 \end{pmatrix}, \frac{q}{\sqrt{2}} \begin{pmatrix} 0 \\ 1 \\ -1 \end{pmatrix} \right\},$$

and the one-mode test function is

$$\psi_{\mathrm{BCC}}(\boldsymbol{r}) = \overline{\psi} + A\left[\cos(qx)\cos(qy) + \cos(qx)\cos(qz) + \cos(qy)\cos(qz)\right].$$

The above one-mode test functions are displayed in Fig. A.1.

These functions can also be used for the construction of substrates, applied through an external potential, described in Sec. 7.2.1. To account for the finiteness of the substrate, the spatial extent of the pattern needs to be limited. This is usually achieved by the use of an envelope function in the appropriate spatial variable, such as a properly parameterized tanh function, which is a generalization of a Heaviside step function

$$\Theta(x) = \frac{1}{2}(\tanh(x) + 1).$$

As an example, a one-dimensional, one-mode approximation of a substrate with smooth transition is illustrated in Fig. A.2, note, that the single-mode function $\psi_{\mathrm{SM}} = \cos x$ is used with a negative sign, so that atomic positions correspond to the minima of the external potential.

Appendix B

Numerical considerations

Solutions to the time or pseudo-time dependent equations of motion coupled with PFC thermodynamics of Chap. 4 have been obtained numerically. The development and the deployment of software solutions for the facilitation of the work presented in this dissertation have taken a considerable amount of time and effort. However, since this development does not involve novel solutions, but only the implementation and efficient use of published methods, we deem necessary only to briefly mention a couple of highlights in this regard.

As described in Chap. 4 on time evolution, order parameter theories are based around the idea of the minimization of functions or functionals. The time evolution of the order parameter is mathematically represented by a partial differential equation (PDE). Boundary conditions need to be specified, which are exclusively periodic boundary conditions (PBCs) in this dissertation. An initial value for the order parameter also needs to be given, this determines, which equilibrium state the system relaxes to. Often these PDEs have a stochastic component, a random variable for the representation of thermal fluctuations.

The EL equation and the diffusive EOM follow dissipative dynamics, in time these equations (without fluctuations) monotonically approach local minima. The accurate numerical representation of these minima is practically more important, than the accuracy of the time marching scheme. The study of diffusional or morphological instabilities actually require an accurate numerical scheme. However, the interpretation of the order parameter as a temporally averaged quantity, allows us the modeling of thermal fluctuations at the nanoscale to aid the system in symmetry breaking and barrier passing. The Langevin noise term perturbs the otherwise accurate solutions, so the amplitude of the noise term puts an upper limit on the required accuracy of time stepping. The book [118] is a valuable resource

on the inclusion of Langevin noise in PDEs.

The PFC functional is based on the Fourier transform of the direct correlation function, Eq. 3.2. The simple form of $c(k)$ together with the low-order approximation of the ideal gas term result in a one-mode dominant (see App. A.3) ground state of the solid phase. Thus, the strategy with the PFC driving force, which is the functional derivative $\frac{\delta F}{\delta \psi}$ is to evaluate the parts nonlinear in ψ (approximation to the ideal gas term) in real space, while use the Fourier transform of ψ to construct the part coming from correlations. When the Fourier transform is employed in the numerical solution process of a PDE, it is frequently characterized as a semi-spectral method. The gradient expansion of $c(k)$ in real space $\hat{c}(\mathrm{i}\nabla)$ is not considered for numerical simulations in this dissertation.

The steps necessary to solve the SH form of the ELE (Eq. 4.1) and the EOM (Eq. 4.2) are presented briefly. The Fourier transform is denoted by the operator $\mathcal{F}(.)$ and the symbol $\hat{.}$, we also introduce the operator $L = -1$ for the ELE and $L = \nabla^2$ for the EOM, so that the dynamical equations can be expressed succintly as

$$\partial_t \psi = L\left((1-\epsilon)\,\psi + \psi^3 + \zeta - \mu + \mathcal{F}^{-1}\left(\left[-2k^2 + k^4\right]\hat{\psi}\right)\right) .$$

We take the Fourier transform of the whole equation, also $\hat{L} = \mathcal{F}(L) = \{-1, -k^2\}$

$$\partial_t \hat{\psi} = \hat{L}\left(\left(1 - \epsilon - 2k^2 + k^4\right)\hat{\psi} + \mathcal{F}\left(\psi^3 + \zeta - \mu\right)\right) .$$

The time derivative is approximated with the forward Euler scheme $\partial_t \psi \approx (\psi(t + \Delta t) - \psi(t))/\Delta t$, thus

$$\hat{\psi}(t + \Delta t) = \hat{\psi}(t) + \Delta t \hat{L}\left(1 - \epsilon - 2k^2 + k^4\right)\hat{\psi} + \Delta t \hat{L}\mathcal{F}\left(\psi^3 + \zeta - \mu\right) .$$

The useful quality of the semi-spectral method is, that one is able to handle implicitly the parts that are linear in the unknown function $\hat{L}(1 - \epsilon - 2k^2 + k^4)\hat{\psi}$, thus the time marching becomes semi-implicit, as that part is evaluated at time $t + \Delta t$

$$\left[1 - \Delta t \hat{L}\left(1 - \epsilon - 2k^2 + k^4\right)\right]\hat{\psi}(t + \Delta t) = \hat{\psi}(t) + \Delta t \hat{L}\mathcal{F}\left(\psi^3 + \zeta - \mu\right) ,$$

where the spatial operator is inverted point-wise in Fourier space to arrive at the final form of time marching

$$\hat{\psi}(t + \Delta t) = \frac{\hat{\psi}(t) + \Delta t \hat{L}\mathcal{F}(\psi^3 + \zeta - \mu)}{1 - \Delta t \hat{L}(1 - \epsilon - 2k^2 + k^4)} .$$

The semi-implicit time stepping improves the stability of the numerical solution considerably. More information on the semi-spectral semi-implicit time marching scheme in PFC context is available in Ref. [119].

The numerical solution of the generalized EOMs in Sec. 4.4 require different considerations, than the equations of the purely dissipative cases. Besides the representation of the order parameter, the accuracy of its time derivative also becomes important. The thermodynamic driving force takes the place of the reactive force, which drives wave propagation, the rate of dissipation is controlled by a viscosity parameter. The spatial operators and the correlational part of the free energy are still evaluated in Fourier space, however, due to the coupled nature of the equations, an explicit second order accurate scheme, Heun's method is used for the time marching of the hydrodynamic equations.

The final forms of the numerical equations were solved on Graphical Processing Units (GPUs), which currently provide the highest compute density and memory bandwidth for the lowest power consumption and cost. Fourier transforms were accomplished with the CUDA implementation of the Fast Fourier Transform [120] algorithm.

Appendix C

Analysis

C.1 Bond order parameters

The configuration of atoms in particle based simulations is frequently analyzed with the help of bond-orientational order parameters, bond order parameters for short. These were introduced in Ref. [85] and sometimes go by the name of Steinhardt order parameters. First, atomic neighborhoods are defined $|\boldsymbol{r}_{ij}| < r_c$ based on a pairwise cutoff distance determined as the location r_c of the first minimum of the radial distribution function. Then, bond vectors $\boldsymbol{r}_{ij}$ are calculated, pointing from particle i to its neighbor particles j. Spherical harmonics basis functions $Y_{lm}\left(\boldsymbol{r}_{ij}\right)$ of order l are evaluated for every bond and averaged over the neighbors for each atom. A complex valued bond orientational vector is constructed

$$\left(\boldsymbol{q}_l^i\right)_m = \frac{1}{N_i} \sum_{j=1}^{N_i} Y_{lm}\left(\boldsymbol{r}_{ij}\right) .$$

The local Steinhardt order parameters q_l^i are coordinate system independent combinations of the spherical harmonics, aside from a normalization constant, they are the lengths of the $\boldsymbol{q}_l$, $.^*$ denotes complex conjugation,

$$q_l^i = \sqrt{\frac{4\pi}{2l+1} \boldsymbol{q}_l^i \cdot \boldsymbol{q}_l^{*i}} .$$

Lechner and Dellago in Ref. [78] found increased accuracy in structure determination, when an averaged order parameter is used in the calculations. The bond orientational vectors $\boldsymbol{q}_l^i$ are averaged over the first neigbors (and the particle itself)

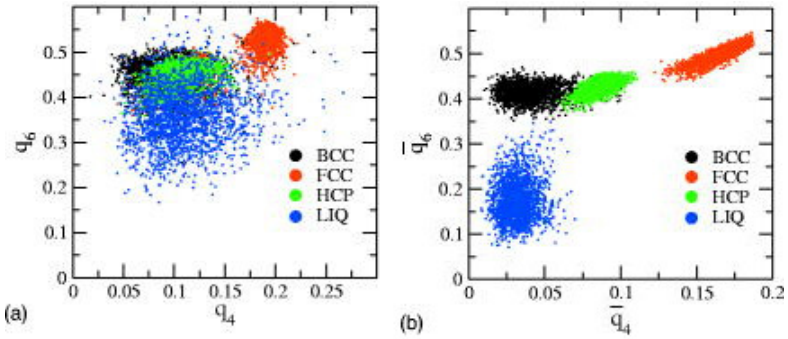

Figure C.1: Second neighbor information improves the quality of structure identification, illustrated on $q_6 - q_4$ scatterplots. Left panel shows the local Steinhardt bond orientational order parameters $q_6 - q_4$ for a molecular dynamics simulation of a Lennard-Jones liquid. Right panel shows the averaged order parameters $\overline{q}_6 - \overline{q}_4$, proposed by Lechner and Dellago. Source: Ref. [78].

to obtain

$$\overline{\boldsymbol{q}}_l^i = \frac{1}{N_i} \sum_{k=0}^{N_i} \boldsymbol{q}_l^k \,,$$

while the improved order parameter is calculated similarly

$$\overline{q}_l^i = \sqrt{\frac{4\pi}{2l+1} \overline{\boldsymbol{q}}_l^i \cdot \overline{\boldsymbol{q}}_l^{*i}} \,.$$

Fluctuations in the atomic positions smear out the local Steinhard order parameters, but the averaged versions provide a more robust separation, this is illustrated in Fig. C.1.

Additionally, the correlation of bond order can be calculated for each atom. The scalar product of the $\boldsymbol{q}_l$ vector of atom i and of its neigboring atom j when surpasses a value $\boldsymbol{q}_l^i \cdot \boldsymbol{q}_l^{*j} > 0.5$ signals a solid-like bond between these atoms. The parameter ξ is used, to represent the number of such solid-like bonds for each atom

$$\xi_i = \sum_{j=1}^{N_i} \Theta \left(\boldsymbol{q}_l^i \cdot \boldsymbol{q}_l^{j*} - 0.5 \right) \,.$$

C.2 Voronoi analysis

Voronoi analysis is a standard method for the segmentation of space into non-overlapping regions, also without gaps, given a set of points as input. It is the generalization of the Wigner-Seitz cell, without the requirement of periodicity. The Voronoi cell (see Fig. C.2) of a given point includes space, which is closer to that

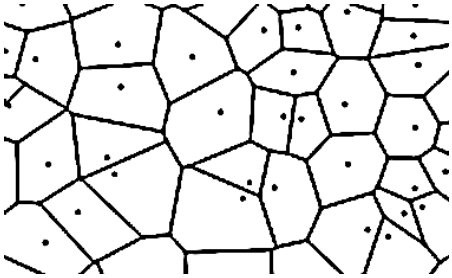

Figure C.2: Illustrating the concept of Voronoi cells, regions of space closer to a chosen point, than to any other. This construction segments space without gaps or overlaps.

point, than to any other. It is useful for both two and three-dimensional point sets. Standard software libraries exist for the calculation, for example Voro++ [121].

C.3 Hexatic order parameter

A common tool to analyze two dimensional, closed packed, local structure is the so-called hexatic order parameter [122], which is constructed from a set of points in the plane. As the name implies, this order parameter will reach a large value, when atoms are situated at the vertices of a hexagon around a central atom (we call this a triangular lattice). The definition

$$\hat{g}_6^i = \sum_j \exp\left(6\mathrm{i}\Theta_{ij}\right) = g_6^i \exp\left(\mathrm{i}\Theta_i\right)$$

does not include the bond lengths between atoms, only the bond angles Θ_{ij} between the central atom i and its neighbors j. The factor 6 is responsible for the constructive interference of six-fold symmetry. The hexatic order parameter is really the modulus of the above complex number $g_6 = |\hat{g}_6|$. The orientation of the hexatic arrangement of atoms relative to the laboratory frame is given by the argument of the complex order parameter $\Theta_i = \arg\left(\hat{g}_6\right)$.

C.4 Coarse-grained amplitude

One can be interested in the segmentation of the solid from the liquid phase or in the determination of the position of defects in the crystal lattice. A coordinate system independent order parameter would be useful, which characterizes the strength of local periodic ordering.

Let us introduce the coarse-graining operation $\langle . \rangle_{\mathrm{CG}}$, which filters out Fourier components of its argument above a set value, let this be $k_{\max}/2$, so the coarse-graining operation over any function $a(\boldsymbol{r})$ can be written succintly as

$$\langle a \rangle_{\mathrm{CG}} = \mathcal{F}^{-1} \left\{ \Theta \left(k_{\max}/2 - |\boldsymbol{k}| \right) \mathcal{F} [a] \right\} .$$

The structural information of the pattern in the PFC model is carried in the density distribution ψ at high wavenumbers, around $k_{\max}$, where the direct correlation function reaches its maximum. The high wavenumber components of ψ can be obtained by subtracting the coarse-grained density $\psi - \langle \psi \rangle_{\mathrm{CG}}$. The desired order parameter would take on a large value, where a *periodic* pattern with large amplitude is present, but would not display its atomic periodicity. This can be achieved, if we take the square of the high wavenumber component, calculated above and coarse-grain it. The new order parameter is calculated as

$$\langle \psi \rangle_{\mathrm{amp}} = \sqrt{\left\langle \left(\psi - \langle \psi \rangle_{\mathrm{CG}} \right)^2 \right\rangle_{\mathrm{CG}}} ,$$

this coarse-grained amplitude is not sensitive to the variation of the average density and shows the long-wavelength variation in the *amplitude* field.

Bibliography

[1] K. R. Elder, M. Katakowski, M. Haataja, and M. Grant, Physical Review Letters **88**, 2457011 (2002).

[2] H. Emmerich, H. Löwen, R. Wittkowski, T. Gruhn, G. I. Tóth, G. Tegze, and L. Gránásy, Advances in Physics **61**, 665 (2012).

[3] S. P. Das, *Statistical Physics of Liquids at Freezing and Beyond* (Cambridge University Press, 2011).

[4] B. J. Alder and T. E. Wainwright, The Journal of Chemical Physics **27**, 1208 (1957).

[5] S. G. Brush, H. L. Sahlin, and E. Teller, The Journal of Chemical Physics **45**, 2102 (1966).

[6] J.-P. Hansen and L. Verlet, Physical Review **184**, 151 (1969).

[7] F. A. Lindemann, Physikalische Zeitschrift **11**, 609 (1910).

[8] D. Stroud and N. W. Ashcroft, Physical Review B **5**, 371 (1972).

[9] J. E. Lennard-Jones and A. F. Devonshire, Proceedings of the Royal Society of London A **170**, 464 (1939).

[10] J. M. Kosterlitz and D. J. Thouless, Journal of Physics C: Solid State Physics **6**, 1181 (1973).

[11] J. G. Kirkwood and E. Monroe, The Journal of Chemical Physics **9**, 514 (1941).

[12] M. Yussouff, T. V. Ramakrishnan, and M. Yussouff, Physical Review B **19**, 2775 (1979).

[13] Y. Rosenfeld, The Journal of Chemical Physics **89**, 4272 (1988).

[14] W. A. Curtin and N. W. Ashcroft, Physical Review Letters **56**, 2775 (1986).

[15] G. I. Tóth, L. Gránásy, and G. Tegze, Journal of Physics: Condensed Matter **26**, 055001 (2014).

[16] R. Backofen and A. Voigt, Journal of Physics: Condensed Matter **22**, 364104 (2010).

[17] G. I. Tóth, T. Pusztai, G. Tegze, G. Tóth, and L. Gránásy, Physical Review Letters **107**, 175702 (2011).

[18] G. I. Tóth, G. Tegze, T. Pusztai, and L. Gránásy, Physical Review Letters **108**, 025502 (2012).

[19] L. Gránásy, F. Podmaniczky, G. I. Tóth, G. Tegze, and T. Pusztai, Chemical Society Reviews **43**, 2159 (2014).

[20] K. R. Elder, N. Provatas, J. Berry, P. Stefanovic, and M. Grant, Physical Review B **75**, 64107 (2007).

[21] K.-A. Wu, A. Adland, and A. Karma, Physical Review E **81**, 061601 (2010).

[22] G. Tegze, L. Gránásy, G. I. Tóth, J. F. Douglas, and T. Pusztai, Soft Matter **7**, 1789 (2011).

[23] G. I. Tóth, G. Tegze, T. Pusztai, G. Tóth, and L. Gránásy, Journal of Physics: Condensed Matter **22**, 364101 (2010).

[24] J. Berry, K. R. Elder, and M. Grant, Physical Review E **77**, 061506 (2008).

[25] J. Berry and M. Grant, Physical Review Letters **106**, 175702 (2011).

[26] J. Swift and P. C. Hohenberg, Physical Review A **15**, 319 (1977).

[27] F. Podmaniczky, G. I. Tóth, T. Pusztai, and L. Gránásy, Journal of Crystal Growth **385**, 148 (2014).

[28] P. C. Hohenberg and B. I. Halperin, Reviews of Modern Physics **49**, 435 (1977).

[29] S. van Teeffelen, R. Backofen, A. Voigt, and H. Löwen, Physical Review E **79**, 051404 (2009).

[30] U. M. B. Marconi and P. Tarazona, The Journal of Chemical Physics **110**, 8032 (1999).

[31] H. Löwen, Journal of Physics: Condensed Matter **15**, V1 (2003).

[32] A. J. Archer and M. Rauscher, Journal of Physics A: Mathematical and General **37**, 9325 (2004).

[33] A. J. Archer and R. Evans, The Journal of Chemical Physics **121**, 4246 (2004).

[34] S. van Teeffelen, C. N. Likos, and H. Löwen, Physical Review Letters **100**, 108302 (2008).

[35] A. J. Archer, Journal of Physics: Condensed Matter **18**, 5617 (2006).

[36] A. J. Archer, The Journal of Chemical Physics **130**, 14509 (2009).

[37] S. Majaniemi and M. Grant, Physical Review B **75**, 054301 (2007).

[38] S. Majaniemi, M. Nonomura, and M. Grant, The European Physical Journal B **66**, 329 (2008).

[39] P. Stefanovic, M. Haataja, and N. Provatas, Physical Review Letters **96**, 225504 (2006).

[40] S. Praetorius and A. Voigt, Macromolecular Theory and Simulations **20**, 541 (2011).

[41] L. D. Landau and E. M. Lifshitz, *Fluid Mechanics* (Pergamon, New York, 1959).

[42] B. Z. Shang, N. K. Voulgarakis, and J.-W. Chu, The Journal of Chemical Physics **135**, 044111 (2011).

[43] R. Salmon, Annual Review of Fluid Mechanics **20**, 225 (1988).

[44] C. Liu and Z. Li, AIP Advances **1**, 32108 (2011).

[45] M. D. Ediger, P. Harrowell, and L. Yu, The Journal of Chemical Physics **128**, 034709 (2008).

[46] F. Podmaniczky and L. Gránásy, Journal of Crystal Growth **597**, 126854 (2022).

[47] M. Volmer and A. Weber, Zeitschrift für Physikalische Chemie **119U**, 277 (1926).

[48] L. Farkas, Zeitschrift für Physikalische Chemie **125**, 236 (1927).

[49] R. Becker and W. Döring, Annalen der Physik **416**, 719 (1935).

[50] D. Turnbull and J. C. Fisher, The Journal of Chemical Physics **17**, 71 (1949).

[51] K. F. Kelton and A. L. Greer, *Nucleation in Condensed Matter: Applications in Materials and Biology*, Pergamon Materials Series (Pergamon, 2010).

[52] D. Kashchiev, *Nucleation: Basic Theory with Applications* (Butterworth Heinemann, 2000).

[53] I. S. Gutzow and J. W. P. Schmelzer, *The Vitreous State: Thermodynamics, Structure, Rheology, and Crystallization* (Springer Berlin Heidelberg, 2013).

[54] K. F. Kelton, Solid State Physics **45**, 75 (1991).

[55] D. W. Oxtoby, Journal of Physics: Condensed Matter **4**, 7627 (1992).

[56] H. Tanaka, Journal of Physics: Condensed Matter **23**, 284115 (2011).

[57] W. C. Swope and H. C. Andersen, Physical Review B **41**, 7042 (1990).

[58] P. R. ten Wolde, M. J. Ruiz-Montero, and D. Frenkel, Physical Review Letters **75**, 2714 (1995).

[59] S. Auer and D. Frenkel, Nature **409**, 1020 (2001).

[60] L. Filion, M. Hermes, R. Ni, and M. Dijkstra, The Journal of Chemical Physics **133**, 244115 (2010).

[61] S. Jungblut and C. Dellago, The Journal of Chemical Physics **134**, 104501 (2011).

[62] Y. Shibuta, S. Sakane, T. Takaki, and M. Ohno, Acta Materialia **105**, 328 (2016).

[63] D. Moroni, P. R. ten Wolde, and P. G. Bolhuis, Physical Review Letters **94**, 235703 (2005).

[64] M. Isobe and W. Krauth, The Journal of Chemical Physics **143**, 084509 (2015).

[65] T. Schilling, H. J. Schöpe, M. Oettel, G. Opletal, and I. Snook, Physical Review Letters **105**, 025701 (2010).

[66] J. S. Rowlinson, Journal of Statistical Physics **20**, 197 (1979).

[67] J. W. Cahn and J. E. Hilliard, The Journal of Chemical Physics **28**, 258 (1958).

[68] K. Binder, Physical Review B **8**, 3423 (1973).

[69] T. Pusztai, G. Tegze, G. I. Tóth, L. Környei, G. Bansel, Z. Fan, and L. Gránásy, Journal of Physics: Condensed Matter **20**, 404205 (2008).

[70] L. Gránásy, T. Börzsönyi, and T. Pusztai, Physical Review Letters **88**, 206105 (2002).

[71] L. Gránásy, T. Pusztai, D. Saylor, and J. A. Warren, Physical Review Letters **98**, 035703 (2007).

[72] J. A. Warren, T. Pusztai, L. Környei, and L. Gránásy, Physical Review B **79**, 014204 (2009).

[73] D. W. Oxtoby, Annual Review of Materials Research **32**, 39 (2002).

[74] Y. C. Shen and D. W. Oxtoby, Physical Review Letters **77**, 3585 (1996).

[75] P. Grosfils and J. F. Lutsko, Langmuir **26**, 8510 (2010).

[76] J. F. Lutsko, The Journal of Chemical Physics **135**, 161101 (2011).

[77] J. F. Lutsko and M. A. Durán-Olivencia, The Journal of Chemical Physics **138**, 244908 (2013).

[78] W. Lechner and C. Dellago, Journal of Chemical Physics **129**, 114707 (2008).

[79] A. Stukowski, Modelling and Simulation in Materials Science and Engineering **18**, 15012 (2010).

[80] J. F. Lutsko and G. Nicolis, Physical Review Letters **96**, 046102 (2006).

[81] H. J. Schöpe, G. Bryant, and W. van Megen, Physical Review Letters **96**, 175701 (2006).

[82] T. H. Zhang and X. Y. Liu, Journal of the American Chemical Society **129**, 13520 (2007).

[83] T. H. Zhang and X. Y. Liu, Journal of Physical Chemistry B **111**, 14001 (2007).

[84] P. Tan, N. Xu, and L. Xu, Nature Physics **10**, 73 (2014).

[85] P. J. Steinhardt, D. R. Nelson, and M. Ronchetti, Physical Review B **28**, 784 (1983).

[86] T. Kawasaki and H. Tanaka, Proceedings of the National Academy of Sciences **107**, 14036 (2010).

[87] Y. Shibuta and T. Suzuki, Journal of Chemical Physics **129**, 144102 (2008).

[88] V. V. Hoang, Nanotechnology **20**, 295703 (2009).

[89] K. R. Elder and M. Grant, Physical Review E **70**, 18 (2004).

[90] G. Tegze, L. Gránásy, G. I. Tóth, F. Podmaniczky, A. Jaatinen, T. Ala-Nissila, and T. Pusztai, Physical Review Letters **103**, 035702 (2009).

[91] A. Baskaran, A. Baskaran, and J. Lowengrub, The Journal of Chemical Physics **141**, 174506 (2014).

[92] V. Heinonen, C. V. Achim, J. M. Kosterlitz, S.-C. Ying, J. Lowengrub, and T. Ala-Nissila, Physical Review Letters **116**, 024303 (2016).

[93] A. Baskaran, Z. Guan, and J. Lowengrub, Computer Methods in Applied Mechanics and Engineering **299**, 22 (2016).

[94] W. Kurz and D. Fisher, *Fundamentals of Solidification* (Trans Tech Publications, Aedermannsdorf, Switzerland, 1992).

[95] A. L. Greer, A. M. Bunn, A. Tronche, P. V. Evans, and D. J. Bristow, Acta Materialia **48**, 2823 (2000).

[96] T. E. Quested and A. L. Greer, Acta Materialia **53**, 2683 (2005).

[97] V. Ferreiro, J. F. Douglas, J. A. Warren, and A. Karim, Physical Review E **65**, 042802 (2002).

[98] V. Ferreiro, J. F. Douglas, J. A. Warren, and A. Karim, Physical Review E **65**, 051606 (2002).

[99] J. H. Magill, Journal of Materials Science **36**, 3143 (2001).

[100] L. Gránásy, T. Pusztai, J. A. Warren, J. F. Douglas, T. Börzsönyi, and V. Ferreiro, Nature Materials **2**, 92 (2003).

[101] L. Gránásy, T. Pusztai, T. Börzsönyi, J. A. Warren, and J. F. Douglas, Nature Materials **3**, 645 (2004).

[102] L. Gránásy, T. Pusztai, G. Tegze, J. A. Warren, and J. F. Douglas, Physical Review E **72**, 011605 (2005).

[103] L. Gránásy, L. Rátkai, A. Szállás, B. Korbuly, G. I. Tóth, L. Környei, and T. Pusztai, Metallurgical and Materials Transactions A **45**, 1694 (2014).

[104] N. Hendler, E. Mentovich, B. Korbuly, T. Pusztai, L. Gránásy, and S. Richter, Nano Research **8**, 3630 (2015).

[105] R. J. Asaro and W. A. Tiller, Metallurgical Transactions **3**, 1789 (1972).

[106] M. A. Grinfeld, Fluid Dynamics **22**, 169 (1987).

[107] E. Allahyarov, K. Sandomirski, S. U. Egelhaaf, and H. Löwen, Nature Communications **6**, 7110 (2015).

[108] F. C. Frank and J. H. van der Merwe, Proceedings of the Royal Society of London A **198**, 205 (1949).

[109] P. Müller and A. Saúl, Surface Science Reports **54**, 157 (2004).

[110] K. Kassner and C. Misbah, Europhysics Letters **46**, 217 (1999).

[111] J. H. van der Merwe, Journal of Applied Physics **34**, 123 (1963).

[112] J. W. Matthews and A. E. Blakeslee, Journal of Crystal Growth **27**, 118 (1974).

[113] R. People and J. C. Bean, Applied Physics Letters **47**, 322 (1985).

[114] F. R. N. Nabarro, *Theory of Crystal Dislocations*, International series of monographs on physics (Clarendon Press, Oxford, 1967).

[115] R. People and J. C. Bean, Applied Physics Letters **49**, 229 (1986).

[116] F. Podmaniczky, G. I. Tóth, G. Tegze, and L. Gránásy, Metallurgical and Materials Transactions A **46**, 4908 (2015).

[117] F. Podmaniczky, G. I. Tóth, G. Tegze, T. Pusztai, and L. Gránásy, Journal of Crystal Growth **457**, 24 (2017).

[118] J. García-Ojalvo and J. M. Sancho, *Noise in Spatially Extended Systems*, Institute for Nonlinear Science (Springer New York, 1999).

[119] G. Tegze, G. Bansel, G. I. Tóth, T. Pusztai, Z. Fan, and L. Gránásy, Journal of Computational Physics **228**, 1612 (2009).

[120] J. W. Cooley and J. W. Tukey, Mathematics of Computation **19**, 297 (1965).

[121] C. H. Rycroft, Chaos **19**, 041111 (2009).

[122] B. I. Halperin and D. R. Nelson, Physical Review Letters **41**, 121 (1978).